NAVAL POSTGRADUATE SCHOOL
Monterey, California

THESIS

SUPERSONIC FLOW FIELD VISUALIZATION STUDIES OF THE M$_\infty$ = 6 PRICE WAVERIDER PLANFORM

by

Karl Garcia

September 2001

Thesis Advisor:	Conrad F. Newberry
Second Reader:	Garth V. Hobson

Approved for public release; distribution is unlimited.

Report Documentation Page

Report Date	Report Type	Dates Covered (from... to)
30 Sep 2001	N/A	-

Title and Subtitle	Contract Number
Supersonic Flow Field Visualization Studies of the M.... = 6 Price Waverider Planform	Grant Number
	Program Element Number

Author(s)	Project Number
6. AUTHOR(S) Garcia, Karl	Task Number
	Work Unit Number

Performing Organization Name(s) and Address(es)	Performing Organization Report Number
Research Office Naval Postgraduate School Monterey, Ca 93943-5138	

Sponsoring/Monitoring Agency Name(s) and Address(es)	Sponsor/Monitor's Acronym(s)
	Sponsor/Monitor's Report Number(s)

Distribution/Availability Statement
Approved for public release, distribution unlimited

Supplementary Notes

Abstract

Subject Terms

Report Classification	Classification of this page
unclassified	unclassified

Classification of Abstract	Limitation of Abstract
unclassified	UU

Number of Pages
109

REPORT DOCUMENTATION PAGE	*Form Approved OMB No. 0704-0188*

Public reporting burden for this collection of information is estimated to average 1 hour per response, including the time for reviewing instruction, searching existing data sources, gathering and maintaining the data needed, and completing and reviewing the collection of information. Send comments regarding this burden estimate or any other aspect of this collection of information, including suggestions for reducing this burden, to Washington headquarters Services, Directorate for Information Operations and Reports, 1215 Jefferson Davis Highway, Suite 1204, Arlington, VA 22202-4302, and to the Office of Management and Budget, Paperwork Reduction Project (0704-0188) Washington DC 20503.

1. AGENCY USE ONLY *(Leave blank)*	2. REPORT DATE September 2001	3. REPORT TYPE AND DATES COVERED Master's Thesis	

4. TITLE AND SUBTITLE: Supersonic Flow Field Visualization Studies of the $M_\infty = 6$ Price Waverider Planform	5. FUNDING NUMBERS

6. AUTHOR(S) Garcia, Karl

7. PERFORMING ORGANIZATION NAME(S) AND ADDRESS(ES) Naval Postgraduate School Monterey, CA 93943-5000	8. PERFORMING ORGANIZATION REPORT NUMBER

9. SPONSORING / MONITORING AGENCY NAME(S) AND ADDRESS(ES) N/A	10. SPONSORING / MONITORING AGENCY REPORT NUMBER

11. SUPPLEMENTARY NOTES The views expressed in this thesis are those of the author and do not reflect the official policy or position of the Department of Defense or the U.S. Government.

12a. DISTRIBUTION / AVAILABILITY STATEMENT Approved for public release; distribution is unlimited.	12b. DISTRIBUTION CODE

13. ABSTRACT *(maximum 200 words)*

Supersonic tests of the conical flow derived $M_\infty = 6$ (design) Price waverider planform were conducted using the Naval Postgraduate School wind tunnel. These tests are part of a continuing effort to study the characteristics of waverider configured vehicles. Two sting-mounted, flat-plate stainless-steel Price waverider planform models were utilized for testing in the NPS 4-inch by 4-inch cross section supersonic blowdown wind tunnel. Tests at Mach numbers of $M_\infty = 1.7$, 2.8 and 4 were attempted but flowfield studies were only completed at $M_\infty = 4$. Sting mount flow blockage (choked flow) prevented test section starting at freestream test Mach numbers of $M_\infty = 1.7$ and 2.8. Horizontal (side-view) and vertical (top-view) mounted shadowgraph pictures and pressure sensitive paint images were taken at pitch angles of $\alpha = 0°$, 2° and 4°. The Mach 4 shadowgraph and pressure sensitive paint results correlate well with previous CFD results using the three-dimensional Price waverider model. The choked flow tests at $M_\infty = 1.7$ and 2.8 are discussed in detail; suggestions are given for future work in this Mach number test spectrum.

14. SUBJECT TERMS Waverider, Supersonic Wind Tunnel Testing, Pressure Sensitive Paint, Shadowgraph, Shock Boundary Layer Interaction, Normal Shock, Oblique Shock.	15. NUMBER OF PAGES 91
	16. PRICE CODE

17. SECURITY CLASSIFICATION OF REPORT Unclassified	18. SECURITY CLASSIFICATION OF THIS PAGE Unclassified	19. SECURITY CLASSIFICATION OF ABSTRACT Unclassified	20. LIMITATION OF ABSTRACT UL

THIS PAGE INTENTIONALLY LEFT BLANK

SUPERSONIC FLOW FIELD VISUALIZATION STUDIES OF THE $M_\infty = 6$
PRICE WAVERIDER PLANFORM

Karl Garcia
Lieutenant, United States Navy
B.S., United States Naval Academy, 1993

Submitted in partial fulfillment of the
requirements for the degree of
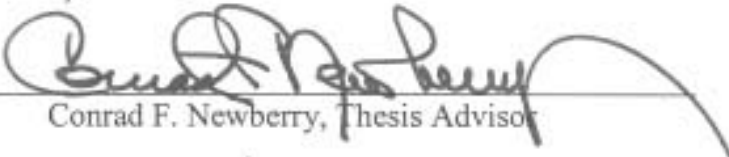
MASTER OF SCIENCE IN AERONAUTICAL ENGINEERING
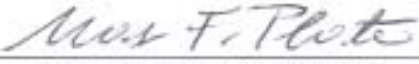
from the

NAVAL POSTGRADUATE SCHOOL
September 2001

Author: _____
Karl Garcia

Approved by: _____
Conrad F. Newberry, Thesis Advisor

_____
Garth V. Hobson, Second Reader

_____
Max F. Platzer, Chairman
Department of Aeronautics and Astronautics

THIS PAGE INTENTIONALLY LEFT BLANK

ABSTRACT

Supersonic tests of the conical flow derived $M_\infty = 6$ (design) Price waverider planform were conducted using the Naval Postgraduate School wind tunnel. These tests are part of a continuing effort to study the characteristics of waverider configured vehicles. Two sting-mounted, flat-plate stainless-steel Price waverider planform models were utilized for testing in the NPS 4-inch by 4-inch cross section supersonic blowdown wind tunnel. Tests at Mach numbers of $M_\infty = 1.7, 2.8$ and 4 were attempted but flowfield studies were only completed at $M_\infty = 4$. Sting mount flow blockage (choked flow) prevented test section starting at freestream test Mach numbers of $M_\infty = 1.7$ and 2.8. Horizontal (side-view) and vertical (top-view) mounted shadowgraph pictures and pressure sensitive paint images were taken at pitch angles of $\alpha = 0°, 2°$ and 4°. The Mach 4 shadowgraph and pressure sensitive paint results correlate well with previous CFD results using the three-dimensional Price waverider model. The choked flow tests at $M_\infty = 1.7$ and 2.8 are discussed in detail; suggestions are given for future work in this Mach number test spectrum.

THIS PAGE INTENTIONALLY LEFT BLANK

TABLE OF CONTENTS

LIST OF FIGURES

x

THIS PAGE INTENTIONALLY LEFT BLANK

LIST OF TABLES

THIS PAGE INTENTIONALLY LEFT BLANK

ACKNOWLEDGMENTS

THIS PAGE INTENTIONALLY LEFT BLANK

I. INTRODUCTION

A. BACKGROUND AND CONCEPT

Hypersonic flight was ushered in with the space age using the blunt body aerodynamics made popular with the Mercury capsules and Apollo missions in the 1960s and 1970s. Today, hypersonic flight using blunt body aerodynamics is considered ordinary and rather routine. For example, space shuttle missions receive little attention and are not considered front-page news unless there is controversy or disaster.

Slender and sleek hypersonic aircraft are still considered to be in their infancy but they have been in development just as long as the blunt body vehicles. While the blunt hypersonic vehicles have enjoyed the limelight, research and experimentation for the sharp hypersonic aircraft have been conducted in the background or in secrecy beginning with the X-15 in 1957, followed by the XB-70 Valkyrie in the mid 1960s. More recent research and development has been accomplished with the National Aerospace Plane (NASP or X-30) in the 1980s and the X-43 Hyper-X in 2001.

Slender vehicles in hypersonic flight may someday be as commonplace as a typical commercial airplane or military aircraft, but not until they can be operated and maintained in an efficient manner with proven technology and a complete understanding of all engineering principles. Once the aerodynamics, engineering, propulsion and technology mature, modern hypersonic aircraft will have many worthwhile applications including; single-stage-to-orbit vehicles, long-range planetary probes, maneuvering reentry vehicles (MaRV), hypersonic glide vehicles (HGV) as discussed in [Ref. 1].

A particular type of hypersonic aircraft designed to "ride" a shockwave created at hypersonic speeds is called a waverider. At the design Mach number, the waverider body has an attached shock along the leading edge, keeping the high pressure on the lower surface isolated from the upper surface. The separation of upper and lower surface flow results in a dramatic reduction of drag and a potentially significant higher lift-to-drag ratio (L/D) compared to more common configurations at the same Mach number. See Figure 1.1 for an example of a waverider and a generic hypersonic vehicle.

1

The origin of the waverider concept can be traced back to an experiment conducted by NASA research engineer, Dr. Alfred Eggers, in 1955. Dr. Eggers achieved a sixty-percent increase in L/D at Mach 5, over the technology of the time period, by creating a test vehicle with wing taper that matched the Mach 5 shock wave [Ref. 2]. A NASA research memorandum was released in 1956 detailing the breakthrough results obtained by Dr. Eggers' research. This research memorandum was made available to authorized aircraft companies. North American Aviation seized the day and used the new technology to design a long-range bomber known as the B-70 Valkyrie [Ref. 3].
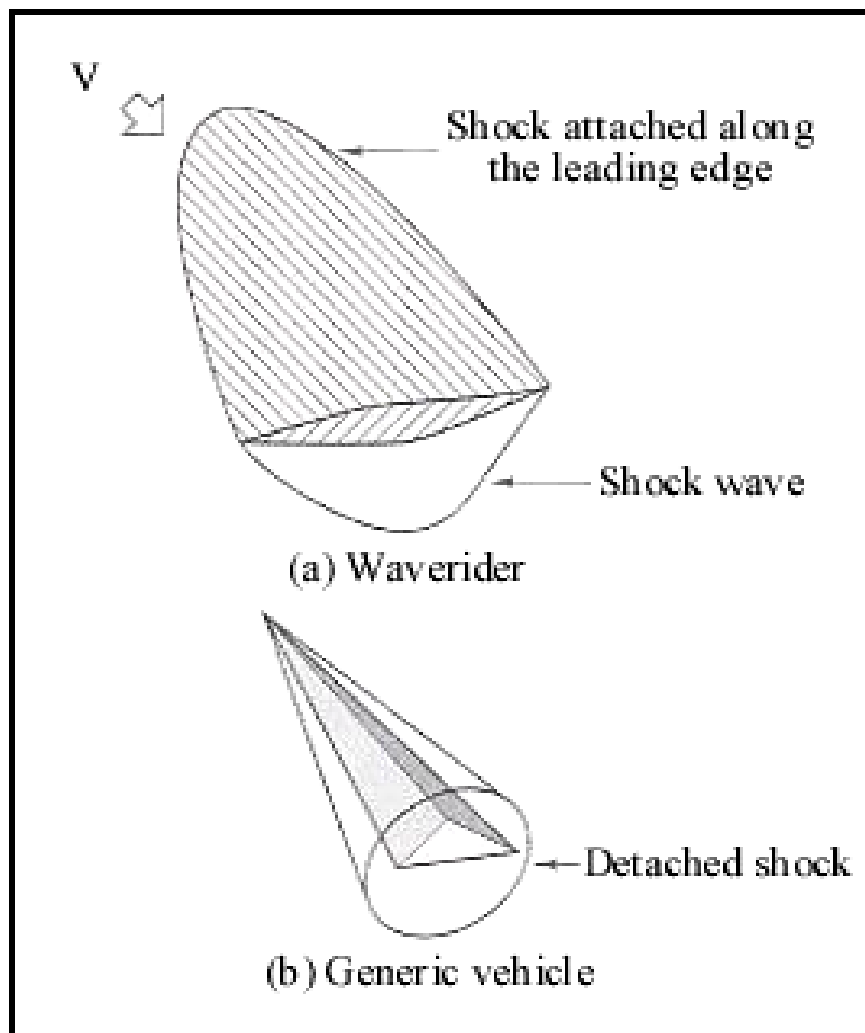
Figure 1.1.   Hypersonic Vehicles copied from Ref. 4 Fig. 12.22: (a) waverider, (b) generic vehicle.

In 1959, T. R. F. Nonweiler introduced the waverider concept of a three-dimensional body optimized using a theoretical wedge flow field. Nonweiler proposed all-wing delta planform designs with caret shaped cross sections in order to keep the shock wave attached at the design Mach number and angle of attack (AOA) [Ref. 4]. Two examples of Nonweiler's proposed waveriders are shown in Figure 1.2. Nonweiler's waveriders did not achieve the expected breakthrough results due to increased drag associated with the high skin friction from the large wetted area of the delta-planform caret-cross-section designs [Ref. 4].
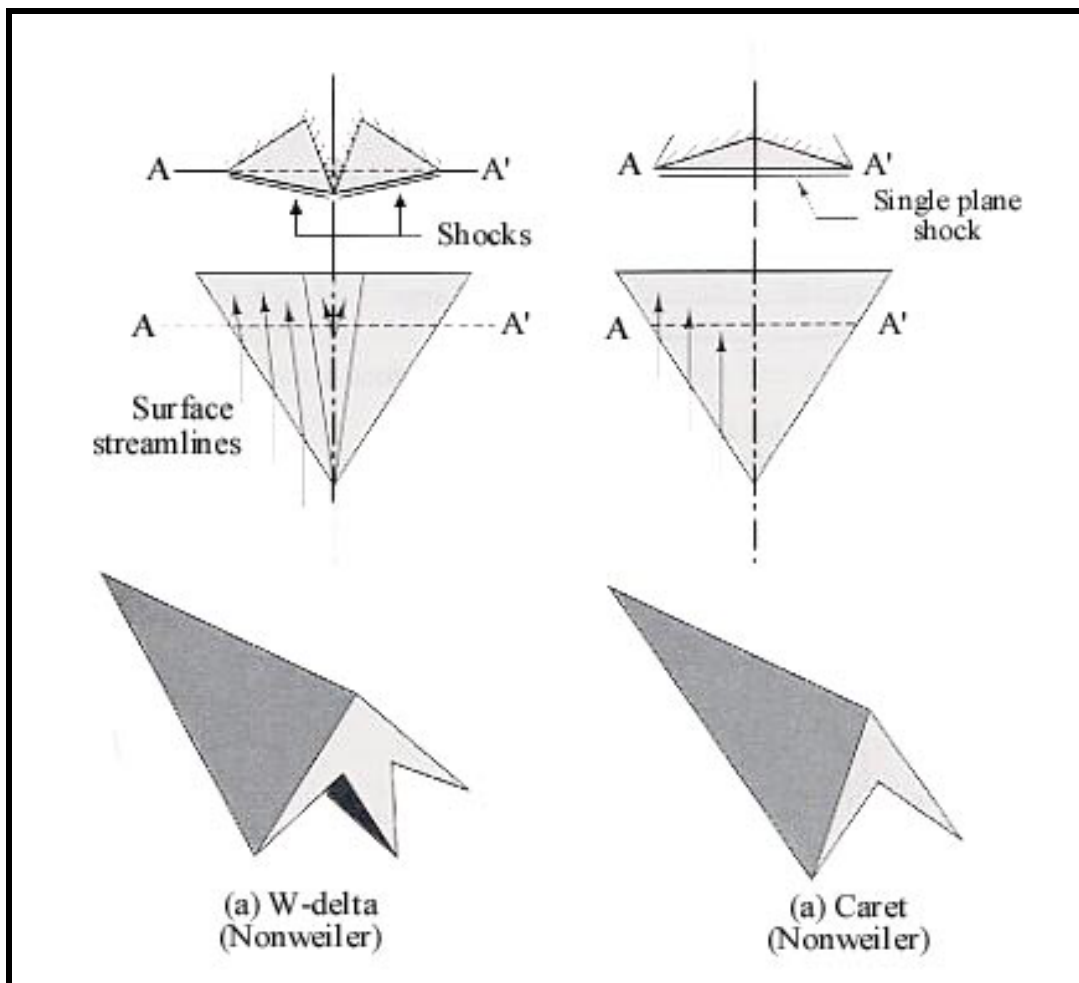
Figure 1.2.   Nonweiler's waverider proposals copied from Ref. 4 Fig. 12.20.

The next waverider advancement occurred in 1968 with the introduction of waveriders optimized for conical flow (axisymetric flow over a right circular cone) by J.

Seddon and A. Spence [Ref. 5]. Advancements in analytical methods allowed a conical flowfield to be simulated resulting in a new waverider shape. Figures 1.3 and 1.4 depict waveriders developed from early conical flow theory. In 1980 the theory was extended by M. L. Rassmussen to include configurations derived from inclined circular and elliptic cones for use in angle of attack studies [Ref. 2]. However, waveriders using these advancements were unable to achieve results beyond Kuchemann's theoretical $(L/D)_{max}$ boundary [Ref. 4]:

$$(L/D)_{max} = \frac{4(M_\infty + 3)}{M_\infty} \tag{1}$$
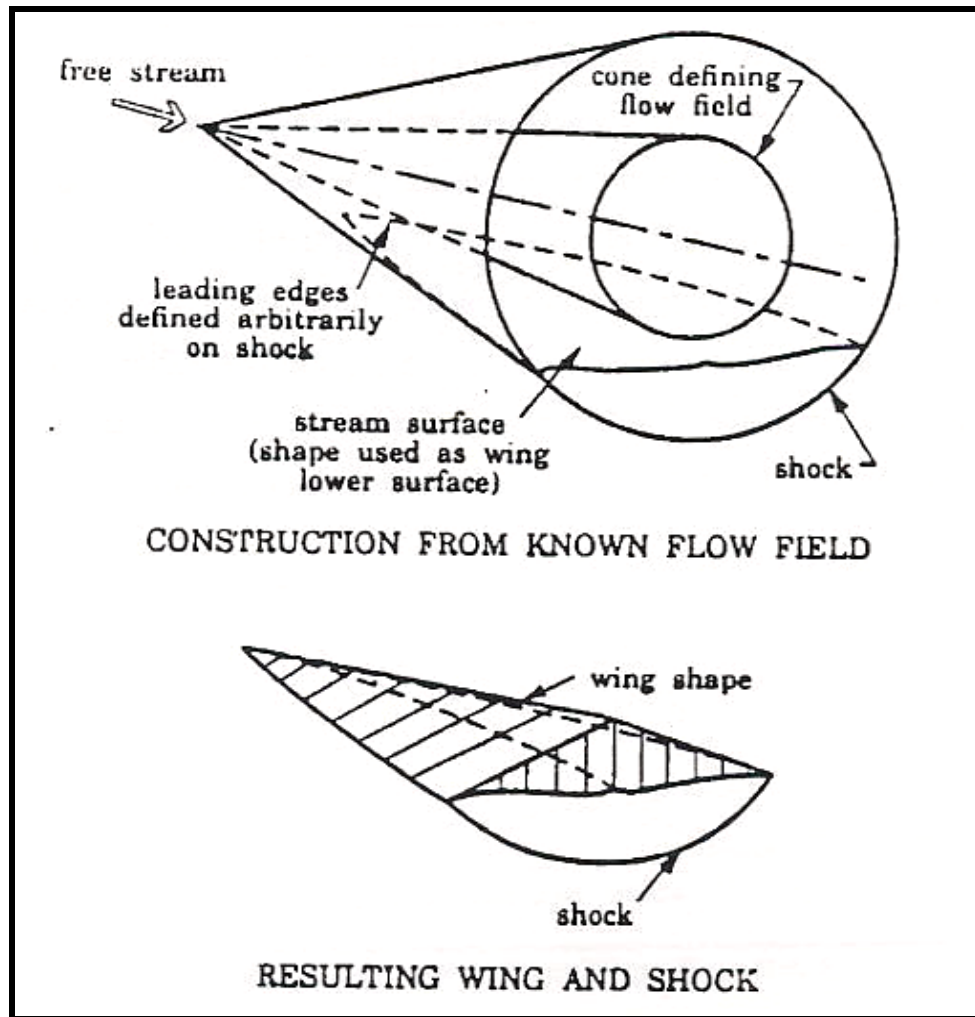
Figure 1.3. **Waverider construction from conical flow field copied from Ref. 1.**

4
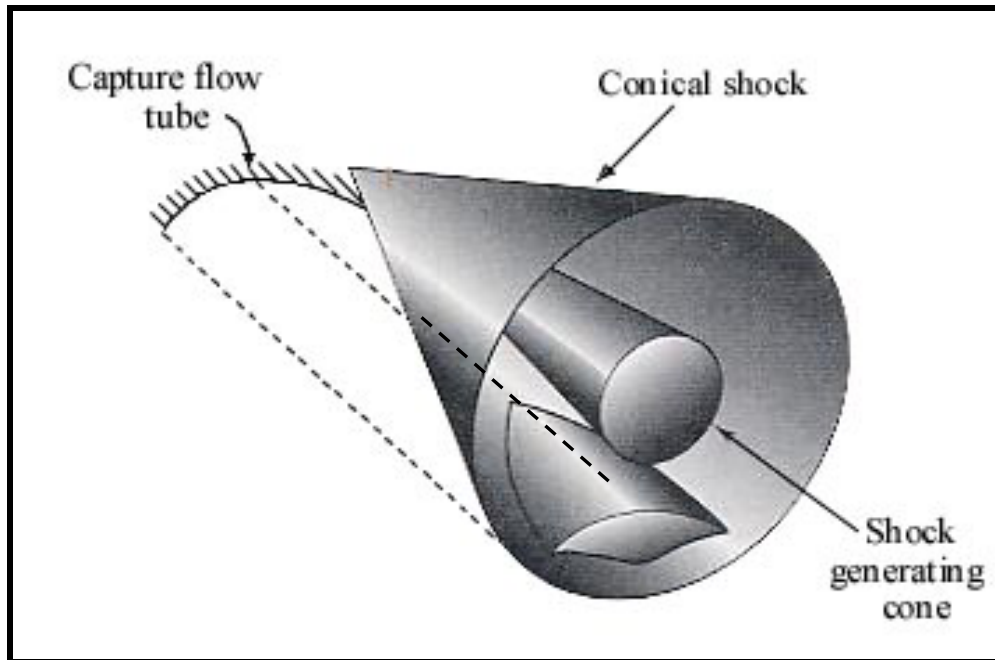
Figure 1.4.   Conical flow field and shock copied from Ref. 4 Fig. 12.24.

Upper surface flow separation and lower surface shock interaction are a couple of flow similarities between thin delta wings and waverider shapes, due to the fact that the flow becomes conical at high Reynolds numbers. Studies involving supersonic and hypersonic flows over delta wings by L.C. Squire were being conducted simultaneously with waverider research in the 1970s. Squire indicates that there are three types of flow for delta wings (and waveriders) that are a function of Mach number and angle of attack. Illustrations and a graphical depiction of the flight envelopes of the different flow regimes can be found in Figure 1.5 [Ref. 6]. The first flow regime (A) consists of a detached lower shock allowing interaction between the upper and lower surfaces. It exists at subsonic and transonic speeds and may occur at low supersonic speeds depending on the vehicle configuration.   The second flow regime (B) occurs at supersonic speeds below the waverider or delta wing design Mach number. The shock is still detached, but close enough to the leading edge that the high-pressure flow from the lower surface reaches Mach 1 before it can influence the upper surface. The third flow regime (C) occurs at the design Mach number of the vehicle. The shock is attached to the sharp leading edge of the waverider, splitting the upper and lower surfaces into two distinct and separate flow regions [Ref. 6].
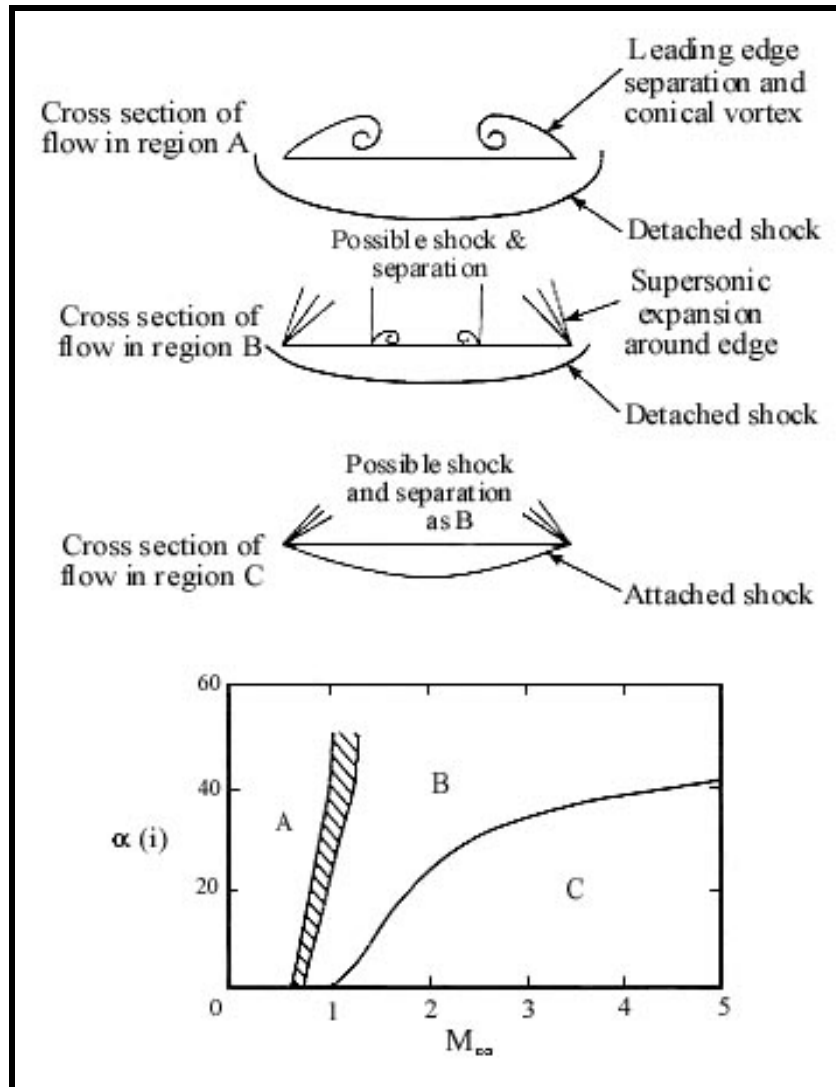
Figure 1.5.   Flow regimes for delta wings and waveriders copied from Ref. 6.

Waverider theory improved significantly in 1987 when K. G. Bowcutt and J. D. Anderson, Jr. presented their paper on viscous optimized waveriders at the AIAA 25th Aerospace Sciences Meeting [Ref. 7].   Bowcutt and Anderson used a non-linear numerical optimization process that represented the undersurface flow as an inviscid conical flow field and the upper surface flow as inviscid flow over a tapered cylinder. The viscous effects are calculated using two-dimensional boundary layer flows that follow the respective upper and lower surface streamlines.   Laminar boundary layer calculations were performed using Walz's integration method, while the turbulent boundary layer calculations were completed using an inner variable method [Ref. 7].

6

The result obtained by including viscous effects was a subtle but extremely important change in the overall design of waveriders. Each theoretical waverider design is unique because it is shaped according to the boundary layer transition criteria used in the optimization process. See Figure 1.6 for examples of optimized waveriders. The refined design extended the theoretical $(L/D)_{max}$ boundary and established a new one following the rule [Ref. 4]:

$$(L/D)_{max} = \frac{6(M_\infty + 2)}{M_\infty} \qquad (2)$$

Figure 1.7 graphically illustrates Kuchemann's theoretical $(L/D)_{max}$ boundary and the new theoretical $(L/D)_{max}$ boundary developed from the work completed by Bowcutt, Anderson and Corda [Refs. 7, 8 and 9].
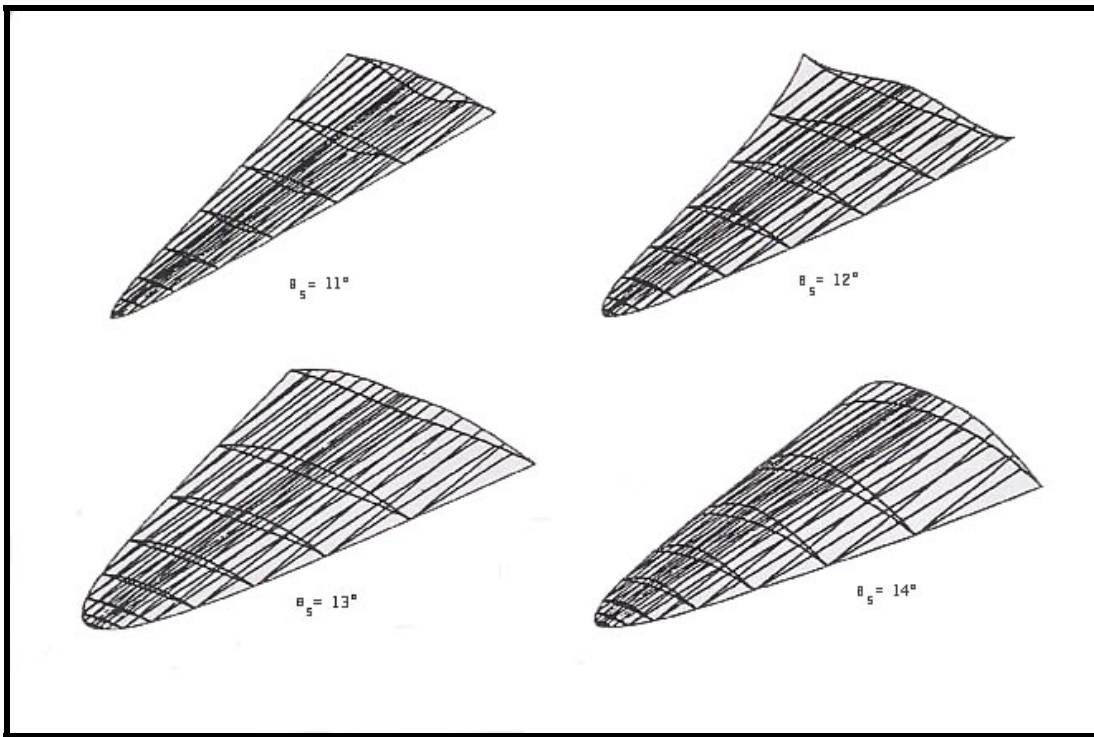
Figure 1.6.   Examples of viscous optimized waveriders copied from Ref. 7 Fig 13.
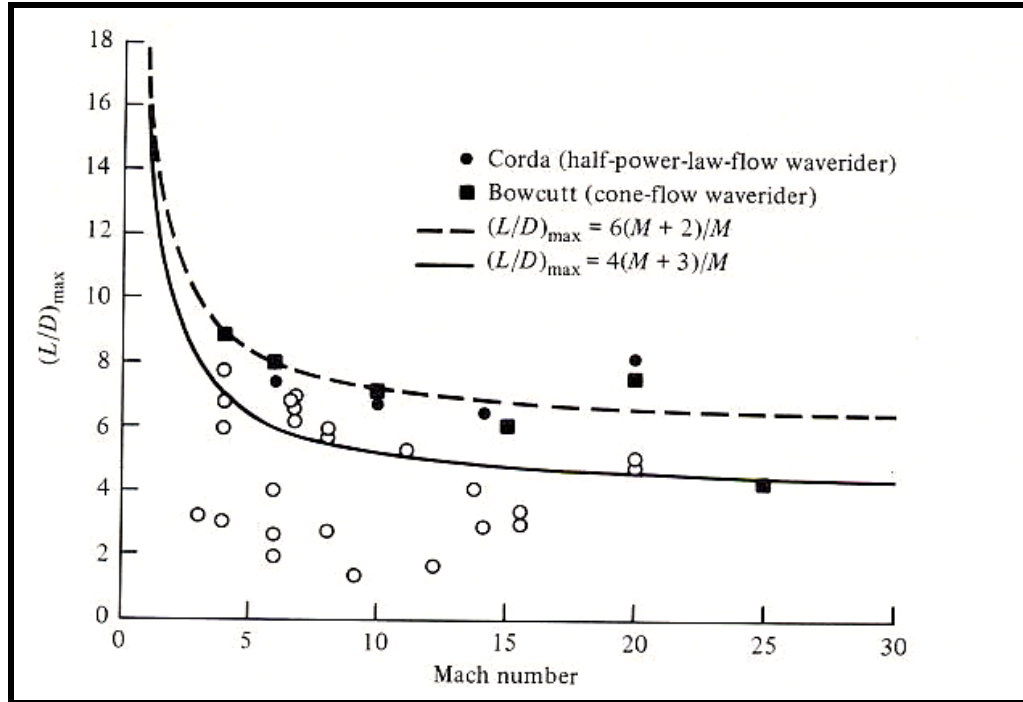
Figure 1.7.   **Maximum L/D boundaries copied from Ref. 10 Fig. 10.7.**

In 1988, D. L. Vanhoy compared the subsonic performance of the Mach 6 viscous optimized waverider, designed by Bowcutt and Anderson, with a sharp edge delta wing with a similar length, span and thickness. His work extended Squire's flow theory by indicating that the waverider and delta wing have similar characteristics in upper surface (vortical) flow, drag and L/D [Refs. 2 and 11].

The latest significant waverider improvements were accomplished in 1998 with the introduction of the osculating cone technique [Ref. 12] and the star body variation [Ref. 13]. The oscul cone method is a variation of the conical-flow techniques using multiple cones to simulate non-axisymmetric shock patterns enabling a designer to incorporate vehicle features such as: engines, canopies and control surfaces. Figure 1.8 is an example of a Mach 6 waverider designed using the osculating cone method. The star body is developed from superimposing multiple conical flow waveriders and joining them at the leading edge. Theoretically, a 20% reduction in wave drag is accomplished when the shock attaches to each of the star fins [Ref. 14]. Figure 1.9 is a picture of a Mach 6.4 star body.

8
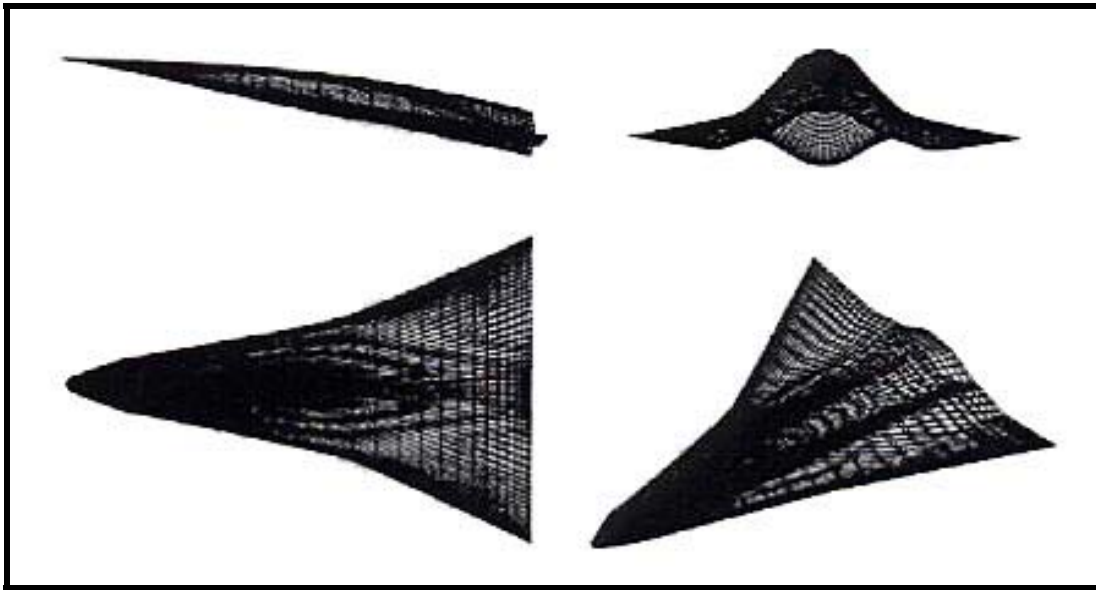
Figure 1.8.   Mach 6 waverider designed by the osculating cone method copied from Ref. 12.
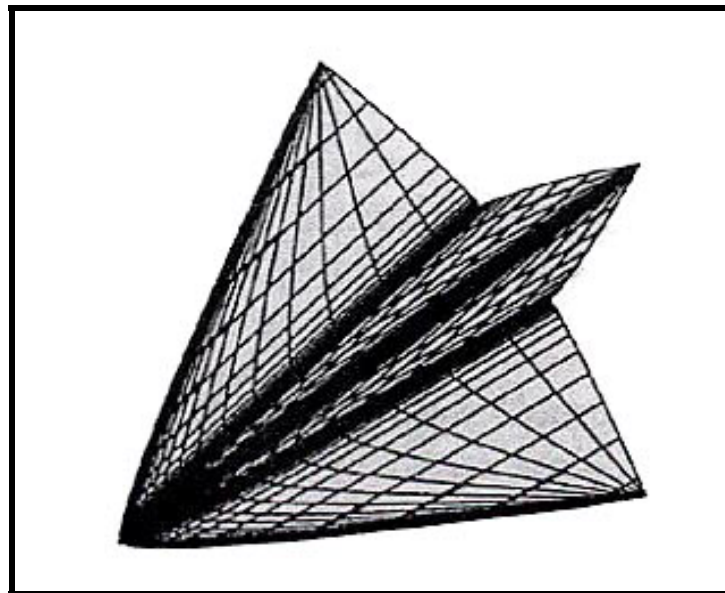
Figure 1.9.   Mach 6.4 star body copied from Ref. 13.

B.   NPS RESEARCH

Waverider research at the Naval Postgraduate School (NPS) began in the aircraft design class (AA 4273) in 1992 and was quickly advanced by D. R. Price's 1993 thesis defining the design of a carrier-launched Mach 6 interceptor. Price generated the waverider shape with the help of the Systems Analysis Branch at NASA Ames Research Center and their Hypersonic Aircraft Vehicle Optimization Code (HAVOC). The design was based on inviscid conical flow theory and was optimized for maximum $\left(\dfrac{L}{D} I_{SP} \right)_{max}$ at Mach 6 and with scramjet propulsion. Figure 1.10 contains an orthographic projection and an isometric view of Price's final waverider design.

In 1994, the study of the Price waverider continued with the hydrodynamic flow field study and low-speed wind tunnel testing by L. M. Johnson [Ref. 2] and M. E. Cedrun [Ref. 15] respectfully. Johnson studied the waverider vortex flow field using an 8-inch root chord aluminum model in the NPS Flow Visualization Water Tunnel facility which has a 15-inch wide, 20-inch high and 60-inch long test section. Angle of attack (AOA or α) sweeps were conducted from 0˚ to 20˚ with yaw (β) sweeps from 0˚ to 10˚. Cedrun used a 15-inch root chord aluminum model in the NPS horizontal low speed wind tunnel with a 45-inch wide, 28.4-inch high and 4-feet long test section. Force and moment wind tunnel data were collected using a six-degree-of-freedom sting balance; tufts were used for flowfield visualization. In 1998, M. R. Huff [Ref. 16] developed an automated data acquisition system for the horizontal NPS subsonic wind tunnel and used the system to replicate Cedrun's force and moment results for the Price waverider.

10
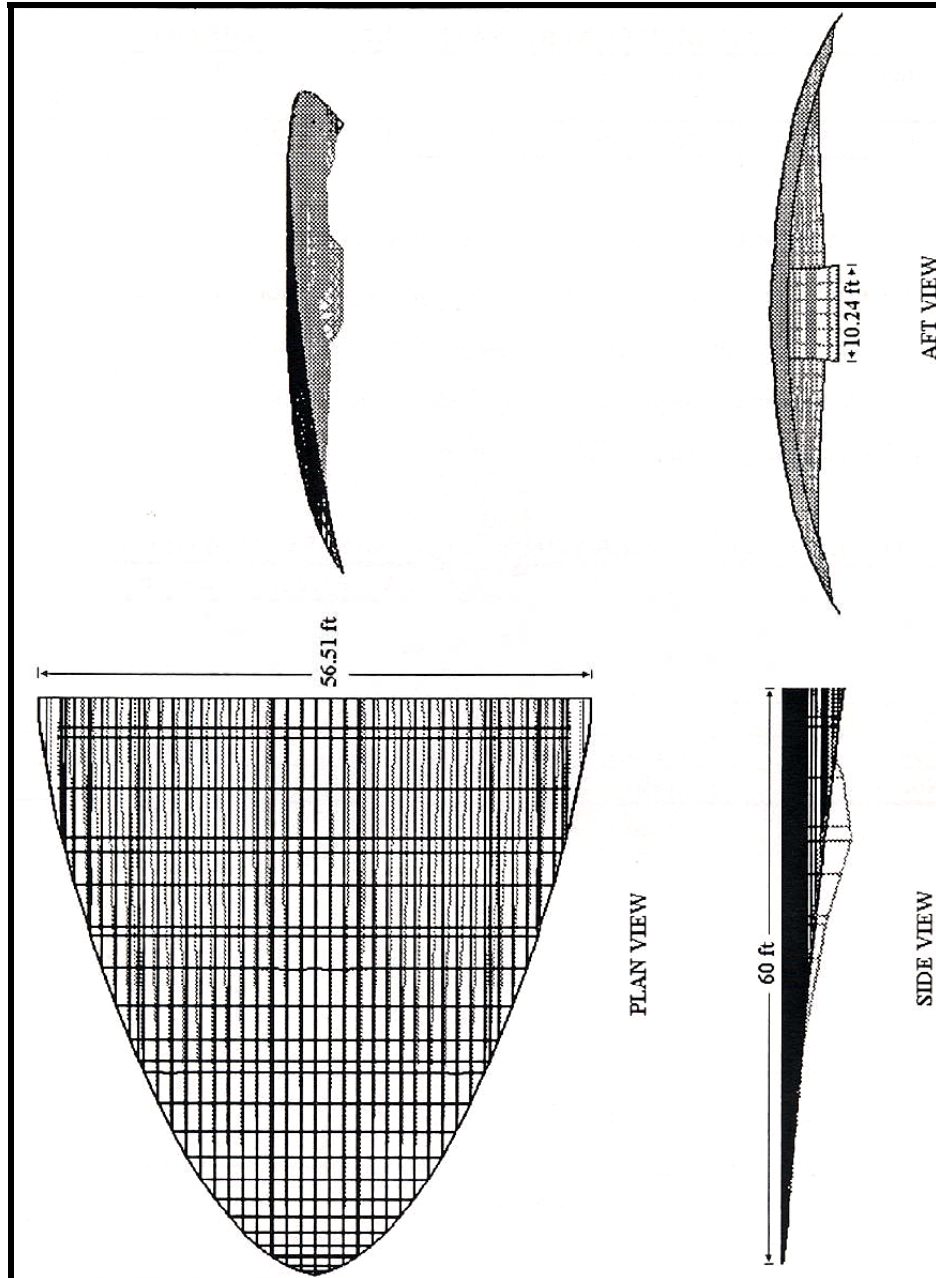
Figure 1.10.   Price waverider design copied from Ref. 1.

The last NPS study involving the Price waverider was a computational fluid dynamic (CFD) analysis conducted by E. Coyne [Ref. 17] in 1999. The analysis determined the theoretical force, moment, pressure distributions and Mach contours for a range of Mach numbers from 0.3 to 6.0. One angle of attack sweep at Mach 0.3 was incorporated into the CFD analysis with results that compared favorably with the wind tunnel data gathered by Cedrun and Huff.

11

C.   SUPERSONIC WIND TUNNEL TESTING

Supersonic (and subsonic) wind tunnel testing is a research tool useful for corroborating high-speed (and low speed) theoretical results, and for pure experimentation when theory is lacking or non-existent [Ref. 18].   The wind tunnel provides airflow under controlled conditions allowing aeronautical engineers to test items of interest [Ref. 19].

Prior to experimentation, it is useful to discuss the basic principles involved in supersonic wind tunnels. A supersonic flow is created, in its most basic sense, by a large pressure differential and a convergent-divergent nozzle.   The pressure differential between the plenum and test section forces the air to flow. The convergent portion of the nozzle accelerates the flow to Mach 1 at the throat and the divergent portion of the nozzle further accelerates the flow to its specified Mach number; dependent on the ratio of the final nozzle area to the throat area (A_n/A_{th}). In addition to the plenum and convergent-divergent nozzle, modern supersonic tunnels include diffusers, heaters, dryers, etc. The components of the NPS supersonic wind tunnel will be discussed later.

During supersonic wind tunnel operations there are three important flow phases that require different pressure ratios; tunnel start, normal shock in the test section (transition), and continuous operation. A graph depicting the tunnel compression ratio, λ, (plenum or total pressure to diffuser exit or static pressure ratio; p_t/p_s) versus Mach number required for theoretical (dashed) and actual (solid) supersonic wind tunnel operation is depicted in Figure 1.11 [Ref. 19]. Illustrations of supersonic wind tunnel operating phases are portrayed in Figure 1.12.
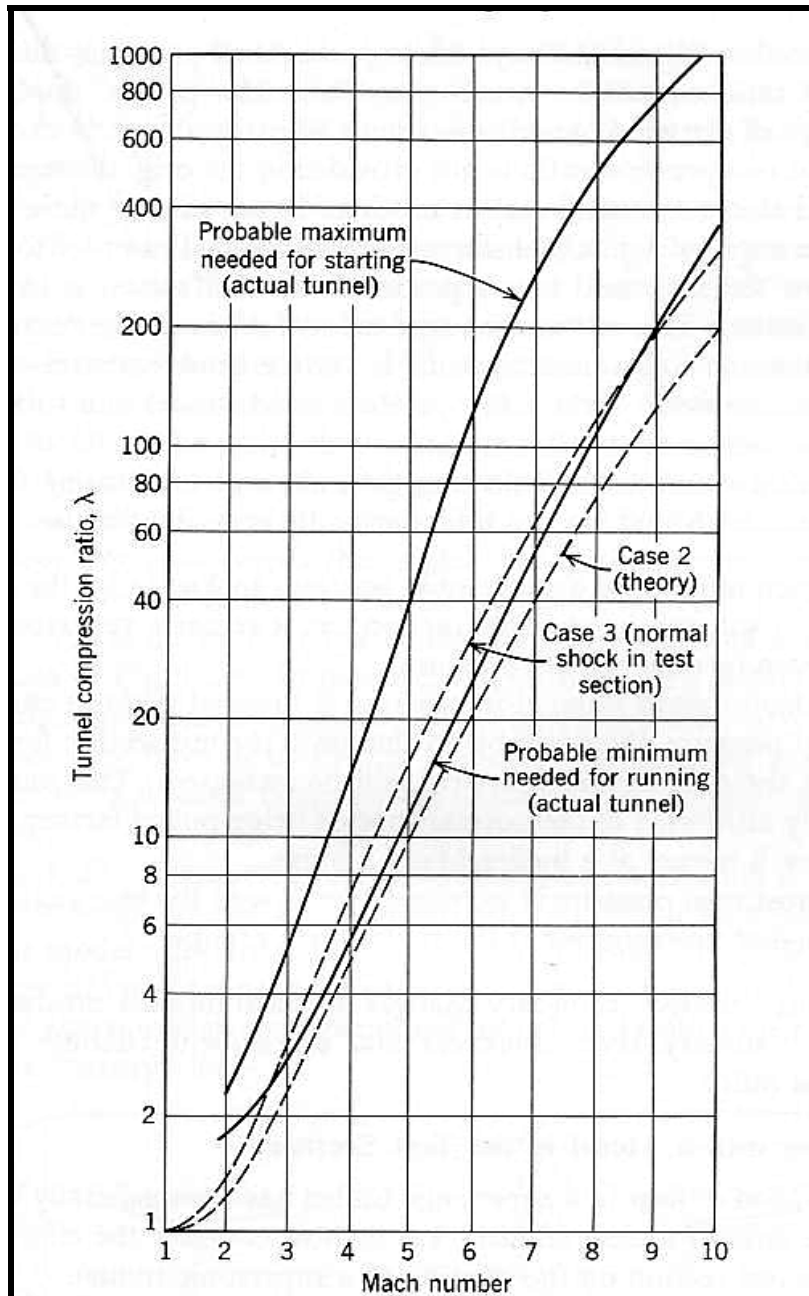
Figure 1.11.   Tunnel compression ratio versus Mach number copied from Ref. 19 Fig 1:25.

Supersonic tunnel starting is a transient flow phase, and is a very important process requiring the largest pressure ratio of the three operational phases. During the tunnel start phase, an unfavorable pressure gradient interacts with the boundary layer as the flow passes through the convergent-divergent nozzle creating large system losses

13

requiring a larger pressure differential between the plenum and test section. In order to overcome the dominating viscous effects associated with the boundary layer, tunnel compression ratios are required to be at least twice as large as the normal shock pressure ratio (p_{t_1}/p_{t_2}). Starting pressure ratios can be reduced using an adjustable convergent-divergent nozzle to start the tunnel at a lower Mach number. The nozzle is used to gradually increase the Mach number after the tunnel has started.
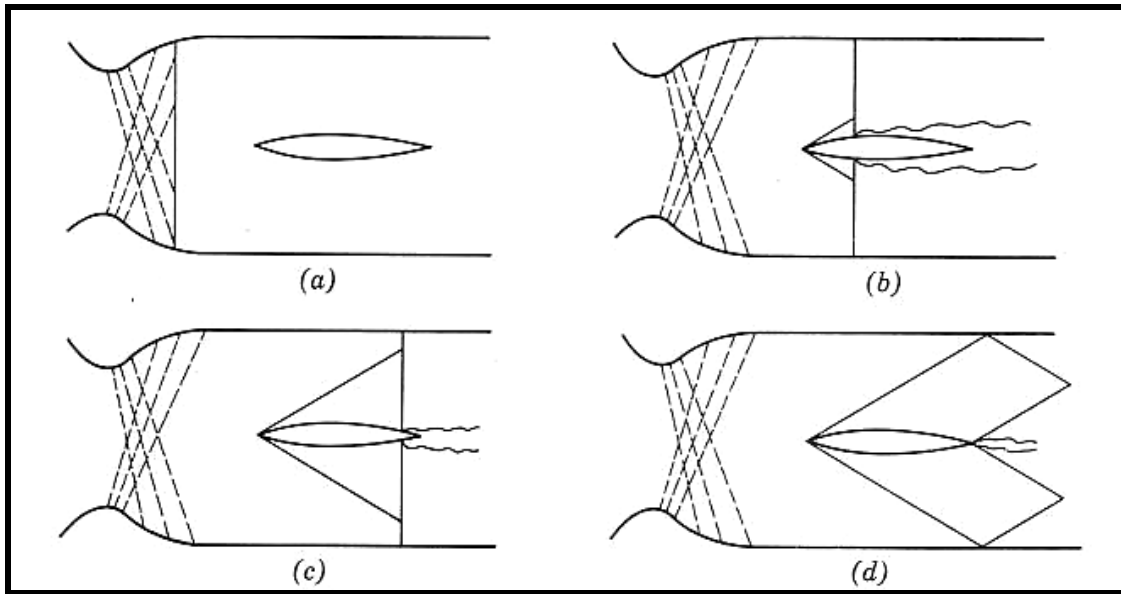
Figure 1.12. Phases of the supersonic wind tunnel, from tunnel start (a) to continuous operation (d), copied from Ref. 19 Fig. 1:26.

The effect of placing a model in the test section is another important design aspect that must be considered before any testing can take place. The maximum size of the model is dependent on several factors. First, during the tunnel start phase, the model must be small enough to allow the mass flow from the nozzle to pass through the test section without accelerating the flow greater than Mach 1. If the normal shock formation (depicted in Figure 1.12 by illustrations b and c) is not allowed to progress over the model, the tunnel will become choked and continuous operating conditions will never be reached. Figure 1.13 is an initial model-sizing guide using the ratio of the model diameter (d_m) to the test section cross sectional area (A) versus Mach number. This guide was developed using theory and experimental data gathered from several supersonic wind

14

tunnels [Ref. 19]. The model diameter is based on circular bodies and requires an equivalent diameter calculation for non-circular shapes. Further experimentation indicates that blunt models may require their size (diameter) to be reduced below the "actual" line while sharp models have permitted starts above the theoretical line [Ref. 19]. The model cross-sectional area should be checked over the range of AOA to be tested in order to ensure that the model does not block or "choke" the flow in the test section as the AOA is increased. Additionally, the model size (length) should be checked for shock interactions with the test section walls for all expected configurations.
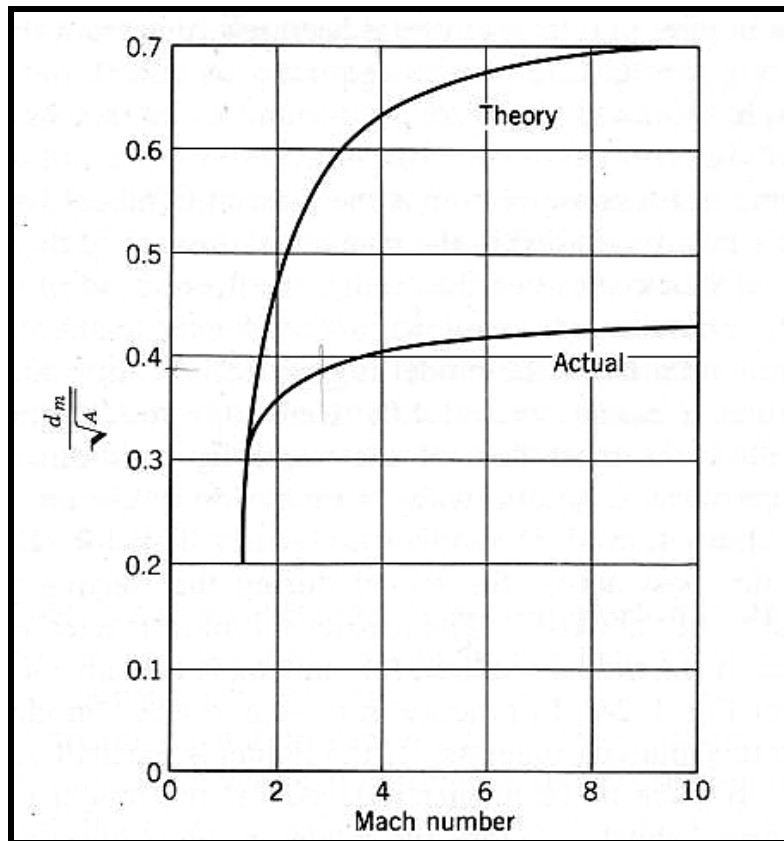
Figure 1.13.   Model sizing chart copied from Ref. 19 Fig 1:27.

Flow acceleration (nozzle expansion) creates dramatic temperature and pressure drops through the convergent-divergent nozzle that can lead to air condensation and liquefaction resulting in inconsistent and inaccurate wind tunnel measurements, if the air

15

supplying the wind tunnel is not dried and heated before flowing through the nozzle blocks and test section. Heating increases the total temperature, averting liquefaction of the moisture in the air. Liquefaction generally does not occur below Mach 4.

A final important wind tunnel test parameter is the Reynolds number. The Reynolds number is highly dependent on temperature and will determine the boundary layer characteristics (laminar or turbulent), define the boundary layer thickness, influence the drag (skin friction and wave drag) and determine whether or not the theory used for estimating or measuring model forces is valid by indicating whether or not the flow is in the continuum region.

D.   PURPOSE

The purpose of this experimental thesis is to determine notional supersonic flow characteristics of the Mach 6 Price waverider planform using pressure sensitive paint and shadowgraph photographs. The experiments were conducted over a modest range of Mach numbers ($1.7 \leq M \leq 4$) at angles-of-attack of $0°$, $2°$ and $4°$. The relative pressure distribution from the pressure sensitive paint and shock characteristics from the shadowgraph photography will provide useful information for follow-on work (using another planform or an actual scaled model) by providing insight into pressure tap location, shock location and vortex interaction. The pressure sensitive paint results of this thesis were compared to the pressure data in the CFD analysis by E. Coyne and to the vortical flow results from L. M. Johnson's hydrodynamic studies. Shock strength and location obtained from the shadowgraph images was also compared to CFD results. Additionally, the experiments conducted in the NPS supersonic wind tunnel provided useful experience in supersonic wind tunnel research at the Naval Postgraduate School.

II. APPARATUS

A. SUPERSONIC WIND TUNNEL

The NPS supersonic wind tunnel is located in the Gas Dynamics Laboratory (Building 216) as part of the M. H. Vavra Turbopropulsion Laboratory complex. The supersonic wind tunnel is an intermittent blow-down tunnel that shares its air supply with a transonic wind tunnel and an unmanned air vehicle (UAV) engine test stand in the Gas Dynamics Laboratory, as well as the rotor spinpit in the turbomachinery laboratory.

The compressed air supply of the NPS blow-down supersonic wind tunnel is provided by a compressor, dryer and boost pump located in the compressor room in Building 216. The three-stage centrifugal Elliot compressor is driven by a 4160-volt 600-HP electric motor and is capable of compressing atmospheric air from 14.7 psia to 150 psig. Figure 2.1 is a schematic of the NPS supersonic wind tunnel and corresponding air supply. After leaving the compressor, the high pressure air is routed through a Hydronix Desiccant Dryer where the moisture is removed. The dryer is composed of two drying tanks in parallel. Each tank operates separately; while one dryer is removing water vapor from the air and filling up with water, the second dryer is draining or in stand-by mode. At this point, the air can either be channeled directly to the storage tanks at 140 psig (after line losses) or it can be compressed further by being routed through the boost pump. The Ingersol Rand boost pump is a reciprocating piston pump that doubles the compression from 150 to 300 psig. The boost pump is belt driven by a 440-volt 150-HP Westinghouse motor. Air leaving the compressor room is routed to storage tanks located outside. Pictures of the compressor, dryers and boost pump are shown in Figures 2.2, 2.3 and 2.4, respectively.

The outdoor storage facility consists of four 2,000-cubic-foot storage tanks resulting in a total capacity of 8,000 cubic-feet. The outdoor compressed air storage facility is commonly referred to as the "tank farm." Each tank is rated at 300 psig and is capable of being individually isolated. During the test period, three tanks were utilized

resulting in 6000 cubic-feet of storage. Figure 2.5 is a picture of the tank farm. Air leaving the tank farm is directed to the laboratory.
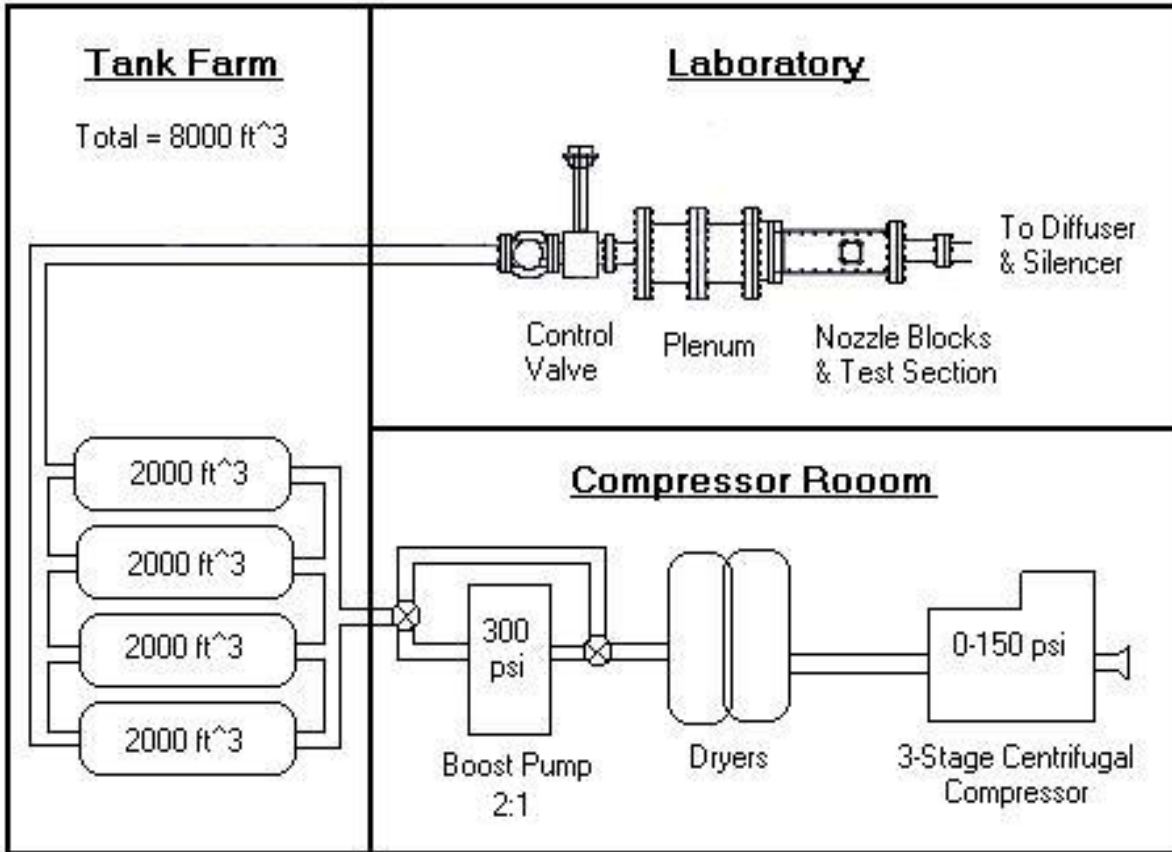
Figure 2.1.   NPS supersonic wind tunnel schematic.

In the gas dynamics laboratory, air is channeled to the supersonic wind tunnel via the Fisher (type 57-T) pneumatic control valve. Air flowing through the control valve enters the plenum where the pressure is recorded using a static pressure port and the temperature was recorded by inserting a standard J-type thermal couple attached to a digital readout. High-pressure low-velocity air leaving the plenum flows through the convergent-divergent nozzle blocks and into the wind tunnel test section. The nozzle blocks are two-dimensional fixed nozzles that must be manually changed to vary the test section Mach number. The supersonic wind tunnel test section is 4-inches wide and 4-inches in height. Figure 2.6 shows the pneumatic control valve, plenum, nozzle blocks

18

and test section. Air leaving the test section is slowed by a fixed diffuser and is routed outside to a silencer before being vented to the atmosphere.
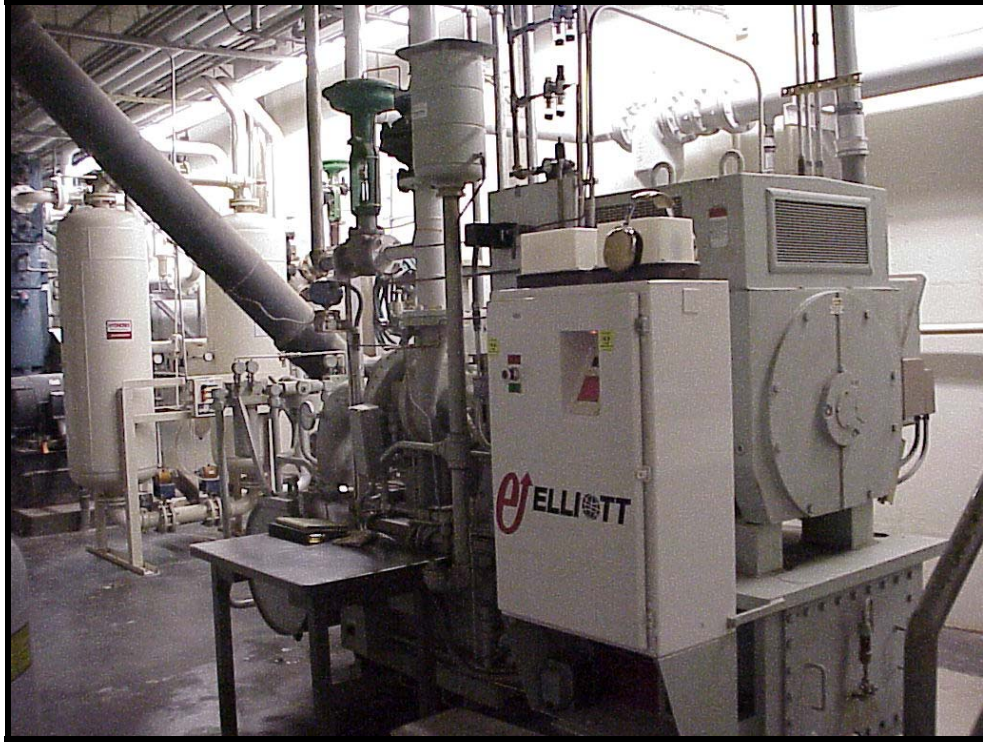
Figure 2.2.   Elliot 3-stage centrifugal compressor.

The test section has two circular planar side windows for observing the model in the test section and a static pressure port (located just upstream of the windows) for test-section static pressure measurements. The circular windows are 6-inches in diameter and are made of glass. The static pressure port can be seen just to the right of the window (upstream) in Figure 2.7.

Figure 2.3.   Hydronix desiccant dryers (in parallel).
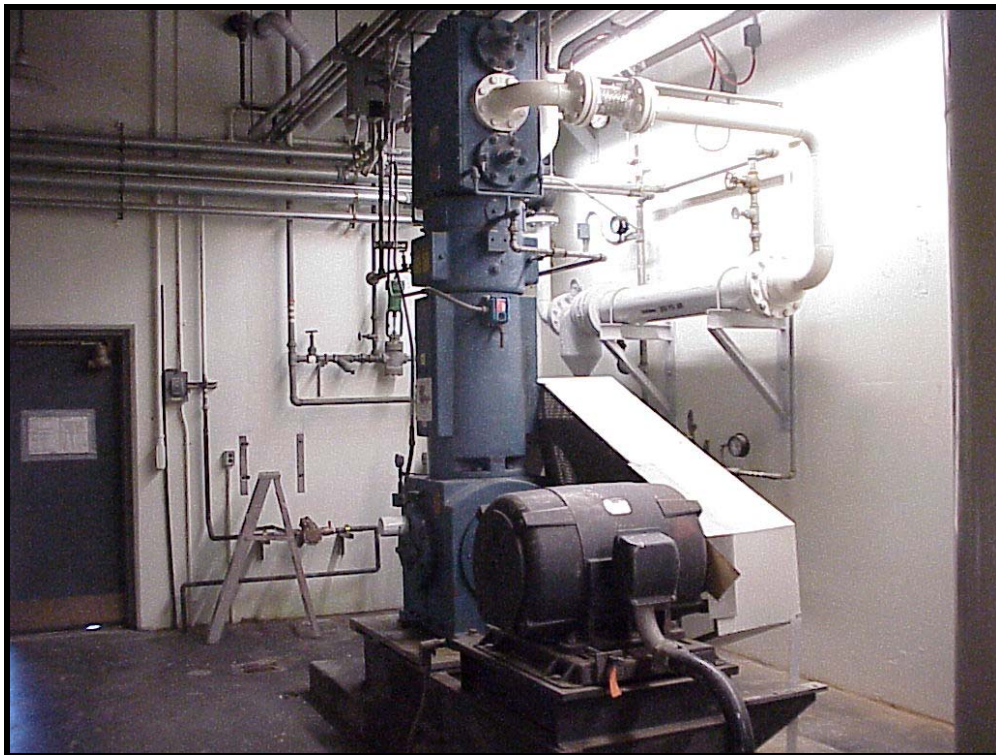
Figure 2.4.   Ingersol Rand reciprocating boost pump.

Figure 2.5.   Gas dynamics laboratory tank farm.
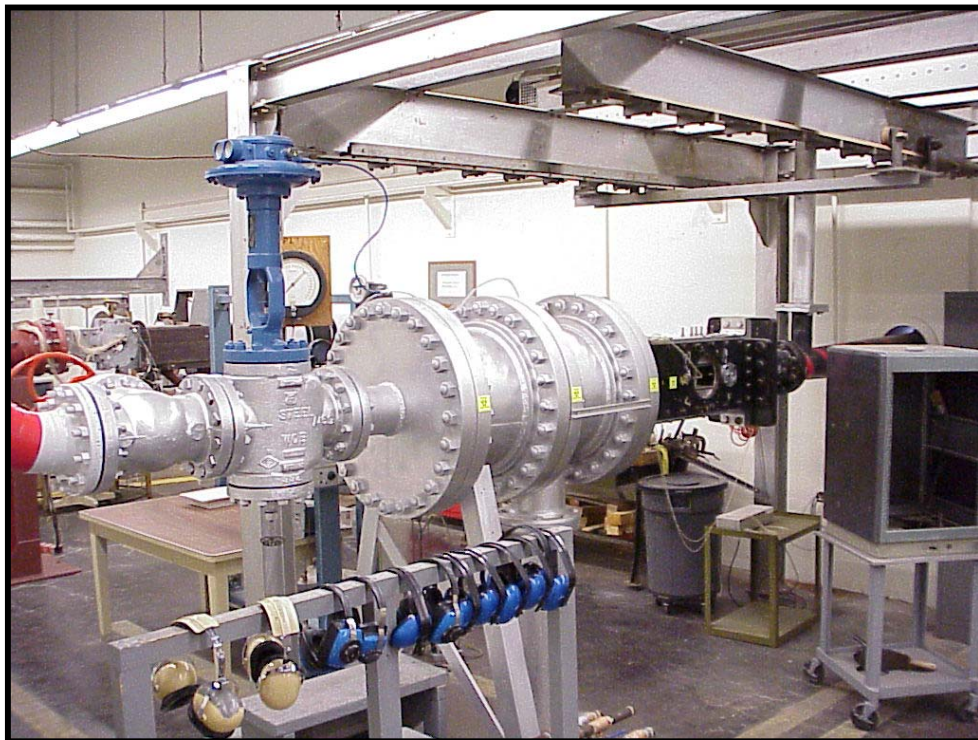
Figure 2.6.   Control valve, plenum, nozzle and test section.
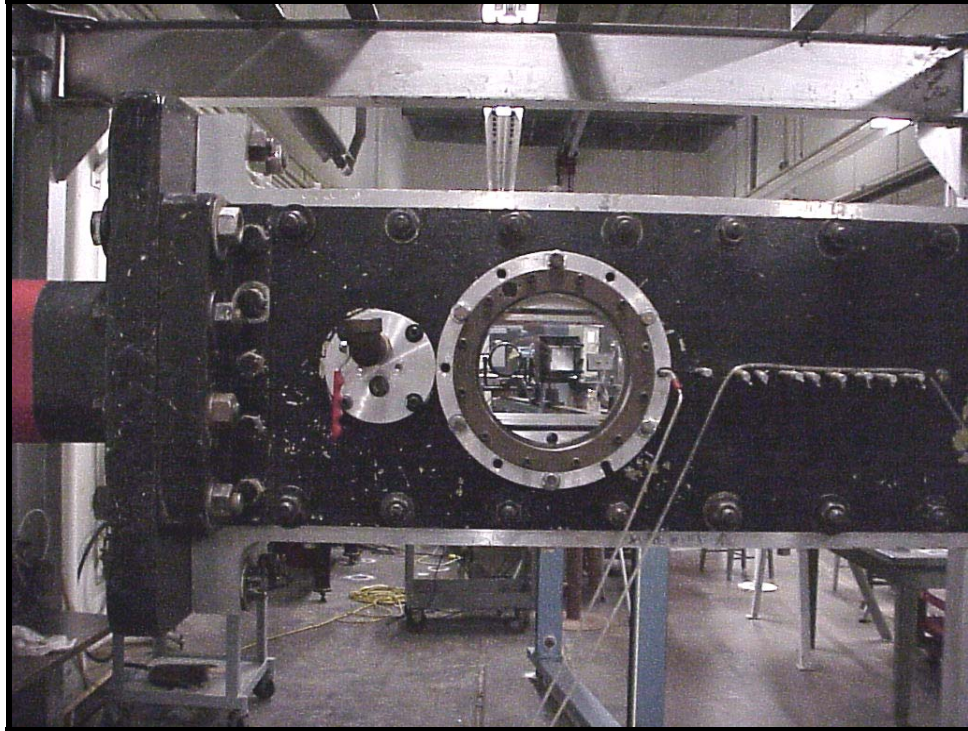
Figure 2.7. **Supersonic wind tunnel test section circular observation window(s), static port and mounting plug.**
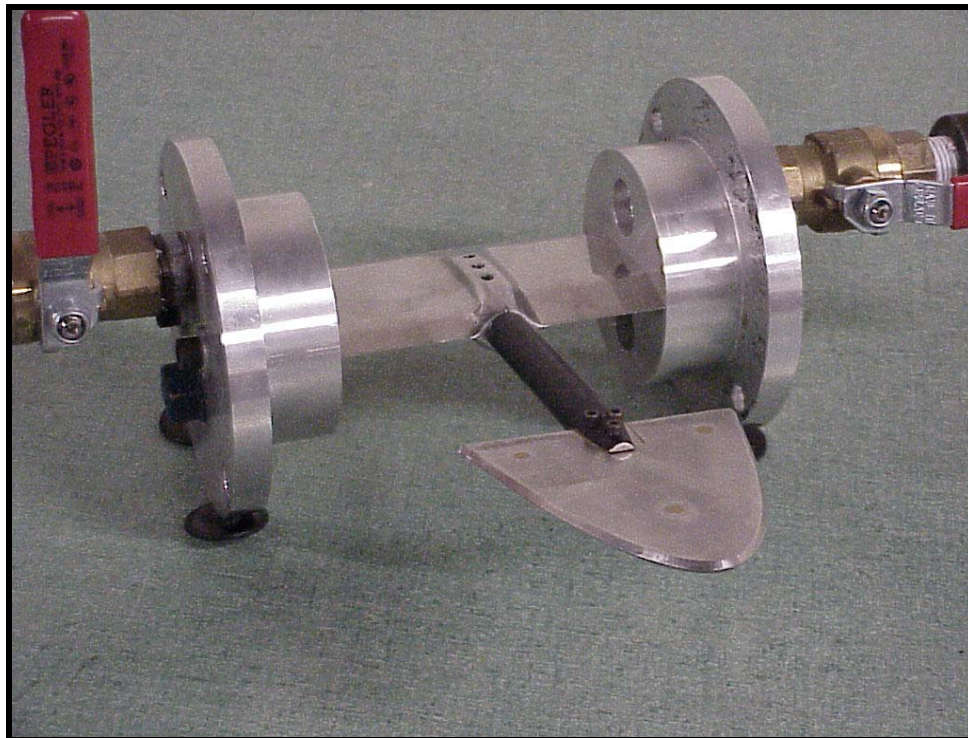
Figure 2.8. **45°-wedge leading edge model, 0° AOA sting, sting mount and mounting plugs.**

The model and sting assembly are connected to the stationary aerodynamic sting mount by two upper and two lower (four total) Allen screws. The sting mount, located downstream of the test section, spans the width of the tunnel and is held in place by two screws in each of the mounting plugs (four total). Figure 2.8 is a picture of the model, sting, sting mount and mounting plugs assembled outside the tunnel.

B.   MEASUREMENT DEVICES

1.   Model

The scaled stainless steel model is a 3.183-inch long flat plate planform of the Price waverider with a maximum width at the base of 3-inches and a maximum thickness of an 1/8-inch. Two model planforms were made; one 45°-wedge leading edge leading edge model and one 15°-wedge leading edge leading edge model. The 45°-wedge leading edge model's leading edge was sharpened at 45° angles (90° enclosed angle) to reduce the flat edge of the planform and to mimic the larger leading edge required for heat dissipation of hypersonic vehicles. The sharp model's leading edge was sharpened to 15° angles (30° enclosed angle) to facilitate better supersonic testing and to mimic the edge that may be used for future hypersonic vehicles when heat dissipation technologies improve. Figure 2.9 is a line drawing of the 15°-wedge leading edge model planform. The model is attached to a 1/2-inch diameter stainless steel sting by three 4-40 carbon steel setscrews. Figure 2.10 consists of an orthographic projection and an isometric view of the 45°-wedge leading edge model with the 0° AOA sting. The model planform leading edge was determined by scaling the planform leading edge equation used for the 14-inch model employed in the subsonic wind tunnel tests conducted by Cedrun [Ref. 15] and Huff [Ref. 16]. MATLAB was used to scale the model and to determine the new planform equation using the polyfit function. Neglecting higher order terms, the equation for the 3.183-inch long planform is:

$$y = -0.0719x^4 - 1.2427x^2 + 3.183 \qquad (3)$$

$$-1.5 \le x \le 1.5$$

23

The NPS supersonic wind tunnel, in its current configuration, utilizes a fixed sting mount requiring a separate sting design for each angle of attack desired for testing. Therefore, three separate stings were designed, in order to obtain the desired test angles of attack of 0°, 2° and 4°. Each sting length of 5 1/2-inches was designed to fit into the sting mount and to allow the complete waverider planform to be seen through the test section window. The overall diameter of the sting is 1/2-inch except at the tip where it is tapered to reduce blockage and minimize shock interactions and at the base where the diameter was reduced to 0.435-inches to match the diameter of the sting mount receiver.
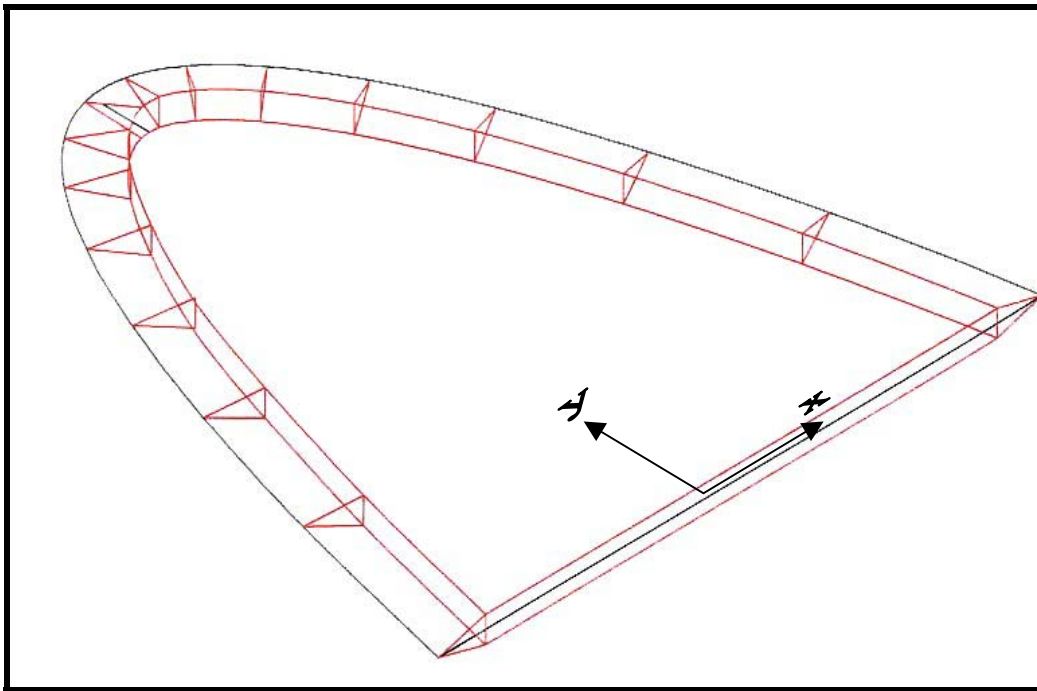
Figure 2.9.   Line drawing of 15°-wedge leading edge planform model.

2.   Shadowgraph and Schlieren

The NPS gas dynamics laboratory shadowgraph and Schlieren optical systems provide non-intrusive methods to view shock waves, boundary layers and transition points. Shadowgraph and Schlieren photography are similar because they both depict changes in density by exploiting changes of the index of refraction. The two methods differ in the density parameter that they exploit. The Schlieren method exploits the

density gradient ($\partial\rho/\partial x$) while the shadowgraph uses changes in the density gradient ($\partial^2\rho/\partial x^2$) to form images.
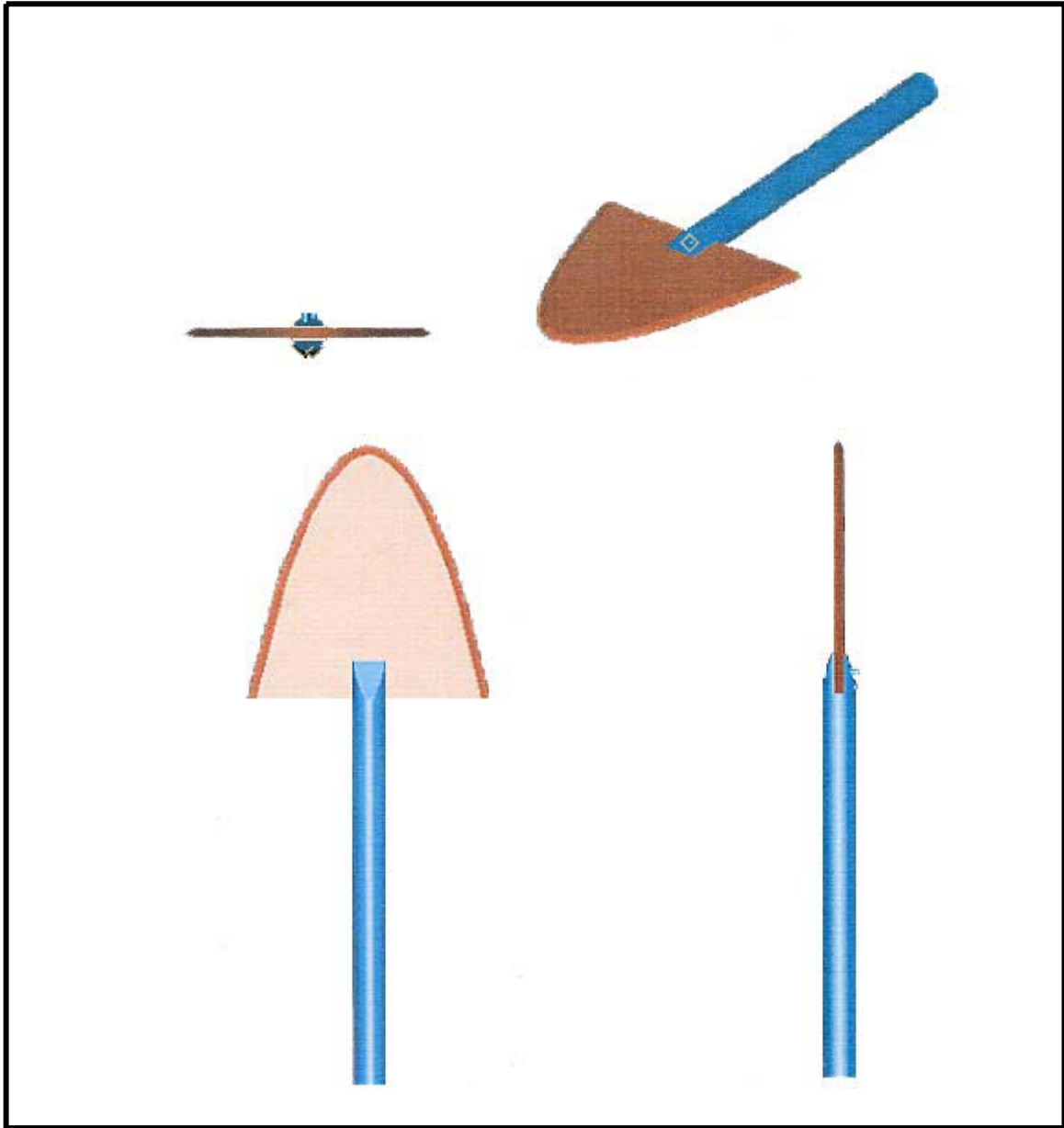
Figure 2.10.   Orthographic and isometric view of the 0° AOA sting and 45°-wedge leading edge planform model.

The Schlieren system is composed of a high-intensity (white) light source, two mirrors, focusing lens, knife-edge, screen, and camera, as shown in Figure 2.11. The light

source shines on the first mirror, which reflects a parallel beam through the test section. The second mirror, on the opposite side of the test section, directs the beam through a focusing lens. The image then travels through the focal point where the knife-edge is precisely located in order to eliminate rays that have been deflected by density gradients (while passing through the test section) resulting in variation of illumination indicating the locations of shocks, boundary layers, etc. The image becomes inverted after the focal point and is projected onto the viewing screen by the focusing lens. The image is recorded using a Polaroid camera or a Sony digital camera. The Polaroid camera is a two-part system consisting of the screen and film holder. The screen doubles as the camera housing and contains the controls for shutter speed and image capture. The film holder contains the film and aids in the development process by providing the internal mechanism that breaks and smoothly applies chemical developer onto the film. The digital camera is a Sony Mavica model MVC-FD91 with 1024x768 pixel resolution and internal 3-1/2 inch floppy disk storage. Figure 2.11 is a schematic of the NPS Schlieren system and Figure 2.12 shows the second mirror, knife-edge, focusing lens (hidden), and screen.

The shadowgraph system is identical to the Schlieren system except that the knife-edge is removed. The (inverted) image produced on the screen depicts areas of decreased illumination created from the scattering of light rays across a region where the density gradient is changing. The changes in the density gradient indicate the location of shocks and boundary layers by dark and bright lines or regions.
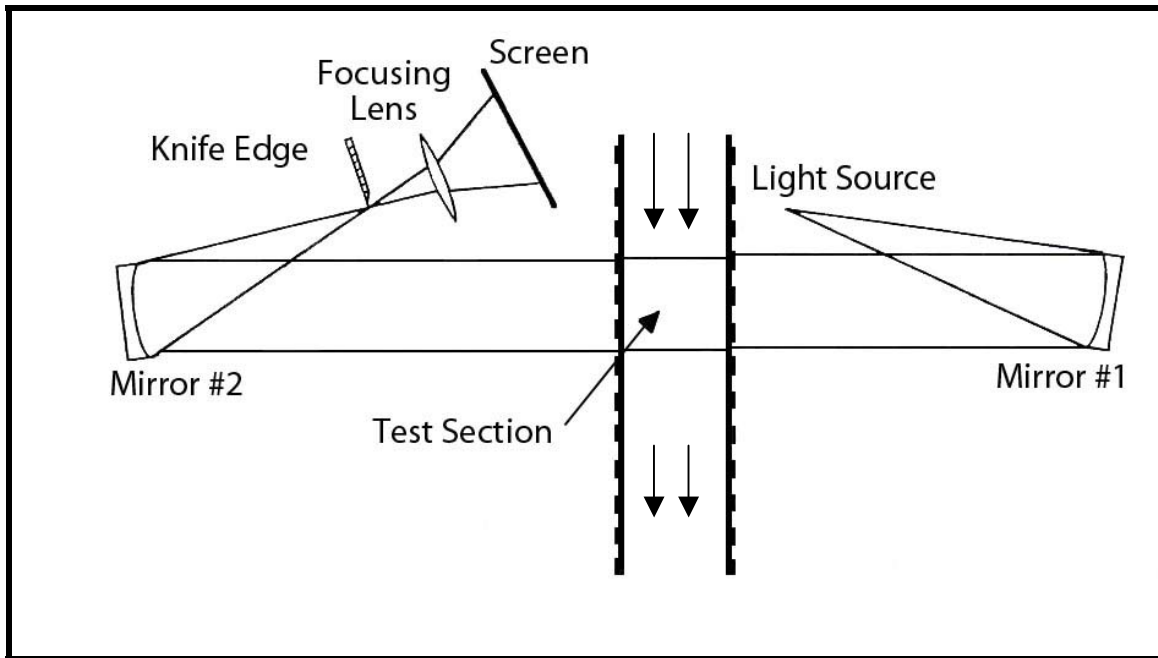
Figure 2.11.   NPS Schlieren system.
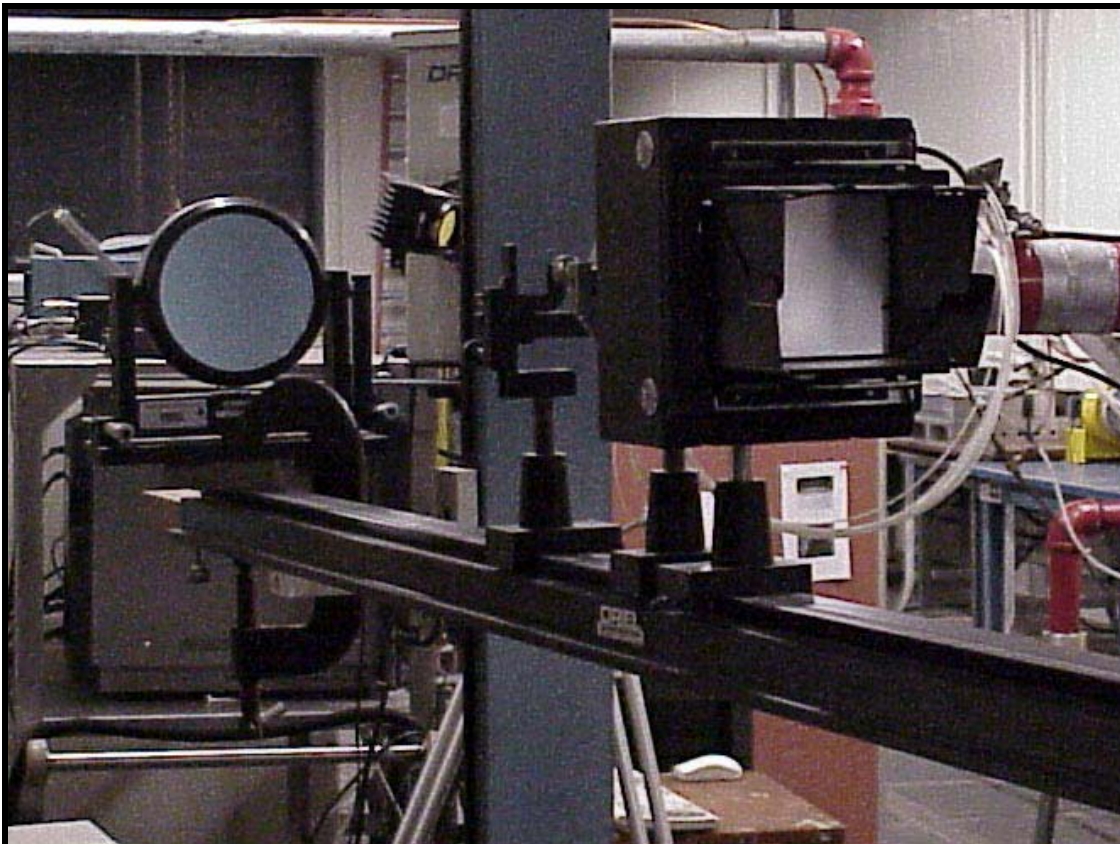
Figure 2.12.   Screen, focusing lens (hidden) and second mirror of the NPS Schlieren system.

3.   Pressure Sensitive Paint

Pressure sensitive paint (PSP) is an emerging technology that is reducing cost and time requirements to determine loads on models placed in wind tunnels.   Pressure sensitive paint, platinumoctaethylporphyrin (PtOEP), can be color calibrated to measure pressures using the Stern-Volmer equation listed below. The equation relates the ratio of the reference (no wind) image intensity (I_{ref}) to the test (wind on) image intensity (I) to the ratio of the test pressure (p) and the reference pressure (p_{ref}) [Ref. 20]. The constants A and B are found using pressure and temperature calibrations.

$$\frac{I_{ref}}{I} = A + B\,\frac{p}{p_{ref}}$$

Quantitative pressure measurements are possible using the pressure and temperature calibration, but they were not extracted due to the focus of this thesis on qualitative flow field characteristics.

A short study of quantum physics provides the knowledge required in order to understand how pressure sensitive paint works. Each atom or molecule has specific energy states with a common ground state. The molecules can be optically pumped (excited) into different energy states or levels creating an population inversion. A population inversion occurs when more electrons are pumped into the excited states than exist in the ground state. The electrons undergo various reactions when returning to the ground state, but pressure sensitive paint technology focuses on energy released in the form of photons. The energy of every photon is specifically defined by the molecule and the excited state from which it is transferred. The energy (E) released is related to the frequency (ν) of the light emission through the equation: $E = h\nu$. Where h is Planck's constant (6.63 x 10^{-34} Joule-sec). The process in which a molecule is optically pumped to achieve photon emission is defined as photoluminescence.   Efficient pumping is accomplished by illuminating a molecule with optical emissions having wavelengths that the molecule absorbs. In the case of PtOEP, absorption occurs in the in the ultraviolet range (uv) and in the visible green at wavelengths of 380 nm (+/- 10 nm) and 540 nm (+/- 10 nm), respectively. The photoluminescence is complete when the PtOEP emits light in

the visible red with a wavelength of 650 nm. Figure 2.13 illustrates the excitation and emission spectrum of PtOEP.
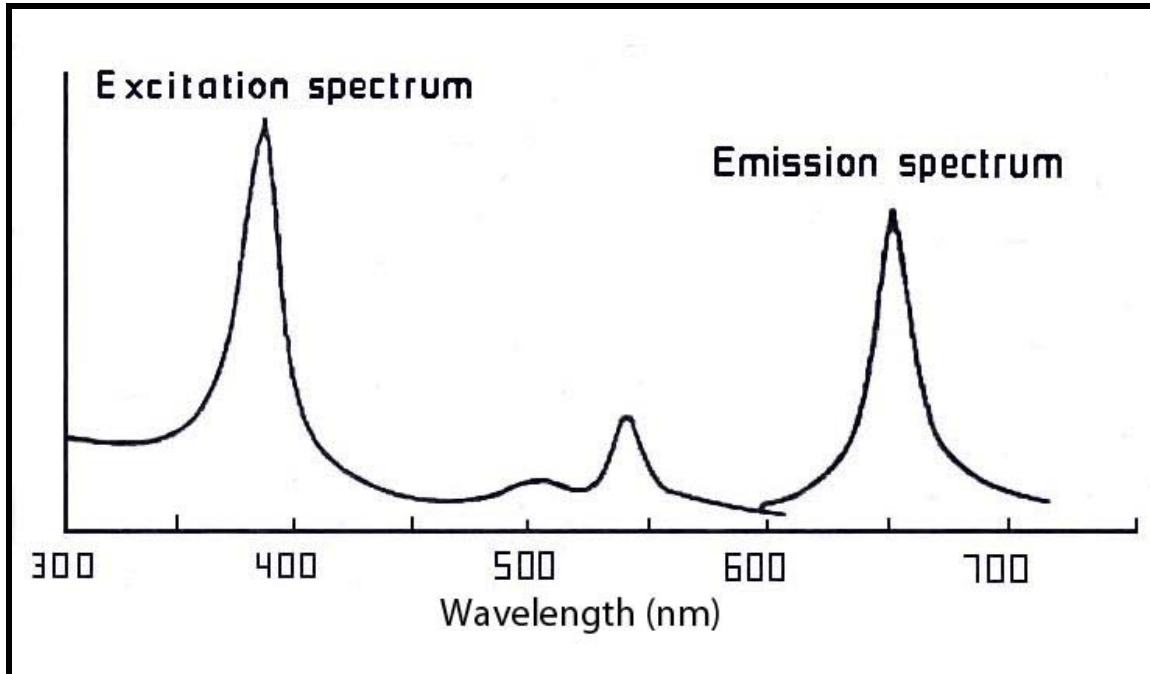
Figure 2.13. **Absorption and emission bands of platinumoctaethylporphyrin (PtOEP) copied from Ref. 21 Fig. 26.**

The relative pressure (or actual pressure if calibrated) is obtained through a process called oxygen quenching. When PtOEP is excited in the presence of oxygen, the oxygen interferes with the emission process, which causes less phosphorescence than would occur if no oxygen molecules present [Ref. 22]. Higher pressure areas will have less phosphorescence; enabling pressure differentials to be determined.

Prior to testing, the model was undercoated with Krylon glossy white paint for better reflectivity, and then coated with PSP using an airbrush. A new coat of PSP was applied prior to each new test Mach number. For each test series, the dry model was placed in the wind tunnel and illuminated using an Oriel Corporation 1-kW quartz tungsten halogen lamp (model 66200) with its associated lamp controller (model 6402). A blue gel filter (385 nm) was combined with a broadband dichroic mirror (Oriel model 6628) with a spectral range of 350-450 nm and a cut-off frequency of 550nm to filter the

uv radiation and to prevent infrared light from reflecting back to the source and overheating the system [Ref. 21]. The model intensity image was captured using a COHU (Model 4910) high performance, monochrome, low intensity CCD (charge-coupled display) camera with a 650 nm interference filter (70 nm bandwidth - Oriel Model 57610), mounted over its lens to block out undesired frequencies. The image was transferred from the camera to the Epix 4MEG Video Model 12 frame grabber board installed in the 386 computer via a R-59 coaxial cable. The data were processed and analyzed using the highest resolution setting (752 x 480) of the camera and EPIX image processing and analysis software. A Sony monitor connected to the computer was used to display the real-time image. See Figure 2.14 for a schematic of the PSP installation.

4.   Computer and Pressure System

The supersonic wind tunnel test section Mach number is determined by the design of the fixed nozzle blocks, but it is verified by pressure measurements. Pressure is measured in the plenum to obtain total or stagnation pressure (p_t) and the static pressure (p) is measured in the test section as shown in Figure 2.15. During continuous operations the nozzle operates efficiently with very minor total pressure losses (one percent or less) allowing the assumption of isentropic flow. The ratio of the total to static pressure (p_t/p) results in the determination of the test section Mach number by solving the isentropic pressure relationship where the Mach number is a function of the pressure ratio: $M = f(p_t/p)$ [Ref. 23]. The Mach number for the Mach 4 nozzle blocks was also determined using a pitot tube survey. The Mach number was determined from the relationship: $M = f(p_{t_2}/p_{t_1})$ where p_{t_2} is the pitot tube total pressure (behind the normal shock created by the pitot tube)and p_{t_1} is the plenum pressure.
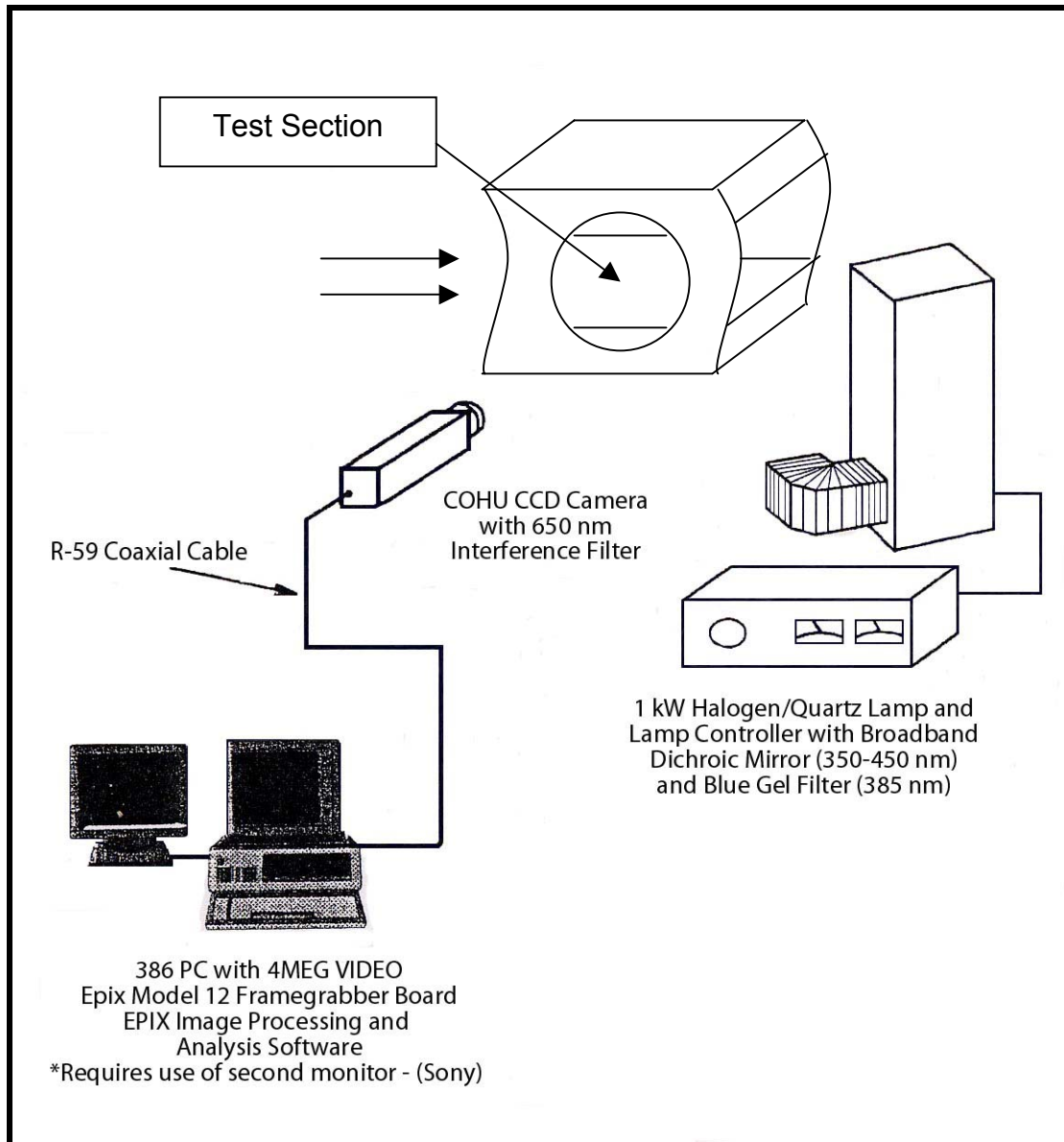
Figure 2.14.   Pressure sensitive paint system.

Prior to initiating test section Mach number pressure measurements, the Scanivalve Corporation (zero-operate-calibrate) ZOC-14 pressure transducer is calibrated using 110 psig Nitrogen gas, the HP 9000 controller, HP 6944A Multiprogrammer and the CALSYS2000.   Using the pneumatic control lines, the high pressure or second CALSYS2000 module initiates the calibration of the ZOC 14 over a range of positive (front-side) high, low and zero pressures followed by range of negative (back-side) high,

low and zero pressures. The CALSYS2000 is connected to the HP 9000 controller by a RS-232 link. Figure 2.15 is a diagram of the pressure measurement system.
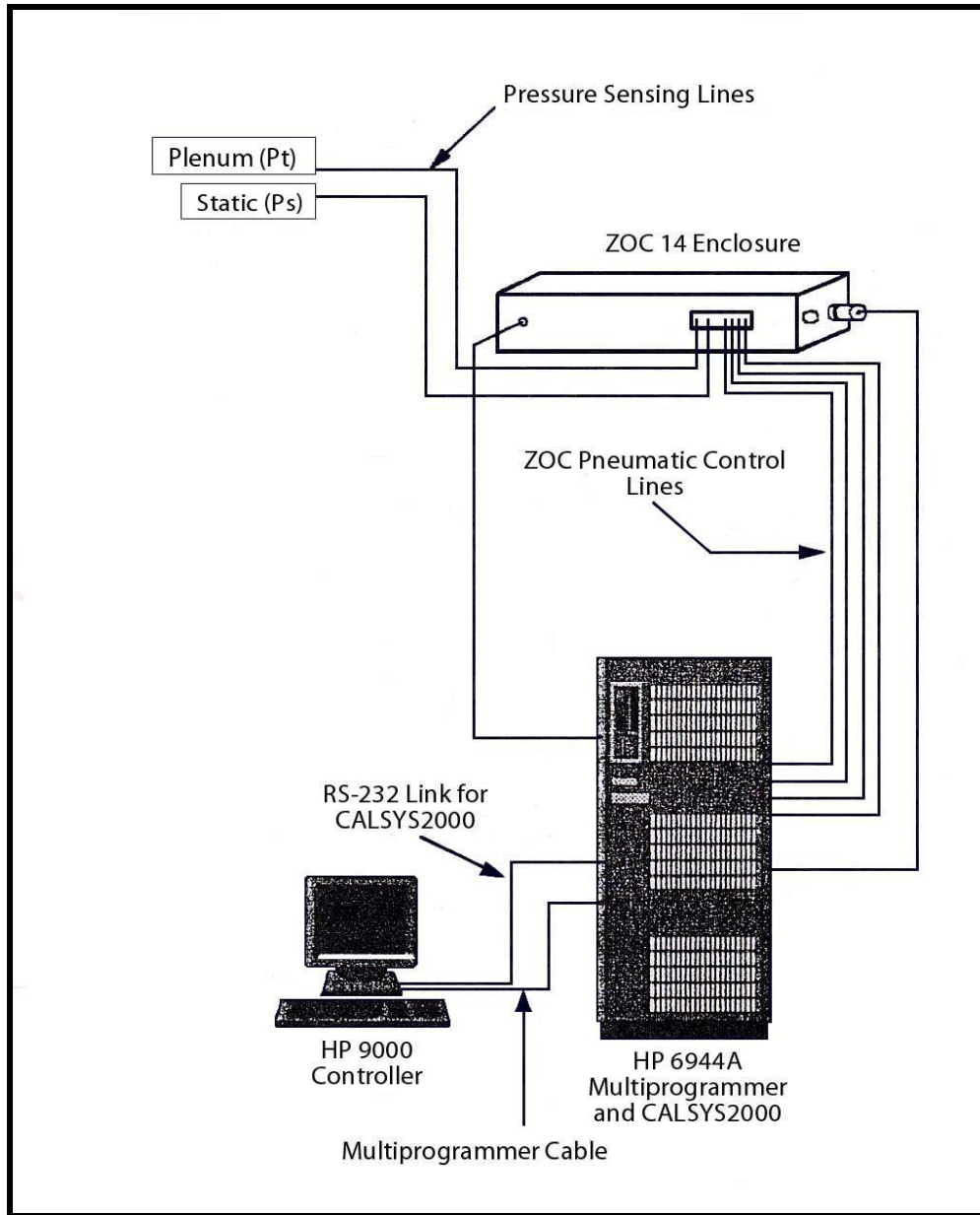
Figure 2.15. Pressure measurement system.

Test section Mach number pressure measurements are initiated manually at the HP 9000 controller. The signal from the computer to gather data is passed through the multiprogrammer to the ZOC-14 pressure transducer. The pressure transducer samples

the pressure data according to the frequency and duration prescribed in the HP 9000 controller and converts the pressures to electronic signals. The gage pressure (psig) data, from the plenum and test section, is routed from the pressure transducer to the multiprogrammer and transferred to the HP 9000 via the multiprogrammer cable where the data can be stored on the hard drive of the HP 9000 or printed using a dot matrix printer connected to the computer.

Pressure measurements were also taken using a manual back-up method in which Heise pressure gages are utilized. Plenum (total) pressure measurements are noted and recorded manually from the Heise pressure gauge used by the wind tunnel operator to monitor and set the plenum pressure using the Fisher pneumatic control valve. Test section (static) pressure is measured by a Heise pressure gage connected to a static port located in the exact same location but opposite side of the wind tunnel as the static pressure port used by the ZOC pressure system. Pressure readings were taken manually by the operator and recorded during steady state tunnel operations. (Note: The plenum pressure reading is measured in gage pressure, while the static pressure reading is measured in absolute pressure).

Temperature measurements were taken separately using a digital thermometer. The plenum pressure probe was replaced with a temperature probe for a determination of total or stagnation temperature (T_t) at each Mach number. Assuming isentropic nozzle flow, the ambient test section temperature (T) required to determine viscosity (μ) and Reynolds number is found by manipulating the stagnation temperature relationship:

$T_t = T\left[1 + \frac{(\gamma-1)}{2}M^2\right]$ [Ref. 23] where the M is Mach number and γ is the specific heat

ratio of air.

THIS PAGE INTENTIONALLY LEFT BLANK

III.   TEST RESULTS

A.   TEST SCHEDULE

All supersonic testing of the Price waverider planform, reported herein, was conducted in the NPS supersonic wind tunnel from June 26 to August 29, 2001. Testing began by using the Mach 1.7 nozzle blocks initially installed for use with AA 3802 laboratory classes. The Mach 2.8 nozzle blocks were utilized for the second round of tests followed, in turn, by the Mach 4 nozzle blocks.

The test schedule was determined by many factors. The factors included: air supply availability, nozzle block (Mach number) changes, tunnel modifications and model modifications. As mentioned in Chapter II, the supersonic tunnel air supply is shared between multiple testing apparatus. During the tests for this thesis, the air supply and technical support were shared with research conducted in the rotor spinpit. Additionally, each test Mach number for the supersonic wind tunnel is determined by a specific set of stainless steel nozzle blocks that form a two-dimensional convergent-divergent nozzle. The nozzle blocks are heavy and the process of changing nozzle blocks (Mach number) is arduous. Typically, testing was interrupted for at least two days when the nozzle blocks were changed, and required two or three people throughout the process. Due to the time consuming and difficult nature of nozzle block (Mach number) changes, testing for each Mach number was systematically completed before transitioning to another Mach number. Wind tunnel modifications (other than nozzle block changes) and sting modifications created a few minor delays, but modifying one of the models halted testing for three weeks.   The test results for the Mach 1.7 and 2.8 nozzle blocks can be found in Appendix A.

Testing utilizing the Mach 4 nozzle blocks began on August 17, 2001. Figure 3.1 shows the interior of the Mach 4 nozzle blocks during the installation process. The first test run was completed using a clean wind tunnel in order to check the integrity of the O-ring seals, windows, mounting plugs and nozzle blocks, as well as to determine the plenum pressure setting required for tunnel start and the test section Mach number. The

Mach number was not able to be determined due to erroneous pressure readings from the pressure measurement system. The plenum pressures exceeded both the ZOC and calibration (CALSYS2000) capabilities. Once the initial integrity checks were completed, the 0° AOA sting and 45°-wedge leading edge model were mounted horizontally in the wind tunnel and testing was initiated. The tunnel started, shadowgraph images of the shock pattern were recorded, and pressure measurements were taken using the back-up (Heise gage) system. The final test of the day was conducted using the horizontally mounted 45°-wedge leading edge model and 2° AOA sting. Shadowgraph images were taken and manual pressure measurements recorded.
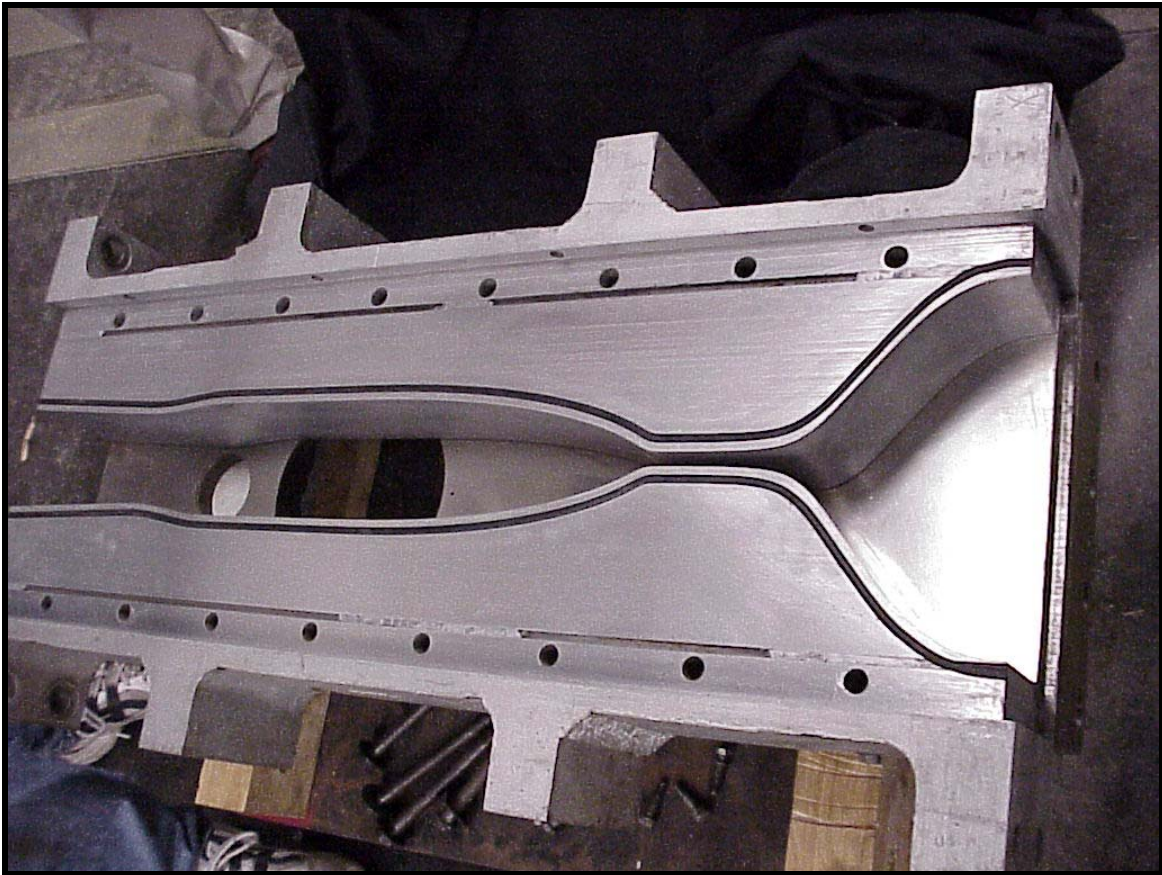
Figure 3.1.   Interior view of the Mach 4 nozzle block design.

Mach 4 testing with the 45°-wedge leading edge model resumed on August 21st. Previous tests at 0° and 2° AOA were duplicated to ensure repeatability. The 45°-wedge

leading edge model was tested horizontally at 0°, 2°, 4° AOA and vertically at 0° and 2° AOA. No change was noticed in the vertical model shock patterns between 0° and 2° AOA so the 45°-wedge leading edge model was not tested vertically at 4°.

On August 22nd the 15°-wedge leading edge model became available for testing. Before testing began the following day, a 0° AOA shadowgraph reference image of the 15°-wedge leading edge model was taken. Tests, utilizing the 15°-wedge leading edge model, consisted of a full AOA range of horizontal tests and a modified AOA range of vertical tests.

Mach 4 testing utilizing pressure sensitive paint began on August 27, 2001. The 45°-wedge leading edge model and 0° AOA sting were inserted into the test section of the supersonic wind tunnel. A wind-off image was recorded followed by a wind-on image of the 45°-wedge leading edge model. Using the computer, the intensity of the wind-off image was compared to the intensity of the wind-on image resulting in the intensity ratio that provided the qualitative data pertaining to relative pressures located on the model. The entire process is called "ratioing" for short. The final test of the day was completed using the 45°-wedge leading edge model and the 4° AOA sting. The wind-off and wind-on images were recorded and ratioed. After the model was removed from the supersonic wind tunnel, it was observed that the pressure sensitive paint on the leading edge had been worn away from tiny particles in the supersonic flow. The discovery resulted in the conclusion that wind-off images should be taken after the wind-on images to provide better ratioing by removing the inconsistencies caused by pressure sensitive paint loss.

The 15°-wedge leading edge model was taken through the full range of AOA (0°, 2°, and 4°) testing the following morning. In addition to testing the 15°-wedge leading edge model, the 45°-wedge leading edge model was tested at 2° AOA, completing the AOA sweep for the 45°-wedge leading edge model. Mach 4 testing was concluded and repeatability was assured by duplicating the test for the 15°-wedge leading edge model at 0° AOA on Wednesday, August 29, 2001.

B.   DATA REDUCTION

1.   Shadowgraph

Shadowgraph images were used to record test results because they provided an adequate representation of shock and boundary layers formations in the test section without having to spend the extra time to precisely position the knife-edge at the focal point for the Schlieren images.   The first two test images, taken during Mach 1.7 testing, were captured using a Polaroid camera, but the antiquated film development process proved unreliable.   The remaining images were captured using a Sony Mavica digital camera.   The change in cameras resulted in a slight loss of detail and contrast in the shadowgraph images, but the speed, reliability and ease of operation made the digital camera a much better image recording device.

The initial Mach 4 tests attempted to utilize the shadowgraph image of the test section projected on the screen to determine shock passage and tunnel start.   However, the starting shock was too fast and weak to be viewed.   The best indication of shock passage and tunnel start was the sharp drop in test section static pressure.   Subsequent tests using both the 45°-wedge leading edge and 15°-wedge leading edge models provided excellent shadowgraph images of shock and boundary layer location.   In addition to shock location, the horizontally-mounted 0° AOA shadowgraph images of both models were utilized as an additional method of determining free-stream Mach number.

The 45°-wedge leading edge model horizontal (side view) shadowgraph images at 0°, 2° and 4° AOA are shown in Figures 3.2, 3.4, and 3.6. The 45°-wedge leading edge model has a detached normal shock that was visually observed in the test section and is noticeable on the 45°-wedge leading edge model images by the rounded appearance of the shock and a disperse shadow region followed by a small bright area just forward of the nose of the model.

The 15°-wedge leading edge model horizontal shadowgraph images at 0°, 2° and 4° AOA are shown in Figures 3.3, 3.5, and 3.7. The 15°-wedge leading edge model has

an attached oblique shock that is readily apparent from the side-view shadowgraph images. Additionally, an intense white region just above the upper surface of the sharp edge (wedge) on all 15°-wedge leading edge model images is indicative of Prandtl-Meyer expansion waves as shown in a close-up image, Figure 3.8, at 0° AOA.
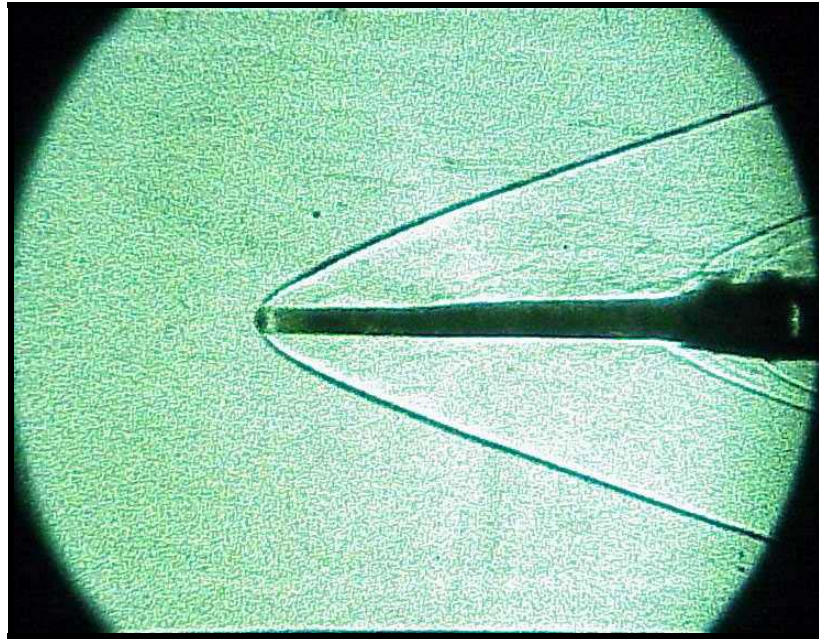
Figure 3.2.   **Mach 4 shadowgraph image of the 45°-wedge leading edge model at 0° AOA.**
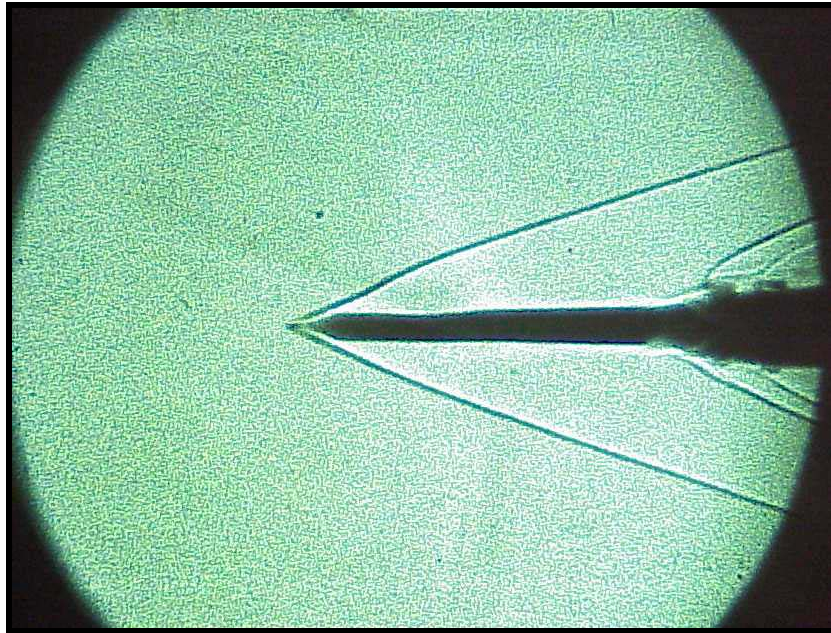
Figure 3.3.   **Mach 4 shadowgraph image of the 15°-wedge leading edge model at 0° AOA.**
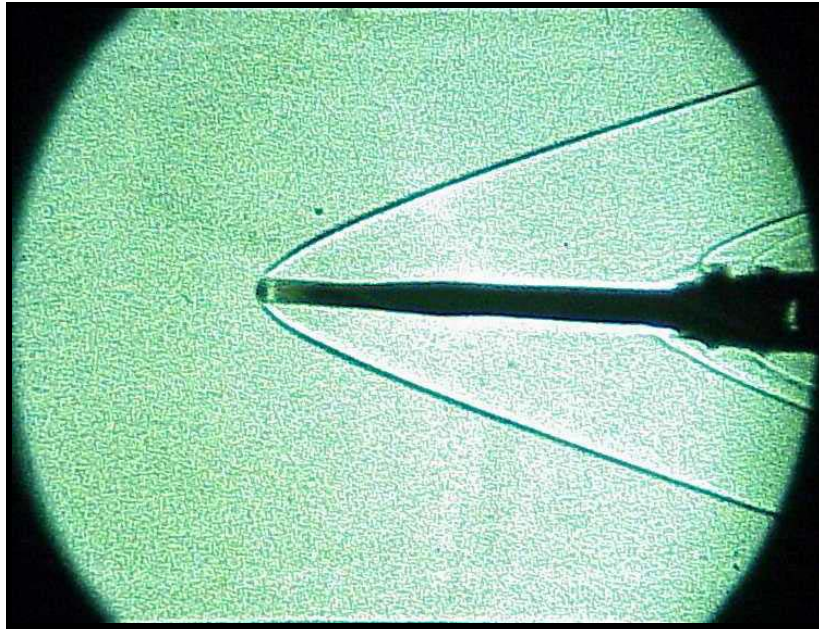
Figure 3.4. Mach 4 shadowgraph image of the 45°-wedge leading edge model at 2° AOA.
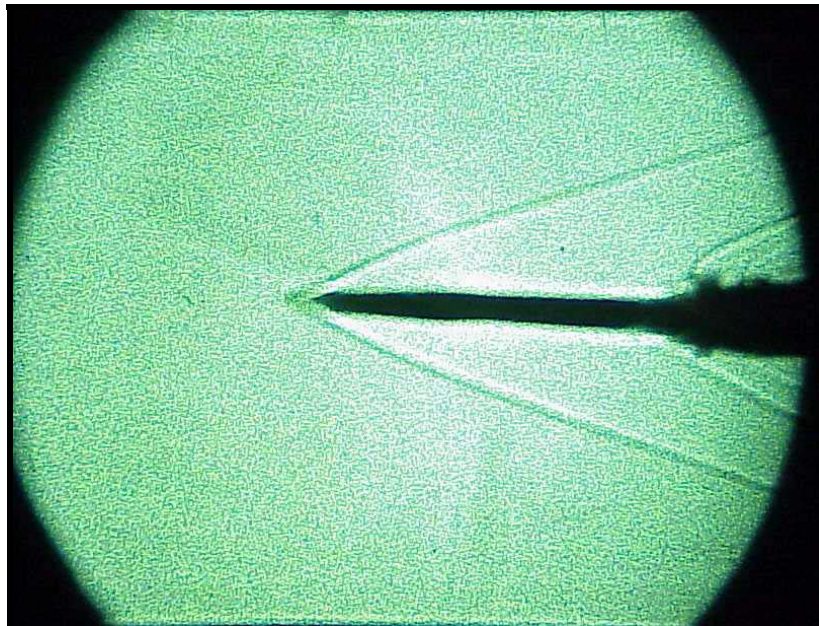
Figure 3.5. Mach 4 shadowgraph image of the 15°-wedge leading edge model at 2° AOA.
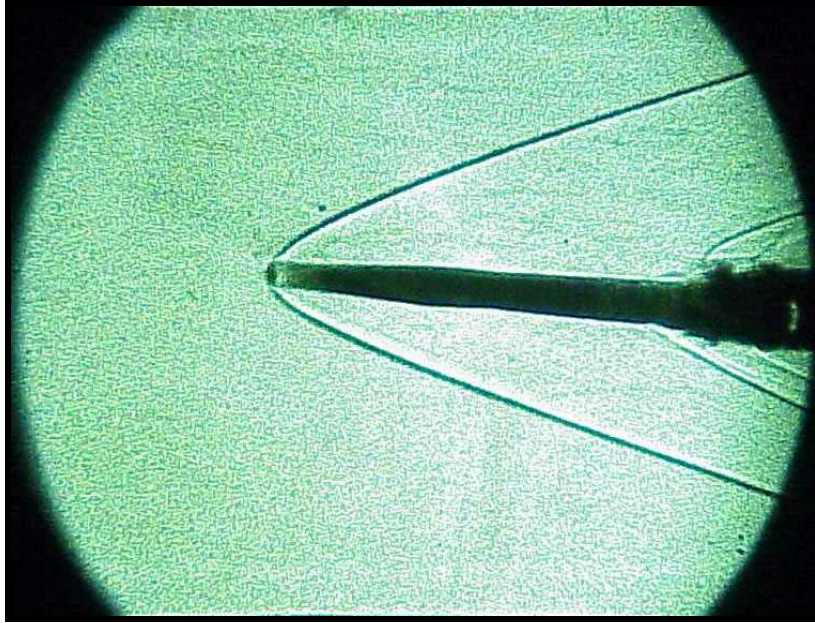
Figure 3.6. Mach 4 shadowgraph image of the 45°-wedge leading edge model at 4° AOA.
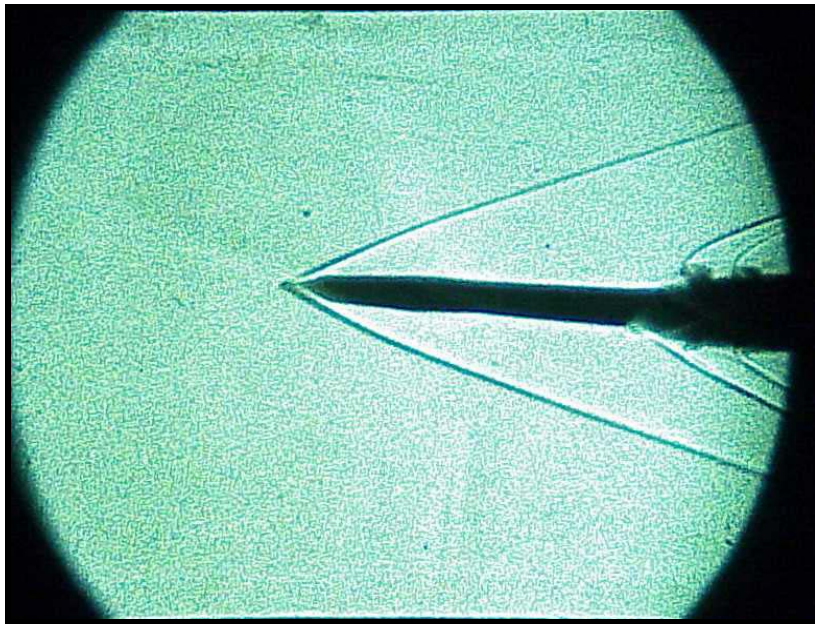
Figure 3.7. Mach 4 shadowgraph image of the 15°-wedge leading edge model at 4° AOA.
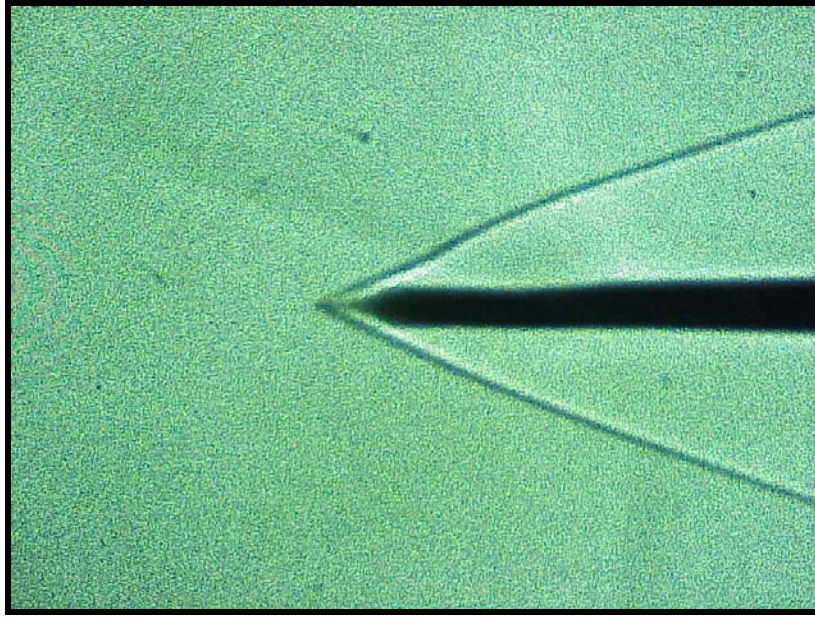
Figure 3.8.   Mach 4 shadowgraph close-up of the 15°-wedge leading edge model at 0° AOA.

The 45°-wedge leading edge model vertical (top view) shadowgraph images at 0° and 2° AOA are shown in Figures 3.9 and 3.10. The 15°-wedge leading edge model vertical shadowgraph images at 2° and 4° AOA are shown in Figures 3.11 and 3.12. Shadowgraph images were not taken for the 45°-wedge leading edge model at 4° or 15°-wedge leading edge model at 0° AOA because there was no noticeable change between the different angles of each model. The detached normal shock, shown in Figures 3.9 and 3.10, can be observed tracing the outline of the 45°-wedge leading edge model and slowly diverging outward. A shadow region is observed between the nose of the 45°-wedge leading edge model and apex of the Mach cone. The shock on the 15°-wedge leading edge model, shown in Figures 3.11 and 3.12, is initially attached to the model planform but can be seen slightly diverging away about halfway down the length of the model.
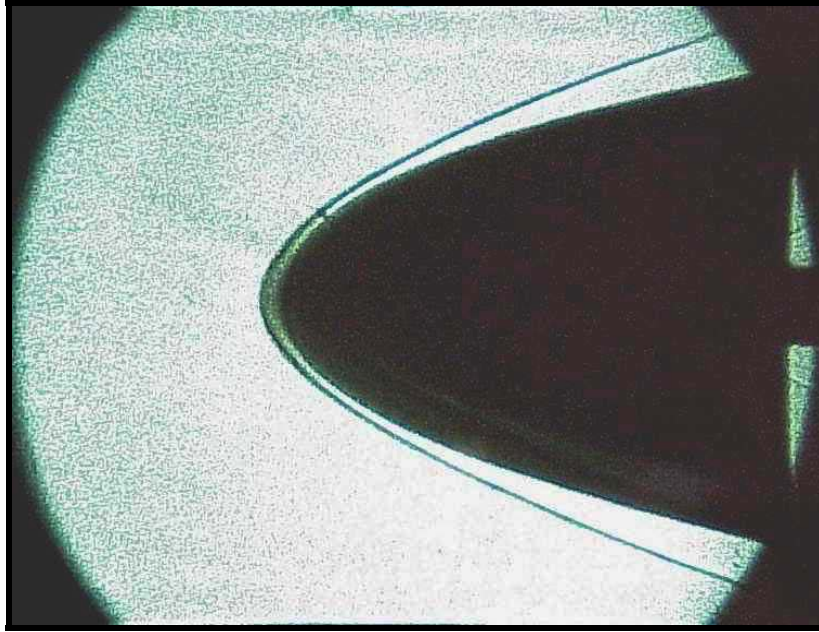
Figure 3.9.   Mach 4 shadowgraph image of the vertically mounted 45°-wedge leading edge model at 0° AOA.
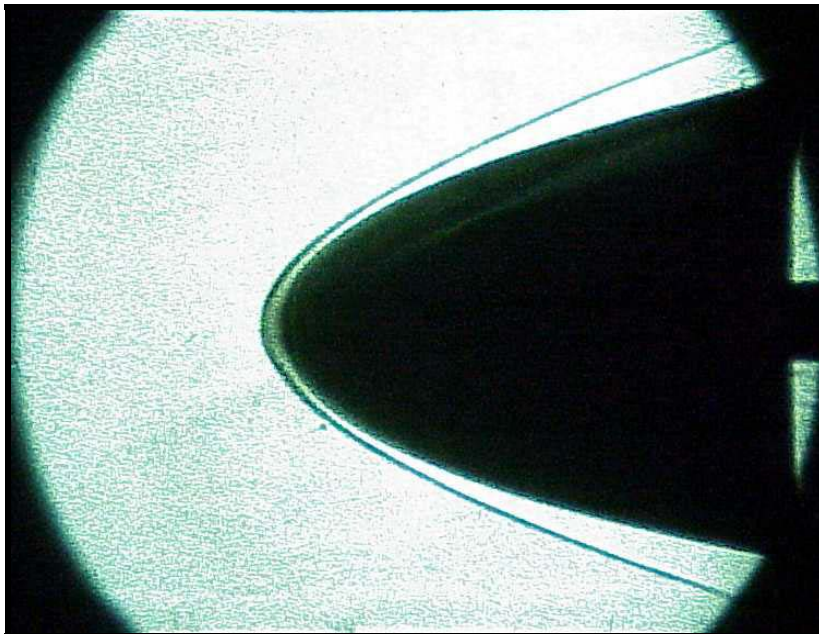
Figure 3.10.   Mach 4 shadowgraph image of the vertically mounted 45°-wedge leading edge model at 2° AOA.
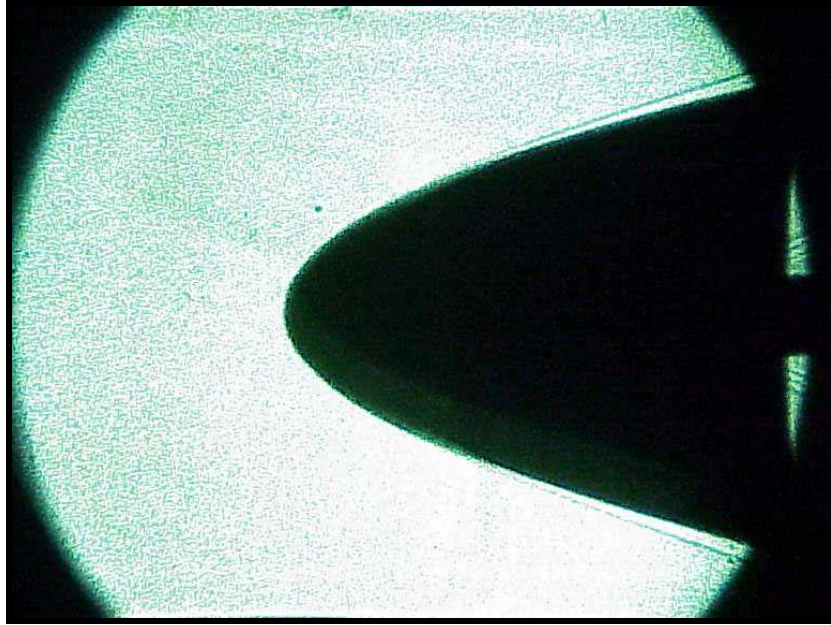
Figure 3.11.   Mach 4 shadowgraph image of the vertically mounted 15°-wedge leading edge model at 2° AOA.
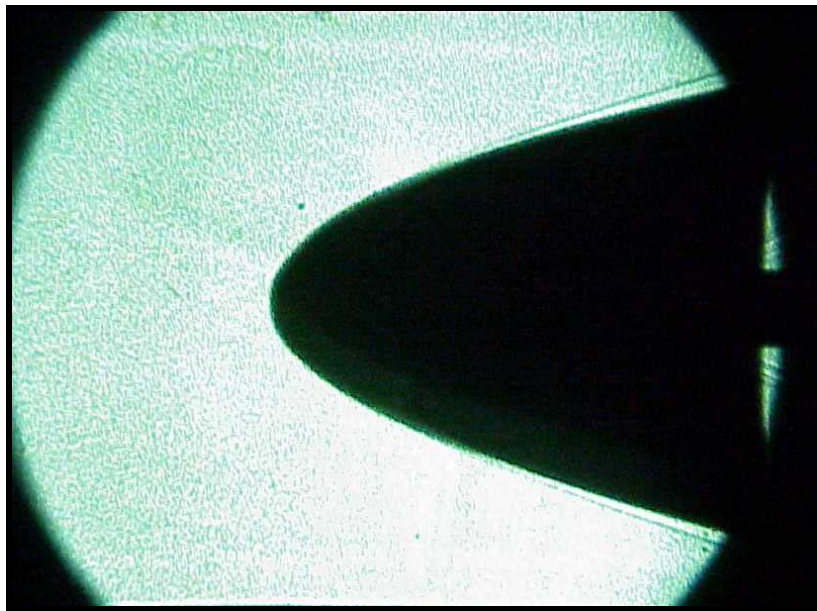
Figure 3.12.   Mach 4 shadowgraph image of the vertically mounted 15°-wedge leading edge model at 4° AOA.

## 2.	Pressure Sensitive Paint

Pressure sensitive paint flow field data were only available at Mach 4 because supersonic flow could not be established at lower Mach numbers. Wind-on and wind-off images were taken and ratioed for both the 45°-wedge leading edge and 15°-wedge leading edge models mounted vertically (top view) at 0°, 2°, and 4° AOA.

The pressure sensitive paint worked very well throughout the entire test process, although minor problems were encountered. The leading edges of both the 45°-wedge leading edge and 15°-wedge leading edge models suffered paint loss from being virtually sandblasted from the unclean test section airflow. The nose of each planform suffered the greatest paint loss while the edges near the aft end retained all paint. Additionally, random paint contamination occurred resulting in minor spots on both models and one large blot on the 15°-wedge leading edge model. The minor paint contamination was caused by a greasy substance present in the wind tunnel airflow obstructed the oxygen quenching capability of the paint.

The minor paint contamination and the leading edge pain loss did not disrupt the flow field measurements or create any uncertainty about the results. However, in order to ensure better results the image capture sequence was reversed. The change in sequence resulted in the wind-off image being captured last. Allowing the paint loss and contamination to be eliminated when the two images are ratioed by the computer. The 0° AOA colored pressure sensitive paint images for the 45°-wedge leading edge and 15°-wedge leading edge models are shown in Figures 3.13 and 3.14, respectively.

Higher surface pressures are red, lower pressures are represented by blue and intermediate pressures are represented by yellow and pink. Spanwise irregularities, detected by the pressure sensitive paint as alternating blue and pink lines, are found on both models, but are more prevalent on the 45°-wedge leading edge model.   In addition to the spanwise irregularities, the curved normal shock created by the presence of the sting is observed on all the pressure sensitive paint images at the base of the models. Lower pressure regions (light blue) are also found near the base of all models between

45

the normal shock and the outer edge of the planform. The region size and shape depends on the model and AOA.

Both models indicate a relatively constant pressure over the surface of the planform except near the trailing edges where there appears to be pressure activity not associated with the spanwise irregularities. Figures 3.15 and 3.16 are pressure sensitive paint images of the 45°-wedge leading edge and 15°-wedge leading edge model at 2° AOA. The pressure sensitive images of the 4° AOA 45°-wedge leading edge and 15°-wedge leading edge models are shown in Figures 3.17 and 3.18, respectively. Both images of the 4° AOA models show areas of constant pressure on the upper surface, reduced sensitivity to the spanwise irregularities, and indicate high-pressure regions (red) behind shock locations. Additionally, asymmetry caused from misalignment of the sting and sting mount is noticeable on the 4° AOA images.
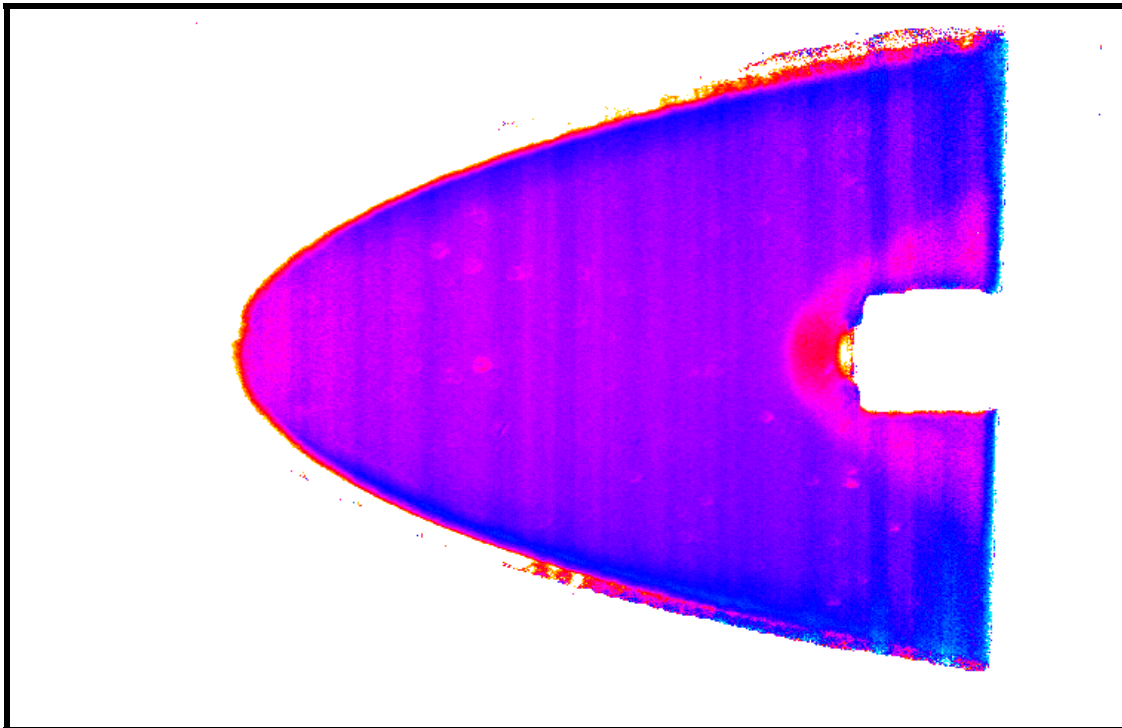
Figure 3.13.   Mach 4 pressure sensitive paint image of the 45°-wedge leading edge model at 0° AOA.
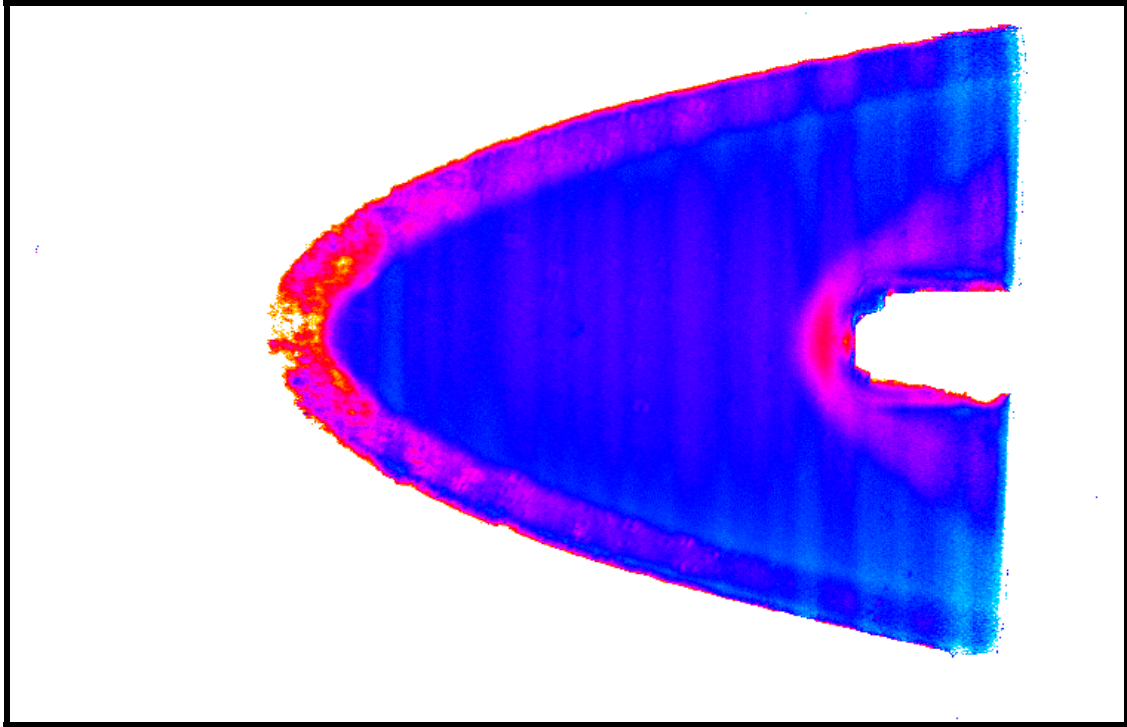
Figure 3.14. Mach 4 pressure sensitive paint image of the 15°-wedge leading edge model at 0° AOA.
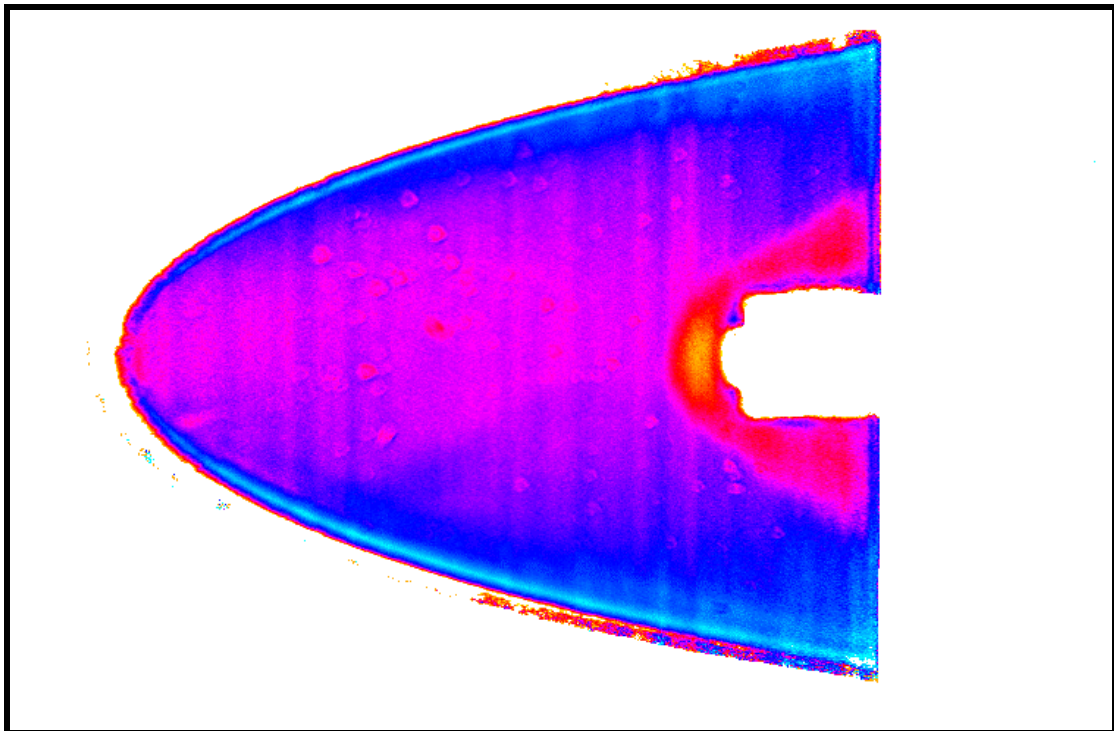
Figure 3.15. Mach 4 pressure sensitive paint image of the 45°-wedge leading edge model at 2° AOA.
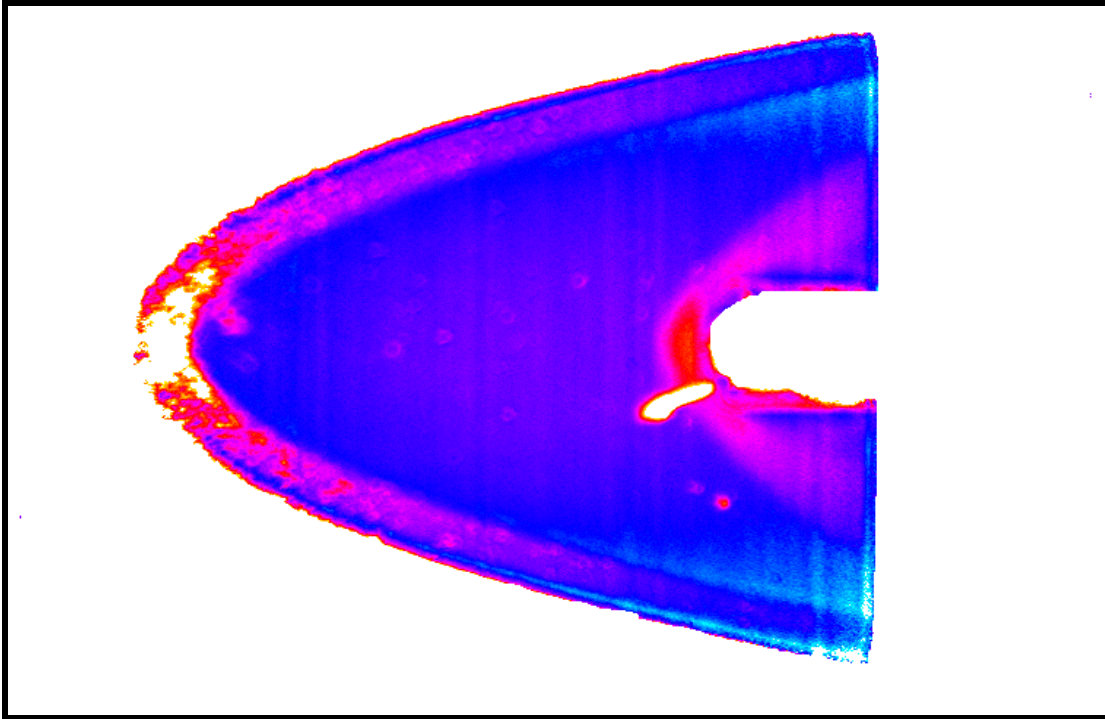
Figure 3.16.   Mach 4 pressure sensitive paint image of the 15°-wedge leading edge model at 2° AOA .
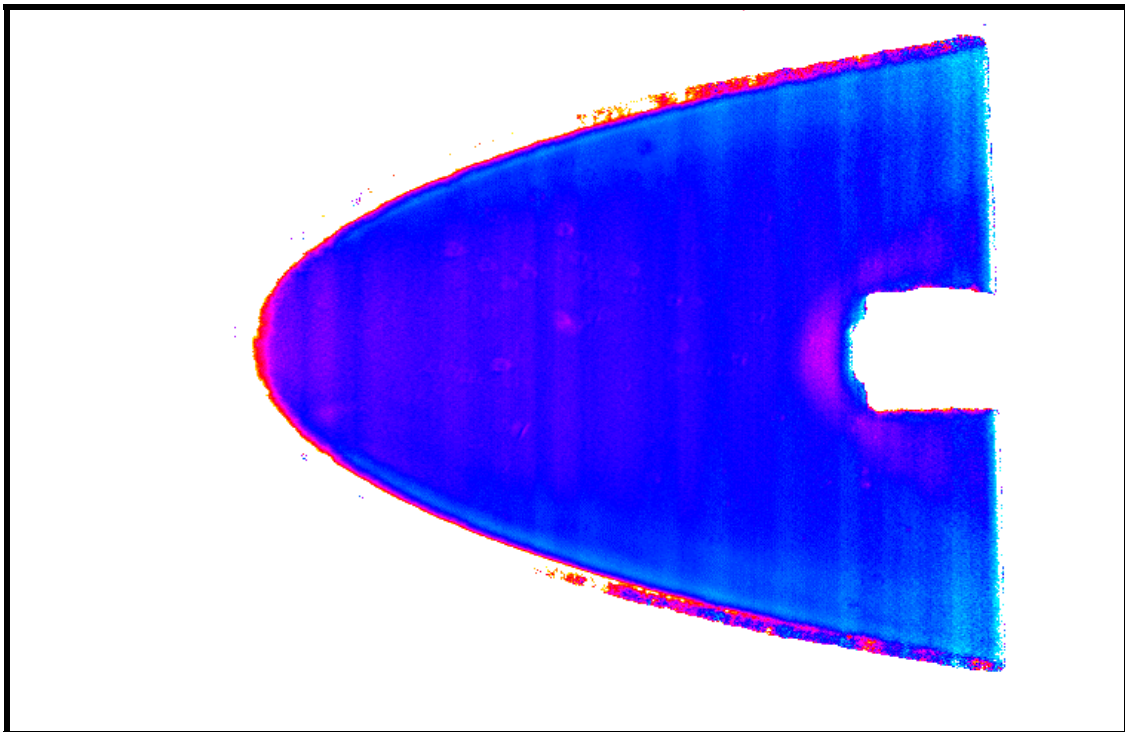
Figure 3.17.   Mach 4 pressure sensitive paint image of the 45°-wedge leading edge model at 4° AOA.
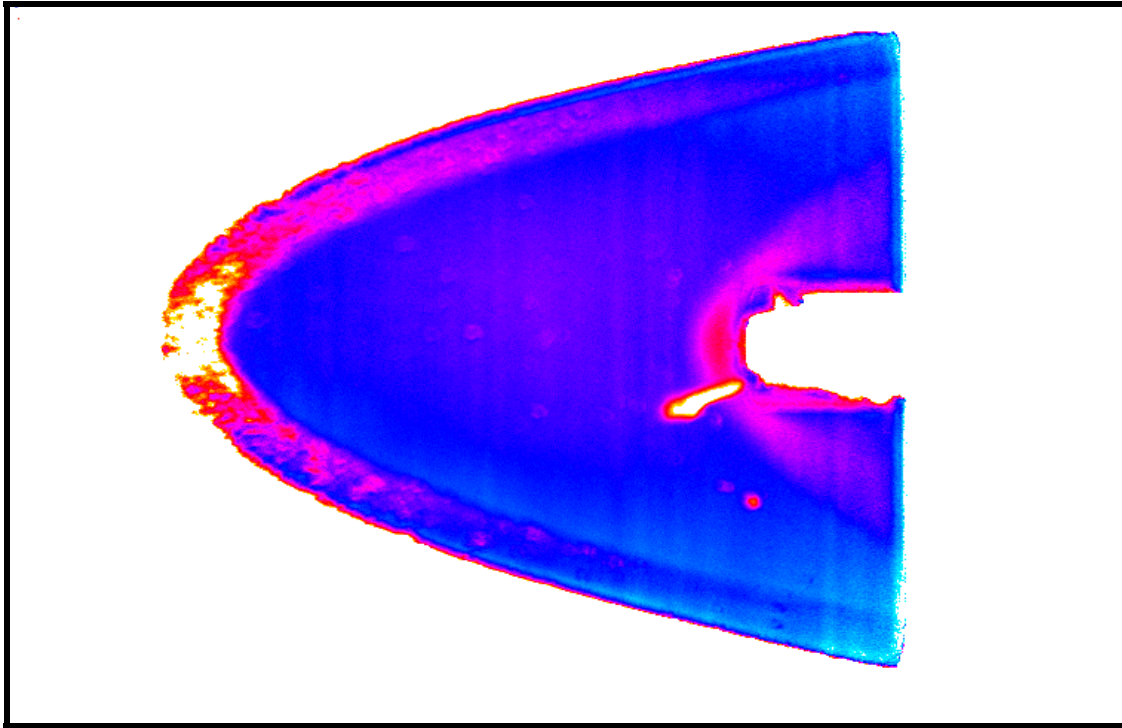
Figure 3.18.   Mach 4 pressure sensitive paint image of the 15°-wedge leading edge model at 4° AOA.

3.   Test Section Pressure Measurements

The initial calibration run utilizing the Mach 4 blocks provided no indication of the test section Mach number because the ZOC pressure system capabilities were exceeded.   As a result of the loss of the ZOC pressure measurement system, the standby Heise pressure system was utilized during Mach 4 testing. Test section Mach surveys were conducted between tests using an empty wind tunnel.   A pitot tube was manufactured from materials on hand and inserted into the test section for the Mach surveys.

Calculations using the isentropic tables and the manual plenum and test section static pressure measurements taken during the shadowgraph and pressure sensitive paint tests indicated that the average Mach number was 3.961 with a standard deviation of 0.087. The Mach number varied from 4.106 to 3.881. The wide range of Mach numbers

49

is due to reading errors associated with the Heise gage. The test section static pressure proved to be the critical value for determining Mach number. A small variation in the static pressure (± 0.25 psi) had a greater affect on the Mach number calculation than a 5-psi difference in plenum pressure. Unfortunately, the Heise gage could only be read to the nearest 0.25 psia resulting in a wide variation of Mach numbers (4.106 to 3.881). All pressure measurement results using the Heise gages are presented in Table B.2 of Appendix B.

The test section total pressure survey was conducted using a pitot tube connected to a Heise gage. The pitot tube provided total pressure measurements (p_{t_2}) after the normal shock. The Mach number was determined using the total pressure ratio $\left(p_{t_2}/p_{t_1}\right)$ in the normal shock tables [Ref. 23 pages 393-401], where p_{t_1} is the plenum pressure.

The survey included two centerline, two lateral and two longitudinal measurements. The centerline surveys were located at the dead center of the test section cross sectional area: 2 inches from both the top and bottom and 2 inches from either sidewall. The lateral surveys, conducted along the vertical centerline, were performed an inch to the left of horizontal centerline (negative) and an inch to the right (positive) where left and right are determined by facing the incoming test section flow. The longitudinal surveys, conducted along the horizontal centerline, were performed an inch up (positive) and 1/2 inch down (negative) from vertical centerline resulting in a +9° pitch and -4.5° of pitch respectfully. The pitot tube pressure readings indicate that the Mach number varies across the wind tunnel from 4.01 $\pm$ 0.02 near the walls to 4.088 $\pm$0.053 at the center of the test section. Table B.3 in Appendix B contains the data obtained during the Mach 4 pitot tube survey.

Plenum temperature readings taken were very consistent at 57° F. Reynolds number calculations resulted in a value of: Re/ft = 1.976 x 10^7. The Reynolds number calculation was made using the ideal gas law, p = ρRT with the measured test section static pressure and isentropic calculation of static temperature from the total temperature measured in the plenum. The viscosity (μ) was calculated using equation 2.91a in Roskam [Ref. 27] and the static test section temperature.

IV.   DISCUSSION

A.   SHADOWGRAPH

Mach 4 tests of the Price waverider planform provided excellent shadowgraph images depicting the normal (45°-wedge leading edge model) and oblique shock (15°-wedge leading edge model) locations around the model. The 0° AOA shadowgraph images of both the 15°-wedge leading edge and 45°-wedge leading edge models, Figures 3.2 and 3.3, provided information about the test section Mach number. The detached shock of the 45°-wedge leading edge model enables Mach wave theory to be assumed. The theory states that the Mach wave has an associated angle (2μ) between the upper and lower shocks or Mach cone.   The Mach angle (μ) is the half angle of the Mach cone and can be used to determine the Mach number by a simple relation ship: $M = \dfrac{1}{\sin \mu}$ [Ref. 23 page 92]. The 45°-wedge leading edge model at 0° AOA, Figure 3.2, indicates a cone angle (2μ) of 39° with an associated Mach number of 3. The method and concept are true, but the result is limited by the fact that the Mach wave is still bending so the actual Mach wave angle cannot be precisely determined.

The attached shock of the 15°-wedge leading edge model is indicative of an oblique shock. The Mach number is determined from measuring the oblique shock angle (θ) of either the upper or lower shock and using the Oblique shock chart [Ref. 23 page 379] with the deflection angle (δ) of 15°. The measured shock angle was 25° with the resulting freestream Mach number of just over 4. In addition to serving as an additional method of determining test section Mach number, the shadowgraph images of the 15°-wedge leading edge model can be used to illustrate the location of Prandtl-Meyer expansion waves. Using the close-up picture of the 15°-wedge leading edge model, Figure 3.8, the region of white above and below the sharp leading edge is indicative of Prandtl-Meyer expansion waves.

At Mach 4 there was no measurable difference in shock location for differing pitch angles with the vertically mounted models, but there was tremendous difference in shock patterns between the 45°-wedge leading edge and 15°-wedge leading edge models. The 45°-wedge leading edge model image, Figure 3.9 clearly shows a detached shock that remains fairly close to the model planform. The 45°-wedge leading edge model also shows a shadow region around the nose of the model, indicating a subsonic flow that is re-accelerating over the model top of the model and around the nose. Figure 4.1 is a graphical description of the flow region around a blunt edge object and the phenomenon captured by the 45°-wedge leading edge model shadowgraph images, Figure 3.2 and 3.9 [Ref. 23]. The shadowgraph image of the vertically mounted 15°-wedge leading edge model reveals an attached shock around the nose of the model that becomes detached as it moves aft along the leading edge of the model.
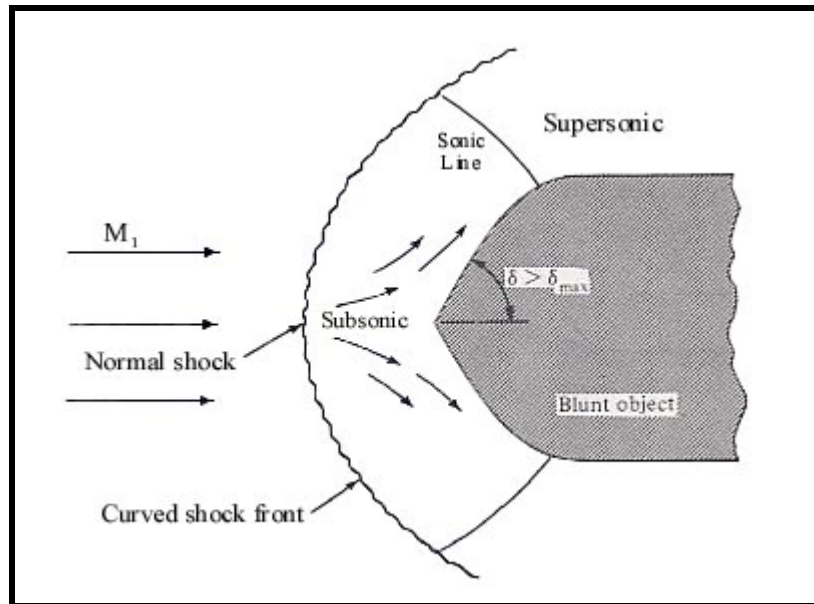
Figure 4.1.   Detached shock created by a blunt object ($\delta > \delta_{max}$) copied from Ref. 23 Fig. 7.13.

B. PRESSURE SENSITIVE PAINT

Significant differences were noted between the 15°-wedge leading edge and 45°-wedge leading edge models, but both models were similarly affected by spanwise irregularities and the rounded normal shock from the sting. The spanwise irregularities are caused from the imperfect machining of the models. The extremely small ridges and valleys across the model chord create differing pressures that are picked up by the pressure sensitive paint. The degree in which the surface pressure is influenced by the imperfect machining is also a function of pitch angle or AOA. This can be shown by comparing the 0° AOA (Figure 3.13) and 2° AOA (Figure 3.15) images of the 45°-wedge leading edge model. The machining imperfections had less of an influence on surface pressure when the pitch angle was increased.

The 45°-wedge leading edge model appears to have differing color regions even if the spanwise imperfections are ignored. A (blue) lower pressure region starts out small just aft of the nose along the edge of the flat planform. The region appears to grow and fan out as it travels the length of the 45°-wedge leading edge model. A low-pressure region that grows larger as it traverses down the length of the model would indicate separation or vortical flow. The presence of separation or vorticities would indicate that the 45°-wedge leading edge planform model was operating in region B of Squire's delta wing theory (Figure 1.5). The vorticies follow the shape of the planform instead of flowing parallel to the chord which is demonstrated in Johnson's hydrodynamic flowfield studies [Ref. 2]. The vorticies are believed to be the result of the planform shape interacting with the upper surface flow and not the result of flow interaction between the upper and lower surface.

The predominant singular color found on the upper surface of the 15°-wedge leading edge model is indicative of uniform pressure and two-dimensional flow. However, there appears to be low pressure areas near the trailing edges of the planform that are similar but much smaller than those previously mentioned on the 45°-wedge leading edge model. The pressure sensitive paint evidence does not support the same conclusion as the 45°-wedge leading edge model of vortical flow. The low pressure areas

appear to be a result of the reduced pressure loss across the oblique shock as the shock curves around the waverider planform. The 15°-wedge leading edge model is believed to be operating in region C of Squire's delta wing flow theory in which the upper surface has a constant pressure. In addition to the pressure results on the flat planform surface, the isentropic acceleration associated with Prandtl-Meyer is evident by the quick transition from red to pink to blue on the edges of the 15°-wedge leading edge model.

Separation between upper and lower surface flows was expected for the 15°-wedge leading edge model since the shock wave is attached along most of the model and remains close except at the aft end of the model. The detached shock of the 45°-wedge leading edge model, observed in the shadowgraph images, is apparently close enough that the upper and lower surfaces flows remain separated because the higher pressure flow from the lower surface reaches the speed of sound before arriving at the upper surface, resulting in distinct pressure and flow regions for the upper and lower surfaces. It is interesting to note the rapid deceleration, increasing pressure and oxygen quenching resulting in a dark red region behind the normal shock created by the influence of the sting. The pressure recovery region appears to be greater on the 15°-wedge leading edge model than on the 45°-wedge leading edge model which would be a further indication of faster flow (larger Mach number) over the upper surface of the 15°-wedge leading edge model.

C. PRESSURE MEASUREMENTS

The plenum pressure required to operate the Mach 4 nozzle blocks was too high to use the ZOC system. The Heise gage system was utilized during Mach 4 testing and yielded pressure readings and associated Mach number calculations that were very close to the design of the nozzle blocks. Table B.2 lists the data gathered during all test runs using the Heise gages and indicates that the average freestream Mach number was 3.961. The highly accurate pitot tube survey indicated an average freestream Mach number of 4.088 in the center of the test section. The pitot tube survey results confirm the validity

of the Heise gage measurements and demonstrated that the freestream Mach number was fairly constant across the tunnel cross section.

D.   COMPOSITE

At Mach 4, the flat upper surface of the 15°-wedge leading edge model is predominantly comprised of constant pressure areas over all pitch angles tested. The only exceptions on the 15°-wedge leading edge model are the areas influenced by the normal shock associated with the sting and from irregularities caused by the imperfect machining process.   The flat upper surface of the 45°-wedge leading edge model is characterized as nearly constant, but it appears to have additional pressure influences beyond the normal shock from the sting and machining irregularities.

The attached shock over the forward portion of the 15°-wedge leading edge model separated the upper and lower surface flows even at a freestream Mach number below design, as indicated by the constant pressure region on the upper surface of the 15°-wedge leading edge model. The small (light blue) lower pressure regions, evident near the trailing edges of the 15°-wedge leading edge model at all pitch angles, is the result of the combination of the machining irregularities and the decrease in pressure loss across the oblique shock as the shock curves around the waverider planform leading edge (assuming the expansion process around the curved leading edge is constant). It is in the realm of possibility that the expanding lower pressure region is due to flow separation and associated vorticies, but flow separation is rejected (on the 15°-wedge leading edge model) because the region is confined to a very small area between the shock from the sting and the planform edge and does not appear to change with angle of attack. Under these assumptions, the 15°-wedge leading edge model appears to have similar characteristics as low angle of attack delta wings operating within region C as described by L.C. Squire [Ref. 6].

The shadowgraph images of the 45°-wedge leading edge model indicates a detached shock and illustrates the textbook detached shock phenomenon described in Zucker [Ref. 23]. The detached shock and relatively high Mach number of the 45°-

wedge leading edge model indicates that the model has similar characteristics to higher angle of attack delta wings that are operating in region B of Squire's [Ref. 6] flow theory. The assumption is further validated by the growing low-pressure area located near the edges of the 45°-wedge leading edge model planform at all pitch angles. The low pressure regions appear to span or grow larger with increasing angle of attack, further validating the assumption of vortical flow originating just aft of the nose along the edge of the 45°-wedge leading edge planform.

The constant pressure region observed on the 15°-wedge leading edge model at 0° AOA compares well to the CFD analysis conducted by E. Coyne [Ref. 17] using the full three-dimensional Price waverider model at Mach 4. Figure 4.2 is a top view and Figure 4.3 is a side view of the three-dimensional Price configuration (with engine inlets) at a freestream Mach number of 4 [Ref. 17]. The CFD analysis of the Price waverider illustrates that the pressure on the curved upper surface is not only constant, but is at freestream pressure. The top view (Figure 4.2) also illustrates the conical shock location. Evaluating Figures 3.11 (C.1), 4.2 (C.2) and 3.14 (C.3), arranged in Appendix C for direct comparison, it is readily observed that the CFD analysis predicted the shock location extremely well and that the upper surface pressure is constant on both the 15°-wedge leading edge model pressure sensitive paint image and in the CFD analysis.
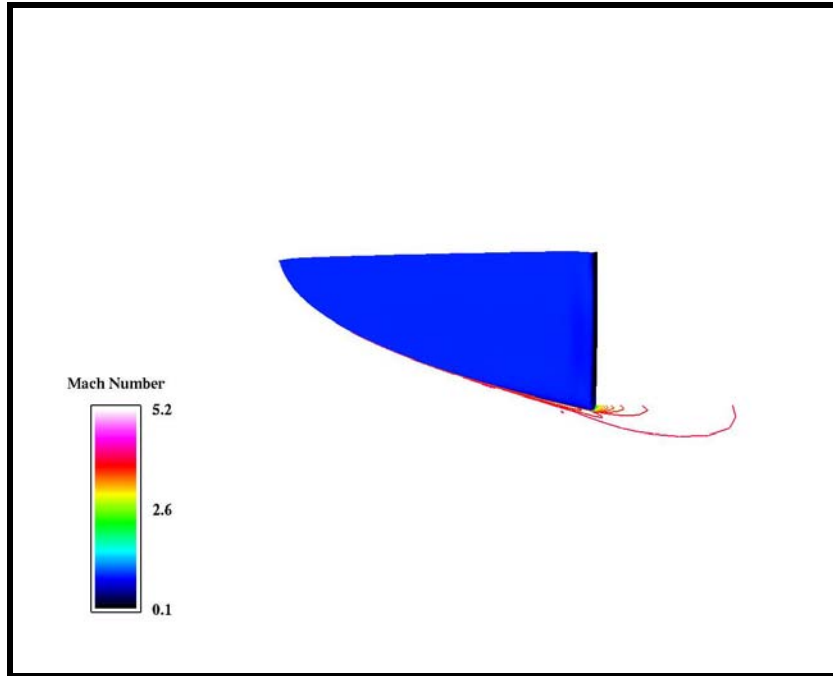
**Figure 4.2.   Mach 4 CFD viscous pressure and Mach contours of the Price
waverider, planform (top) view generated from Ref. 17.**

Theoretical surface pressures on the 15°-wedge leading edge model, derived using the freestream Mach number and oblique shock relations, indicated that the upper surface pressure is equal to freestream pressure and that the upper surface Mach number is 5% below the freestream Mach number.   Oblique shock calculations using the centerline geometry of the 15°-wedge leading edge model are located in Appendix D.   The CFD results indicate that the both the pressure and Mach number on the upper surface are at freestream conditions at 0° AOA and Mach 4.   The Mach number difference on the upper surface between the 15°-wedge leading edge model and the CFD analysis is a result of the double ramp (upper and lower) on the 15°-wedge leading edge model.

57
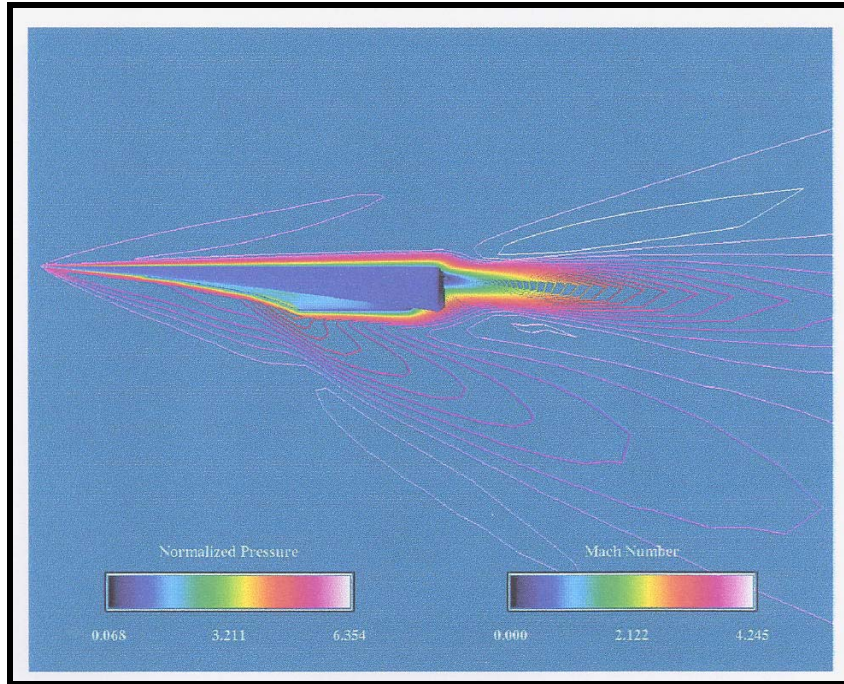
Figure 4.3.   Mach 4 CFD viscous pressure and Mach contours of the Price waverider, horizontal (side) view copied from Ref. 17.

The 15° ramp on the upper surface creates an oblique shock and associated total pressure loss. The pressure loss from the oblique shock does not allow the planform model to achieve both freestream Mach number and pressure concurrently. The 15°-wedge leading edge model mounted horizontally at 0° AOA, Figure 3.3 (C.4) and Mach 4 CFD analysis side-view, Figure 4.3 (C.5), is placed in Appendix C for direct comparison. The upper surface oblique shock on the shadowgraph image of the planform model is noted as a large difference.   Additionally, the lower surface oblique shock of the planform model is larger than the CFD analysis by roughly 5°.

V. CONCLUSIONS AND RECOMMENDATIONS

The conical shocks demonstrated in supersonic testing at Mach 4 on the Price waverider planform 15°-wedge leading edge model mounted in the vertical position (top view) were matched closely by CFD analysis. Horizontal shock patterns and upper surface Mach numbers of the 15°-wedge leading edge planform model did not correlate well to CFD results because the 15°-wedge leading edge model's leading edge does not represent the true leading edge of the Price waverider. However, the constant and uniform upper surface pressure calculation for the flat plate planform model matches the value and constant distribution predicted by CFD. Furthermore, both models (15°-wedge leading edge and 45°-wedge leading edge) prove that Squire's flowfield theory can be extended to waveriders. Both models tested herein suggest that the upper surface flow is separated from the lower surface flow at Mach numbers below the design Mach number.

The similarities in supersonic flow solutions, between the tests conducted on the flat plate planform and CFD analysis, are the beginning of the validation process of the supersonic CFD analysis performed on the Price waverider. Continued testing at all Mach numbers is necessary to determine if the supersonic flowfield of the full three-dimensional Price waverider can be closely predicted using a simplified flat plate model.

A new planform model, carefully designed to match cross section properties of the Price waverider should be designed and built for future supersonic experiments. The leading edge of the new model should have a flat upper surface and a single 7° ramp on the lower surface in order to better replicate the Price waverider. The model should also be designed to incorporate one pressure tap on each surface (upper and lower) in order to obtain a direct comparison of pressures between CFD results and test results.

Before supersonic tests, utilizing sting-mounted models, can be accomplished in the NPS supersonic wind tunnel, the Mach 1.7 and Mach 2.8 nozzle blocks must be modified. Additional improvements to the sting and sting mount should be made to facilitate the use of pressure taps and associated internal pressure lines required.

Further improvements to the NPS supersonic wind tunnel facility can be made by purchasing and integrating a balance to measure lift, drag, and moments and by designing or purchasing variable nozzle and variable diffuser nozzle blocks order to test full ranges of Mach numbers and to improve the tunnel starting capabilities with models installed.

LIST OF REFERENCES

1. Price, D.R., <u>Optimization and Performance Analysis of a Supersonic Conical-Flow Waverider for a Deck-Launched Intercept Mission</u>, Masters Thesis, Naval Postgraduate School, Monterey, California, June 1993.

2. Johnson, L.M., <u>Hydrodynamic Flowfield Visualization Studies of a Mach 6 Waverider</u>, Masters Thesis, Naval Postgraduate School, Monterey, California, March 1994.

3. Ward, L., "Riding the Shock Wave," *Skyline*, North American Aviation, V 19, No. 1, March 1961.

4. Bertin, J.J. and M.L. Smith, *Aerodynamics for Engineers*, Third Edition, Prentice-Hall, Inc., Upper Saddle River, New Jersey, 1998.

5. Seddon, J. and A. Spence, "The Use of Known Flow Fields as an Approach to the Design of High Speed Aircraft," *Hypersonic Boundary Layers and Flow Fields*, AGARD CP No. 30, Royal Aeronautical Society, London, May 1968.

6. Squire, L.C. "Flow Regimes Over Delta Wings at Supersonic and Hypersonic Speeds," *Aeronautical Quarterly*, Volume 27, February 1976.

7. Bowcutt, K.G., J.D. Anderson, and D. Capriotti, "Viscous Optimized Hypersonic Waveriders," Preprint *AIAA-87-0272*, AIAA 25th Aerospace Sciences Meeting, Reno, Nevada, January 1987.

8. Corda, S. and J.D. Anderson, "Viscous Optimized Hypersonic Waveriders From Axisymmetric Flow Fields, " Preprint *AIAA-88-0369*, 26th Aerospace Sciences Meeting, Reno, Nevada, January 1988.

9. Anderson, J.D., M.J. Lewis, and S. Corda, "Several Families of Viscous Optimized Hypersonic Waveriders – A Review of Waverider Research at the University of Maryland," Proceedings *of the First International Hypersonic Waverider Symposium*, College Park, Maryland, October 1990.

10. Anderson, J.D., *Introduction to Flight*, Third Edition, McGraw-Hill Inc., New York, New York, 1989.

11.   Vanhoy, D. L., <u>Low-Speed Wind Tunnel Testing of a Mach 6 Viscous Optimized Waverider</u>, Masters Thesis, University of Maryland, College Park, Maryland, May 1988.

12.   Miller, R W., B. M. Argrow, K. B. Center, G. J. Brauckmann, and M. N. Rhode, "Experimental Verification of the Osculating Cones Method for Two Waverider Forebodies at Mach 4 and 6," Preprint *AIAA-98-0682*, 36th Aerospace Sciences Meeting, Reno, Nevada, January 1998.

13.   Sabean, John, W. and M. J. Lewis, "Performance of a Power Law Star Body" Preprint *AIAA-98-1617*, 1998.

14.   "Aerospaceweb.org," [http://www.aerospaceweb.org/design/waverider/waverider.shtml], August 14, 2001.

15.   Cedrun, M. E., <u>Low-Speed Wind Tunnel Testing of the NPS/NASA Ames Mach 6 Optimized Waverider</u>, Masters Thesis, Naval Postgraduate School, Monterey, California, June 1994.

16.   Huff, M. R., <u>A Labview© Based Wind Tunnel Data Acquisition System</u>, Masters Thesis, Naval Postgraduate School, Monterey, California, September 1998.

17.   Coyne, E., <u>Computational Analysis of the Off-Design Performance of a Mach 6 $\left(L/D \, I_{SP} \right)_{\max}$ Optimized Waverider</u>, Masters Thesis, Naval Postgraduate School, Monterey, California, September 1999.

18.   Pope, A., *Aerodynamics of Supersonic Flight*, Pitman Publishing Corp., New York, New York, 1950.

19.   Pope, A., and K.L. Goin, *High Speed Wind Tunnel Testing*, John Wiley & Sons Inc., New York, New York, 1965.

20.   Baker, W. M., "Recent Experiences With Pressure Sensitive Paint Testing," Preprint *AIAA-2001-0135*, 39th Aerospace Sciences Meeting, Reno, Nevada, June 2001.

21.   Seivwright, D. L., <u>Application of Pressure Sensitive Paint in Shock-Boundary Layer Iteration Experiments</u>, Masters Thesis, Naval Postgraduate School, Monterey, California, March 1996.

22.   Muller, J. A., <u>Calibration to Determine Pressure and Temperature Sensitivities of a Pressure Sensitive Paint</u>, Masters Thesis, Naval Postgraduate School, Monterey, California, June 2000.

23.   Zucker, R.D., *Fundamentals of Gas Dynamics*, Matrix Publishers Inc., Chesterland, Ohio, 1977.

24.   Anderson, J.D., *Fundamentals of Aerodynamics*, Second Edition, McGraw-Hill Inc., New York, New York, 1991.

25.   Cockrell, C.E., L.D. Huebner, and D.B. Finley, "Aerodynamic Performance and Flow-Field Characteristics of Two Waverider-Derived Hypersonic Cruise Configurations," Preprint *AIAA-95-0736*, 33rd Aerospace Sciences Meeting, Reno, Nevada, January, 1995.

26.   Cockrell, C.E., L.D. Huebner, and D.B. Finley, "Aerodynamic Characteristics of Two Waverider-Derived Hypersonic Cruise Configurations," *NASA °°Technical Paper 3559*, Langley Research Center, Hampton, Virginia, July 1996.

27.   Roskam, J. and C. E. Lan, *Airplane Aerodynamics and Performance*, Roskam Aviation and Engineering Corp., Ottawa, Kansas, 1980.

28.   Kuethe, A. M.and J. D. Schetzer, *Foundations of Aerodynamics*, John Wiley & Sons, Inc., New York, New York, 1950.

29.   Nicolai, L.M., *Fundamentals of Aircraft Design*, Mets Inc., San Jose, California, 1975.

THIS PAGE INTENTIONALLY LEFT BLANK

APPENDIX A. MACH 1.7 AND 2.8 RESULTS

A.   TEST SCHEDULE

Initial supersonic testing began on June 26, 2001 using the Mach 1.7 nozzle blocks that were already installed. The Mach number for the nozzle blocks was well documented by numerous testing runs completed for class work over the past few years, abrogating the need for calibration. During the first test, the 45°-wedge leading edge model started spinning uncontrollably (rotating on its longitudinal axis) shortly after the normal shock entered the test section. Close inspection of the test apparatus revealed that the 45°-wedge leading edge model was slightly misaligned horizontally (yawed) with the 0° AOA sting due to a tiny amount of play in the three set-screws that held and connected the 45°-wedge leading edge model to the sting. During the test, the misalignment created a sideslip condition resulting in a large enough force and moment to overcome the hold of the four Allen screws in the sting mount. Once the hold was broken the 45°-wedge leading edge model was free to spin. The solution to the spin problem involved drilling precision holes into the three stings (0°, 2° and 4° AOA) coinciding with the location of the Allen screws on the sting mount. The drilled holes were sized to be just large enough to enable the tips of the Allen screws to penetrate below the surface of the shaft providing a tighter grip and preventing spinning.   The modification also resulted in quicker alignment and assembly of each sting to the sting mount. In addition to the modification, closer attention was paid to the alignment between the model and each sting prior to all subsequent tests.

Mach 1.7 testing resumed on July 2, 2001. The 45°-wedge leading edge model and modified 0° AOA sting were placed in the tunnel with the shadowgraph and pressure measurement system operating. Using a Polaroid camera, a picture was taken before the test was initiated to record the reference position of the 45°-wedge leading edge model. The supersonic wind tunnel pneumatic valve was opened and the first test was then

initiated. A shadowgraph image of the 45°-wedge leading edge model at 0° AOA was captured during supersonic tunnel operation when the plenum pressure reached a steady 20 psig. After the picture was taken, the Polaroid camera was removed, allowing the shadowgraph image to be projected onto the screen. A short time interval passed before the 45°-wedge leading edge model started spinning uncontrollably for the second time. The test was halted and the 45°-wedge leading edge model, sting, and sting mount were removed from the test section. An inspection revealed that the Allen screws were not tightened properly due to human error. The screws were secured, the 45°-wedge leading edge model was placed in the wind tunnel and the test was completed without further incident. It was determined that closer attention would be paid to the Allen screws on the sting mount and that lock-tight would be used during subsequent tests to ensure that vibrations and forces would be unable to loosen the connection.

The desired flow over the 45°-wedge leading edge model was not established during the Mach 1.7 tests, because the supersonic wind tunnel was choked and never started. The tunnel was assumed to be choked by too much blockage from the sting mount. In addition to the sting mount blockage, model vibration was also noticed. Both the tunnel and model required modifications before testing resumed. The solution for sting mount blockage was to drill and tap two 17/32-inch diameter holes into each mounting plug. One hole was used to connect 1/2inch steel tubing with a valve and 90° elbow. A 1/2-inch plug was screwed into the second hole. Figure A.1 shows one of the two identical mounting plugs after the modifications. The four holes, when open, were designed to allow air from the test section to escape at the critical blockage point and enable the tunnel to start. Model vibration was solved by custom fitting and installing a 1/100-inch shim between the model and 0° AOA sting in order to create a tighter fit and stronger hold.
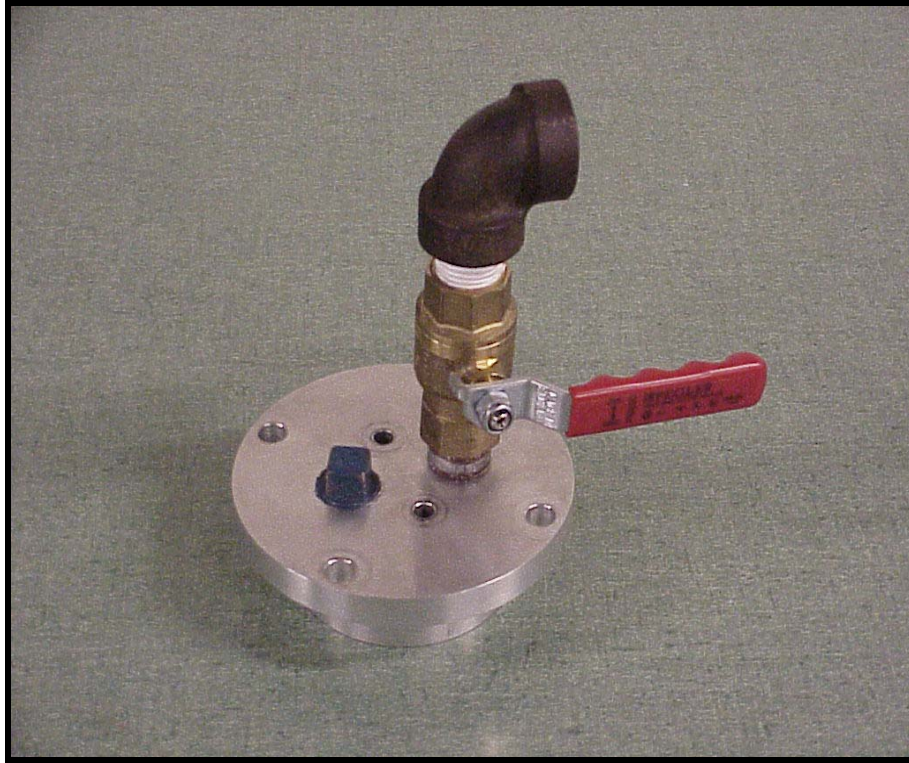
Figure A.1.   Mounting plug after installation of 17/32-inch diameter relief holes.

The modified model assembly and plugs were installed in the test section and testing initiated the next day (July 3, 2001). Model vibration was significantly reduced and no spinning occurred. The plenum pressure was set at 20 psig, the four holes opened, tunnel static pressure recorded and the shadowgraph image was photographed. The four relief holes drilled into the plugs did not reduce flow choking. In fact, the condition worsened. The 45°-wedge leading edge model and 0° AOA sting were then removed from the test section leaving only the sting mount in the tunnel. The sting mount was fastened securely in-place and positioned backwards to ensure that the 7/16-inch diameter opening (for the sting) would not adversely interfere with the flow. Tests were conducted varying the plenum pressure from 20 to 40 psig in increments of 10-psig while varying the condition of the four relief holes.   At a plenum pressure of 20 psig, it was observed that air is sucked into the test section rather than the desired effect of air being blown out of the mounting (and diffuser) section relieving the blockage effect. Tape was placed over the two relief holes without valves and the plenum pressure was increased to 30 psig. As the pressure increased, the tape was sucked in until a pressure of 25-28 psig was

attained, when a transition occurred. At plenum pressures above 28, the tape developed a bubble; indicating out-flow pressure. (Note: Using the Mach 1.7 nozzle blocks and opening the relief holes quickly drains the air supply) The 45°-wedge leading edge model was re-installed in the test section to determine if the presence of the model (at 40 psig) would puncture the large standing normal shock in the test section by creating upper and lower oblique shocks; enabling the tunnel to start. The 45°-wedge leading edge model was installed with no improvement in the test section flow. Significant model vibration began to be encountered at 40 psig impeding further testing at higher plenum pressures, and the possibility of starting the tunnel by overpowering the system. Testing for Mach 1.7 was discontinued without any pressure-sensitive paint measurements due to the inability to start the tunnel.

The Mach 2.8 nozzle blocks were installed and supersonic testing resumed on July 10, 2001. Figure A.2 is a picture of the Mach 2.8 nozzle blocks taken during the installation process. The first test was conducted as a calibration run using a clean supersonic wind tunnel (no model, sting or sting mount installed) with all valves and relief holes closed. The plenum pressure was gradually increased and the test section was closely monitored using the shadowgraph image projected on the screen. The normal shockwave passed through the test section yielding uniform flow and indicating tunnel start at 40-psig plenum pressure.
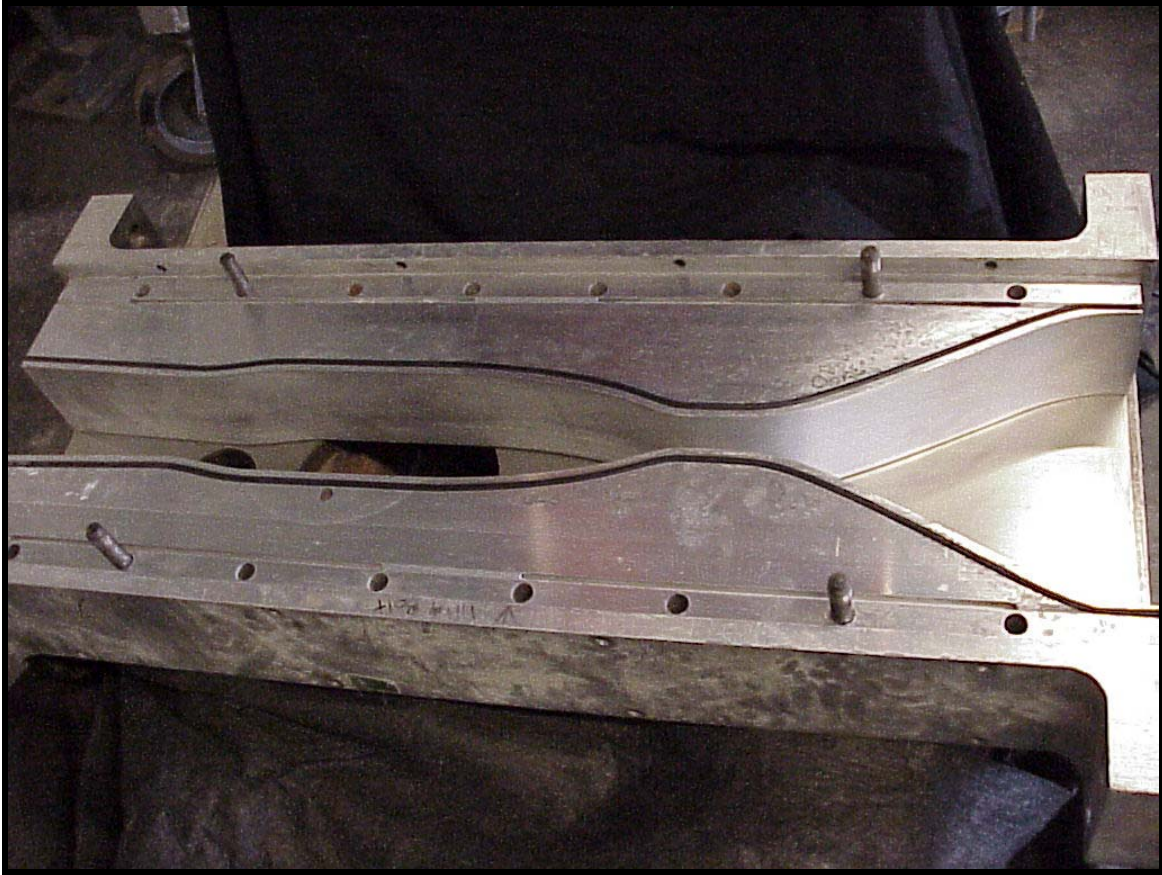
Figure A.2.   Interior view of the Mach 2.8 nozzle block design.

The second set of tests using the Mach 2.8 nozzle blocks was conducted to determine if the tunnel could be started with only the sting mount installed. Plenum pressures of 40, 50 and 60 psig were used in addition to opening the outflow valves, but the tunnel remained choked.   The 45°-wedge leading edge model and 0° AOA sting were placed in the test section to see if their presence in the test section improved flow conditions. However, the test section remained choked and the normal shock was pushed further upstream. No model vibration occurred even when the plenum pressure was 60 psig.   The model was rotated to the vertical position to determine whether or not having the model out of plane with the sting mount would change the choked flow condition. The vertically mounted model resulted in a slight improvement in the normal shock location (further downstream in the test section) when compared to the horizontal placement of the model at the same plenum pressure.

The final tests using the Mach 2.8 nozzle blocks were conducted to isolate and determine the factors creating blockage in the wind tunnel that caused the tunnel to remain choked. A sharp cone and its 0° AOA sting were inserted into the supersonic wind tunnel (Figure A.3) using the same sting mount utilized in all previous testing. The cone and its sting were selected because of their availability and the fact that they were previously used in successful wind tunnel tests conducted using the Mach 4 nozzle blocks. The use of the cone was to experimentally determine whether or not a sharper object could puncture and collapse the normal shock into oblique shocks and allow the tunnel to start. The plenum pressure was methodically increased to 70 psig but the flow remained choked. The outflow valves were opened and closed with no noticeable improvement in the location of the shock in the test section. The 0° AOA sting used to hold and mount the waverider was placed in the tunnel. The plenum pressure was varied from 40 psig to 65 psig, but the wind tunnel remained choked. Testing was halted while the nozzle blocks were changed for Mach 4 testing.
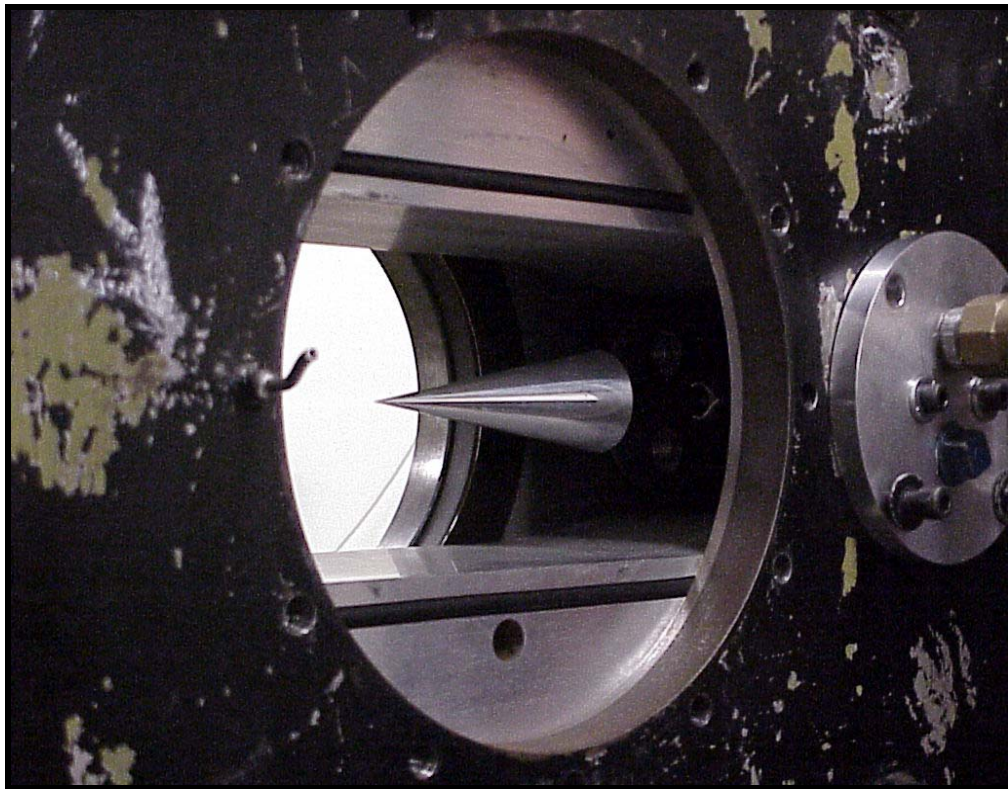
Figure A.3.   Sharp cone mounted in NPS supersonic wind tunnel.

B.   DATA REDUCTION

1.   Shadowgraph

The shadowgraph image of the test section was projected onto the screen, but no pictures were taken during the first supersonic run at Mach 1.7 because the test was used to verify the integrity of the wind tunnel and 45°-wedge leading edge model. The test section integrity and shadowgraph image of the model projected on the screen were monitored during the test run. As the plenum pressure increased above 15 psig, a normal shock entered the test section and physical control of the model was lost.

Before the second set of Mach 1.7 tests were initiated a wind-off reference picture of the 45°-wedge leading edge model and 0° AOA sting was taken, Figure A.4, using a Polaroid camera. The wind-off picture indicated a discontinuity in the glass windows of the test section that went unnoticed to the naked eye, but became readily apparent when the shadowgraph image was viewed. Using Figure A.4 as a reference, the discontinuity extends in a triangular shape from the center of the picture encompassing the upper left quadrant. (Note: The shadowgraph image of the test section appears inverted on the screen, but all recorded shadowgraph images were re-inverted using Microsoft Photo Editor, before being inserted into this document). The abnormalities of the glass also make the model appear warped.
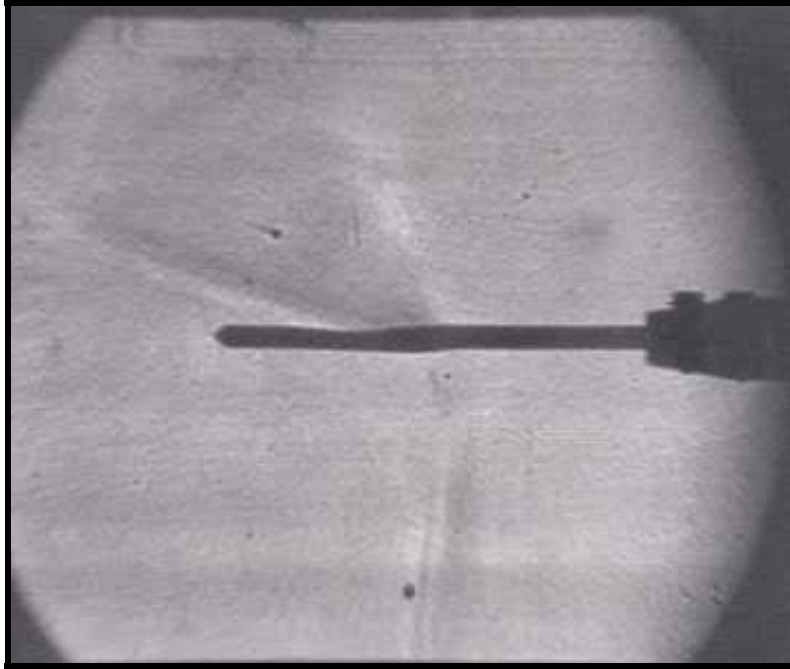
Figure A.4. **Sting-mounted 45°-wedge leading edge model 0° AOA shadowgraph reference image.**

At a plenum pressure setting of 20 psig, a (wind-on) picture was taken, Figure A.5, prior to the 45°-wedge leading edge model spinning uncontrollably, about its longitudinal axis, for the second time. Figure A.5 indicates the presence of a weak normal shock located near the leading edge and large boundary layers (top and bottom). The thicker appearance of the shock wave and model cross section (side view) are created by model vibration and unsteady test section flow. The standing normal shock wave in a test section constantly moved, but the model vibration appeared to amplify the unsteady nature of the shock wave.

After model and tunnel modifications, designed to stop model vibration and to relieve the choked flow, Mach 1.7 testing resumed. The plenum pressure was increased steadily while the shock and boundary layer locations and thicknesses were monitored using the shadowgraph image projected onto the screen. The standing normal shock remained positioned at the nose of the model, even at a plenum pressure of 40 psig, regardless of the position of the four relief valves. Slight model vibration was noticed and the test was terminated.
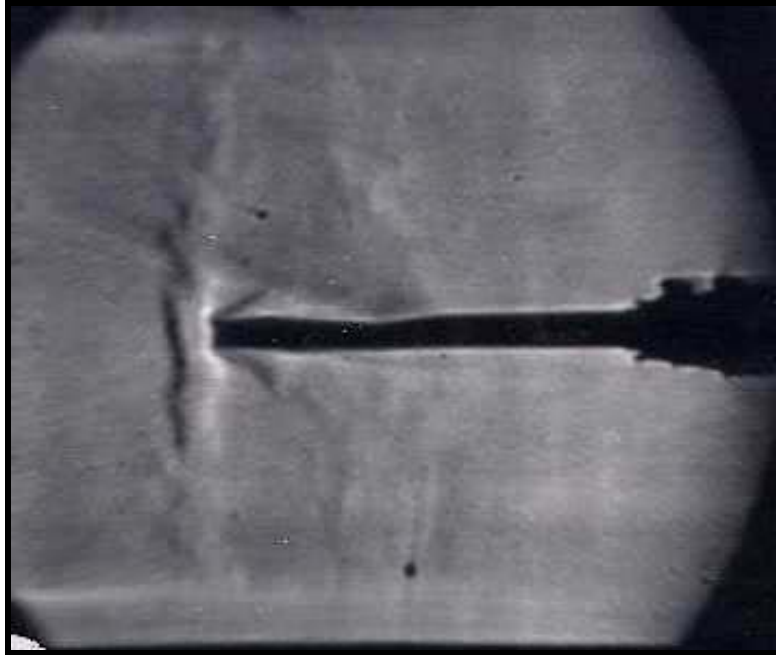
Figure A.5.   45°-wedge leading edge model at 0° AOA with a plenum pressure setting of 20 psig using the M 1.7 nozzle blocks.

In order to complete the Mach 1.7 testing and to verify that the sting mount was the leading cause of choking the flow, the sting mount was installed in the tunnel by itself. During the methodical increase in plenum pressure, a large normal shock became visible in the test section when the plenum pressure reached 25-28 psig. The shock had large lambda-shocks on the top and bottom from strong shock boundary layer interaction. The boundary layers downstream of the shock were very large while the upstream boundary layers were orders of magnitude smaller. Figures A.6 and A.7 were captured using the Sony digital camera, and illustrate the minor difference in shock location when the relief valves were open or closed at a plenum pressure of 40 psig. Large lambda shocks or shock boundary layer interaction can be seen in the images as well as the significant reduction in boundary layer size after the normal shock. At a 50 psig plenum pressure, the normal shock moved slightly further downstream than the 40 psig position with the valves closed. A dramatic change in the shock position occurred when the valves were initially closed and then opened as the plenum pressure was rising above 30 psig as suggested by Figures A.8 and A.9. Boundary layers and shock-boundary layer interactions can also be observed in Figures A.8 and A.9.

Figure A.6. Normal shock resulting from sting mount blockage using Mach 1.7 nozzle blocks with 40 psig plenum pressure and relief valves closed.

Figure A.7. Normal shock resulting from sting mount blockage using Mach 1.7 nozzle blocks with 40 psig plenum pressure and relief valves open.

Figure A.8.   Normal shock resulting from sting mount blockage using Mach 1.7 nozzle blocks with 50 psig plenum pressure and relief valves closed.

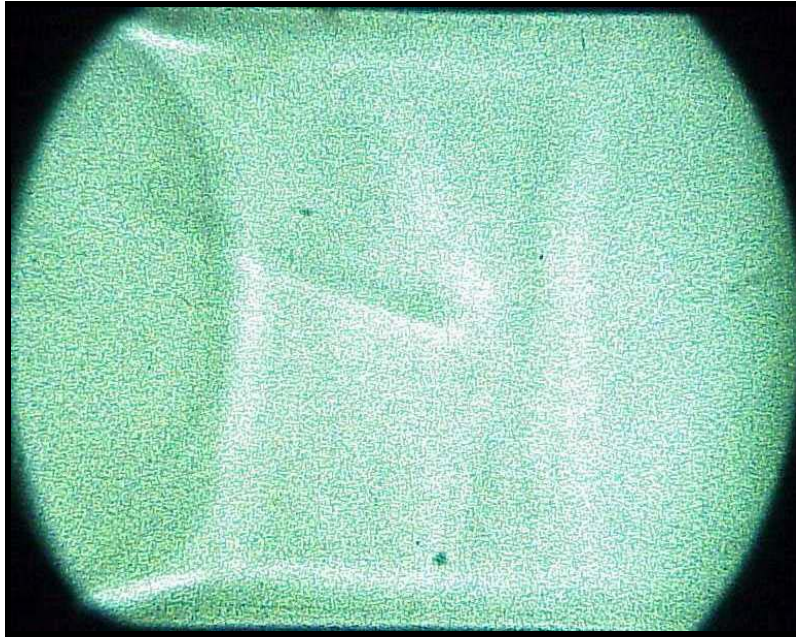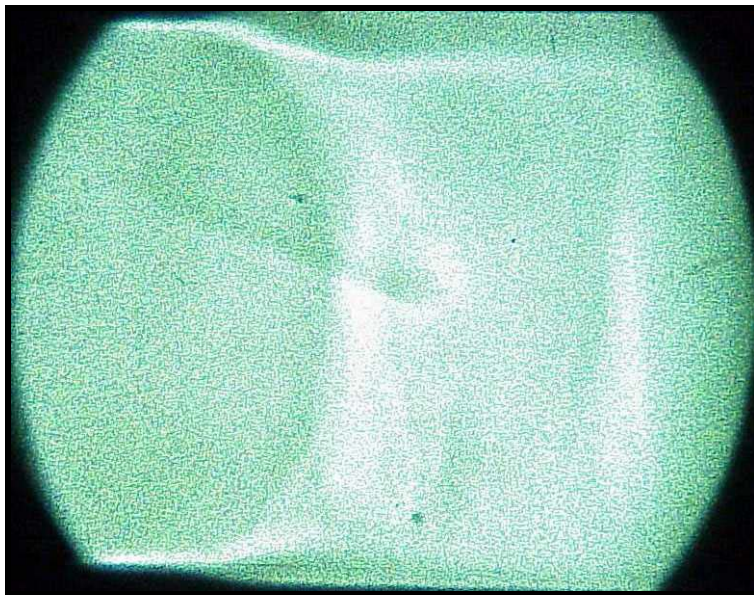**Figure A.9.   Normal shock resulting from sting mount blockage using Mach 1.7 nozzle blocks with 50 psig plenum pressure and relief valves open.**

The initial Mach 2.8 test was completed using a clean tunnel for Mach number calibration. During the test, the plenum pressure was methodically increased in order to

observe the tunnel start and record the required plenum pressure setting. As the plenum pressure reached 35 psig, a short normal shock appeared in the test section. The normal shock was combined with large upper and lower oblique shocks with their associated lambda shock-boundary layer interactions. As the plenum pressure continued to rise to 40 psig, the starting shock moved past the test section and the tunnel was officially started. It was observed that the boundary layer prior to the shock was very large and was much smaller after shock passage.

The second set of tests using the Mach 2.8 nozzle blocks were initiated to determine whether or not the sting mount would create too much blockage and choke the tunnel. After the tunnel was started and the plenum pressure increased to 40 psig, a short normal shock with long trailing upper and lower oblique shock were observed deep into the test section as shown in Figure A.10. The oblique shocks were combined with lambda shocks associated with shock-boundary layer interaction. Increasing plenum pressure resulted in the normal shock moving downstream, without allowing the tunnel to start. The 45°-wedge leading edge model was placed horizontally in the wind tunnel operating at a plenum pressure setting of 60 psig, as shown in Figure A.11. However, the standing normal shock, its associated oblique shocks and lambda shocks were pushed further upstream. The 45°-wedge leading edge model was rotated 90° to the vertical position, Figure A.12, at the same plenum pressure setting. This resulted in a noticeable improvement in the shock location when compared to the horizontally mounted model. With the model in the vertical position many shock interactions were visible slightly upstream and to the sides of the model including the lambda shocks associated with shock boundary layer interactions and compression waves associated with imperfect nozzle expansion.

A sharp cone was placed in the supersonic wind tunnel. The tunnel remained choked even at a plenum pressure setting of 70 psig. Shock patterns very similar to those detected with the vertically mounted model were observed and are shown in Figure A.13.

The final Mach 2.8 nozzle block tests were completed with only the sting installed in the sting mount. At 40 psig plenum pressure, a short normal shock with large trailing upper and lower oblique shocks entered the test section. The location of the normal

shock was close to the position of the normal shock associated with the 45°-wedge leading edge model.

The plenum pressure was increased to 65 psig, as shown in Figure A.14. The shock location is shown to be further forward than the shock location associated with the sting mount at a plenum pressure of 40 psig shown in Figure A.10. All testing using the Mach 2.8 nozzle blocks was terminated because the normal shock location at 65 psig was too far upstream to provide any hope of overpowering the system and clearing the choked condition.

(a) (b)

Figure A.10. Normal, oblique and lambda shocks created by blockage from sting mount at plenum pressure setting of 40 psig using Mach 2.8 nozzle blocks. Image (a) is the raw image, image (b) is enhanced for illustration.

<div align="center">(a)   (b)</div>
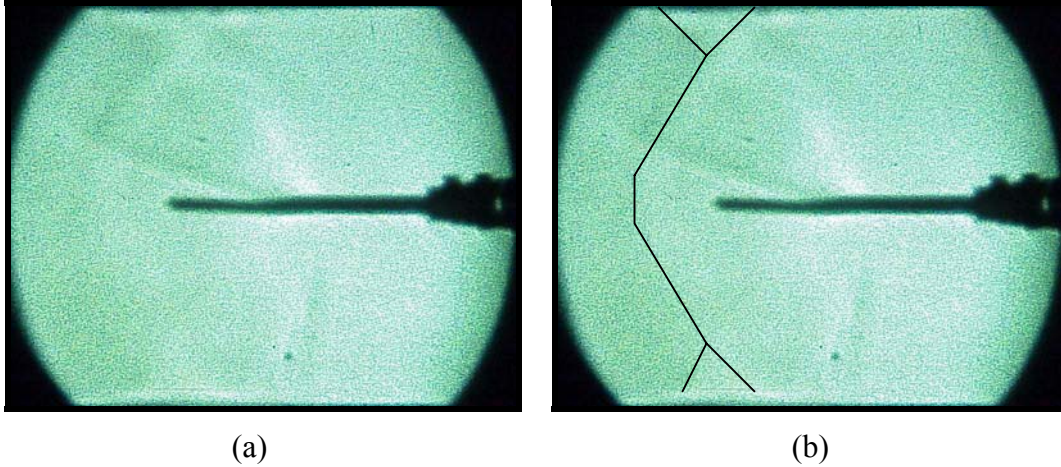
Figure A.11. Normal, oblique and lambda shocks created by blockage from horizontal 45°-wedge leading edge model at a plenum pressure setting of 60 psig using Mach 2.8 nozzle blocks. Image (a) is the raw image, image (b) is enhanced for illustration.

<div align="center">(a)   (b)</div>
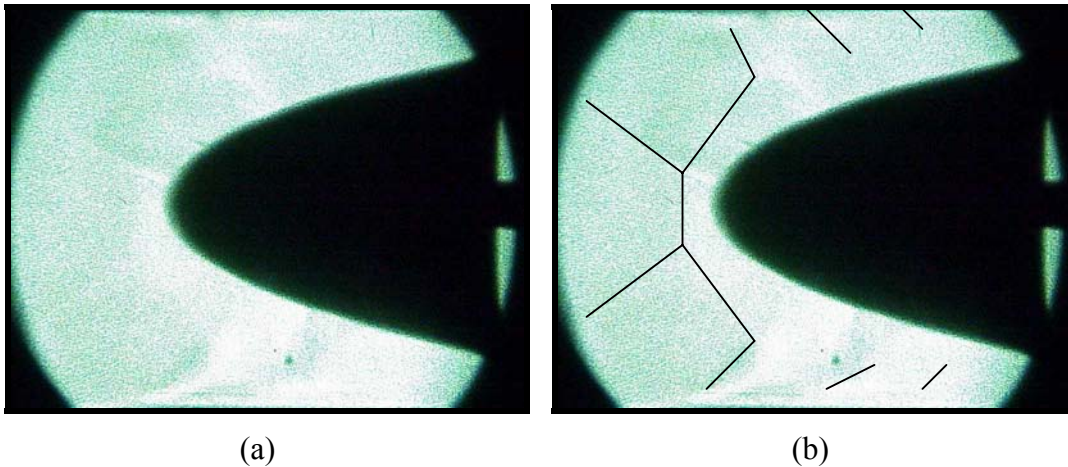
Figure A.12. Normal, oblique and lambda shocks created by blockage from vertical 45°-wedge leading edge model at a plenum pressure setting of 60 psig using Mach 2.8 nozzle blocks. Image (a) is the raw image, image (b) is enhanced for illustration.
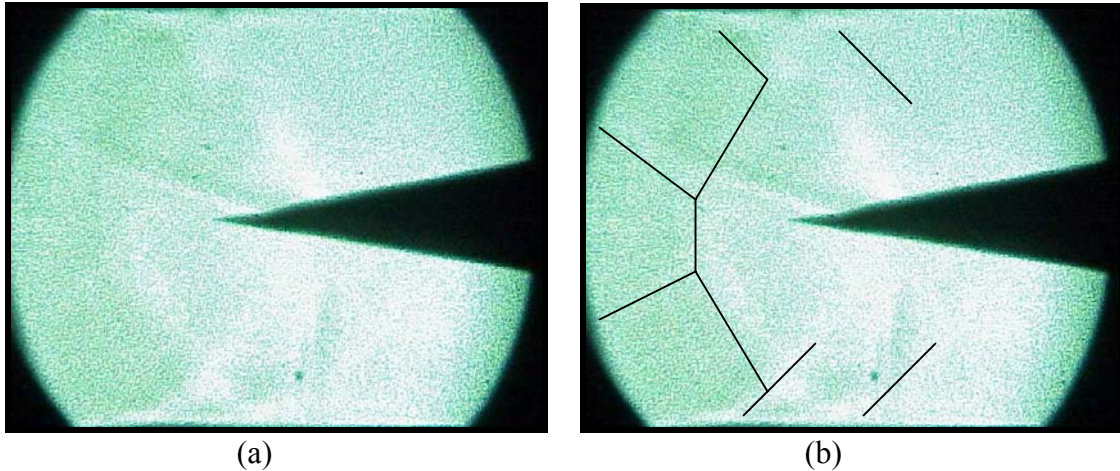
Figure A.13.   Normal, oblique and lambda shocks created by blockage from sharp cone at a plenum pressure setting of 70 psig using Mach 2.8 nozzle blocks. Image (a) is the raw image, image (b) is enhanced for illustration.
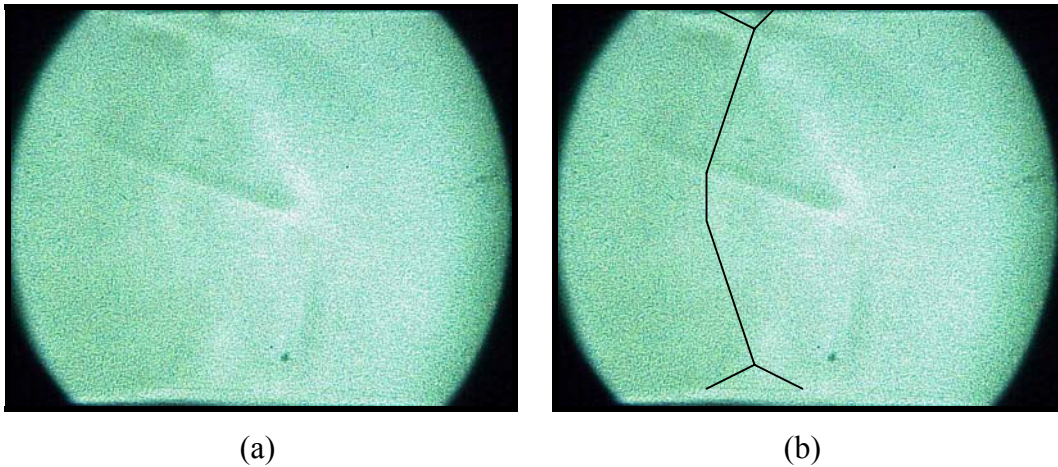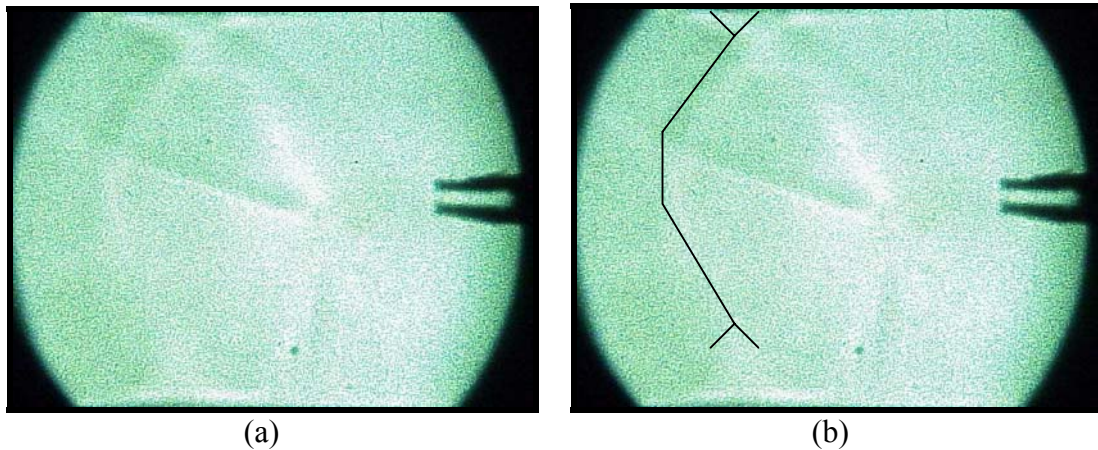

Figure A.14.   Normal, oblique and lambda shocks created by blockage from the 0° AOA sting at a plenum pressure setting of 65 psig using Mach 2.8 nozzle blocks. Image (a) is the raw image, image (b) is enhanced for illustration.

2.   Test Section Pressure Measurements

Plenum and test section pressures measured during the initial Mach 1.7 tests indicated that the test section Mach number was actually 1.68. The slightly lower Mach number combined with the choked flow condition suggests the presence of disturbances or losses in the tunnel at or near the location of the static pressure tap.   After the modification to the plugs, designed to relieve the flow past the sting mount, pressure

readings were taken with all (four) relief valves open at a plenum pressure setting of 20 psig. The Mach number (determined from the pressure readings) was reduced to Mach 1.31. The significant drop in Mach number can only be explained by the presence of a normal shock in the divergent portion of the nozzle upstream from the static port. The final run, conducted at 40 psig plenum pressure with 2 relief-valves open, yielded a Mach number of 1.62.

The initial run using the Mach 2.8 nozzle blocks was a calibration run conducted using a clean (no model or sting mount) wind tunnel. After the tunnel started, the plenum and test section pressures were taken. The data revealed that the test section Mach number was only 2.05. The large disparity in Mach number is due to the nozzle block shape being designed without accounting for boundary layers on the four sides of the nozzle and tunnel. The area reduction created by the boundary layer(s) resulted in a lower Mach number. With the 45°-wedge leading edge model mounted in the test section, the plenum and static pressures indicated a slight rise in Mach number to 2.10. The slight difference in Mach number is near the statistical uncertainty of the pressure readings, but it is also possible that the presence of the model in the test section slightly increases the nozzle efficiency by causing a small boundary layer reduction in the nozzle. ZOC pressure results for Mach 1.7 and Mach 2.8 nozzle blocks can be found in Table B.1 of Appendix B.

C. DISCUSSION

1. Shadowgraph

The shadowgraph test results using the Mach 1.7 nozzle blocks indicate that the sting mount creates too much blockage for proper supersonic flow to be established. The shock location at 50 psig plenum pressure with the relief valves open, Figure A.9, is still less than half way through the test section. The poor shock location combined with the high pressure setting (more than the double normal Mach 1.7 operating pressure) provides no indication that the choked condition can be overcome by any means other than redesign of the sting mount and/or nozzle blocks.

Tests conducted using the Mach 2.8 blocks indicate that the blockage is due to both the sting and sting mount.   Comparing Figures A.10 and A.11, it can be readily observed that the 45°-wedge leading edge model forced the small normal shock slightly upstream, increased the oblique shock angles and lengthened the lambda shocks. Rotating the model 90° to the vertical position enabled the model to be positioned out of plain with the sting and sting mount, resulting in a very minor improvement in shock location.   The deduction is that the model size does not adversely affect the choked condition by adding to the blockage.   However, the bluntness of the 45°-wedge leading edge model pushes the shock upstream instead of allowing the normal shock to attach to the leading edge and collapse into oblique shocks.   Figures A.11 and A.14 indicate that the sting is a significant source of test section flow blockage.   The sting (and sting mount) pushes the normal shock upstream to nearly the same location in the test section as the 45°-wedge leading edge model.   Figure A.10 shows that the sting mount creates enough blockage by itself to severely choke the flow.   Furthermore, the degree in which the normal shock location is pushed further upstream by the sting, Figure A.14, indicates that the sting increases the flow blockage in a cumulative manner.

2.   Pressure Measurements

The initial Mach 1.7 ZOC pressure measurements with relief holes closed indicated a slightly lower Mach number than previous nozzle block operations. However, determining the Mach number using the ratio of test section static to total (plenum) pressure is not the most precise method because of pressure inacuracies. Therefore, the indicated Mach numbers of just over 1.68 are within reason, but it is also possible that a shock is located near the static port resulting in the lower Mach number. The pressure measurements indicating test section Mach numbers of 1.31 and 1.61 are due to the open relief holes.   The lower Mach numbers, 1.31 and 1.61, are a result of increased blockage from the suction of ambient air into the sting mount region when the relief valves are open and the plenum pressure is below 28 psig.

The ZOC pressure measurements for the Mach 2.8 nozzle blocks indicate a test section Mach number of 2.05, which is much lower than the nozzle design Mach number

and was not expected. The plenum pressure is at the limit of the ZOC pressure system but well within the calibration limits. Small Mach number errors are probable, but not on the order indicated.

3.   Composite

The Mach 1.7 nozzle blocks cannot incorporate the sting mount in its current configuration for any useful testing. The lower the Mach number, the more critical the area requirements become for the test section and second throat (diffuser). The current sting mount creates too much blockage and chokes the flow. The nozzle blocks do not have a second throat, instead the area slightly increases aft of the test section resulting in a virtual second throat when the boundary layer increases. The relief holes when opened resulted in worse test section flow conditions because the ambient air is sucked into the test section at normal tunnel operating pressures. The combination of the weak shock, lower test section Mach number and large boundary layers on both sides of the normal shock in the test section when the 45°-wedge leading edge model was installed indicates that there are unseen shock events upstream that are most likely positioned near the test section static port or in the short distance between the test section static port and the observation windows.

When the sting mount was installed, the boundary layers downstream of the shock were very large while the upstream boundary layers were orders of magnitude smaller further indicating additional shock phenomena when the 45°-wedge leading edge model was installed. At 20 psig, with the model installed, the test section Mach number was 1.68 with no relief holes open. When four relief holes were opened, the Mach number reading was drastically reduced to 1.31. At the same pressure, with only the sting mount installed and two relief holes open, the test section Mach number was 1.62. The 20 psig data clearly supports the observation that the relief holes were sucking air into the critical

blockage area and reducing the chances of starting the tunnel. Furthermore, the test section Mach number is reduced when the normal shock is forced upstream (forward) into the nozzle by blockage. The result is that the sting mount is too large and will not allow the tunnel to start in any condition and the 45°-wedge leading edge model is not sharp enough to be used as a catalyst for tunnel start.

The Mach 2.8 nozzle blocks were designed using ideal (isentropic) relationships and based completely on area ratio. In actuality, boundary layers on all four walls play a significant factor in designing the proper nozzle area ratio and second throat area in order to achieve a specific Mach number. The Mach 2.8 nozzle blocks had a significantly reduced Mach number (2.05) even when the wind tunnel was operated empty during the calibration test run. Inspection and measurement of the Mach 2.8 nozzle blocks when the nozzle blocks were being removed revealed that the second throat, co-located with the sting mount, is too small in area and that the shallow slope extends the critical area forward. The smaller throat creates blockage and causes a lower test section Mach number that further amplifies the blockage problem. The shallow design of the second throat causes the sting to become an additional source of blockage, further exacerbating the blockage. The installation of the 45°-wedge leading edge model resulted in only a slight improvement in the test section Mach number when compared to the calibration Mach number. The 45°-wedge leading edge model had no effect on shock location when compared to the shock location with the sting installed in the test section. The combination of the poor nozzle design resulting in a significantly lower Mach number, and increased blockage of additional components, indicates that all subsequent tests utilizing the Mach 2.8 nozzle blocks will be unsuccessful until the nozzle blocks are modified or redesigned.

THIS PAGE INTENTIONALLY LEFT BLANK

APPENDIX B.   PRESSURE MEASUREMENTS

ZOC Pressure Measurements						
Date	02-Jul-01		03-Jul-01		10-Jul-01	
Nozzle Blocks	**1.7**		**1.7**		**2.8**	
Atmospheric Pressure (Hg)	29.81		29.78		29.96	
Pressure System	ZOC		ZOC		ZOC	
Collection rate (Hz)	330		330		330	
Samples	5		5		5	
Run #	1	2	1	2	1	2
Tunnel Plenum (psig)	**14**	**20**	**20**	**20**	**60**	**50**
Total (Hg)	57.05	70.13	69.34	71.05	151.37	136.61
Static (Hg)	11.87	14.55	24.46	16.46	17.98	15.09
Ratio (Ps/Pt)	0.208016	0.207459	0.352721	0.23163	0.1188	0.110463
Mach # (Isentropic Tables)	1.68	1.685	1.31	1.62	2.05	2.10
Mach Number (eqn)	**1.682**	**1.684**	**1.317**	**1.610**	**2.047**	**2.093**

Table B.1.   Mach number determined using ZOC pressure measurement system.

Mach 4 Heise Gage Pressure Measurements (back-up)						
Date	17-Aug-01		21-Aug-01		23-Aug-01	
Atmospheric Pressure (Hg)	29.94		29.95		29.92	
Atmospheric Pressure (psi)	14.71		14.71		14.70	
Run #	1	2	1	2	1	2
Plenum (psig)	157	147	160	160	155	155
Total (psia) Pt	171.71	161.71	174.71	174.71	169.70	169.70
Test Section Static (psia)	1.25	1.25	1	1.25	1.25	1.25
Ratio (Ps/Pt)	0.00728	0.00773	0.005724	0.007155	0.007366	0.007366
Mach Number (eqn)	**3.925**	**3.881**	**4.106**	**3.938**	**3.916**	**3.916**

**Table B.2a.   Mach number determined using Heise gage pressure measurement
system Part 1.**

Mach 4 Heise Gage Pressure Measurements (back-up)				
Date	29-Aug-01			
Atmospheric Pressure (Hg)	29.72			
Atmospheric Pressure (psi)	14.60			
Run #	1	2		
Plenum (psig)	157	155		
Total (psia) Pt	171.60	169.60		
Test Section Static (psia)	1	1.25		
Ratio (Ps/Pt)	0.005827	0.00737	AVG	STD DEV
Mach Number (eqn)	**3.925**	**3.881**	**3.961**	**0.087**

Table B.2b.   Mach number determined using Heise gage pressure measurement system Part 2.

Mach 4 Pitot Tube Survey						
Date	23-Aug-01			29-Aug-01		
Atmospheric Pressure (Hg)	29.92			29.72		
Atmospheric Pressure (psi)	14.70			14.60		
Location	Center	-1"	+ 1"	Center	+ 9°	-4.5°
Plenum (psig)	156	155	155	168	156	156
Pt1 (psia)	170.70	169.70	169.70	182.60	170.60	170.60
Pt2 (pitot tube - psia)	23	23	24	22.5	23.5	23.5
Ratio (Pt2/Pt1)	0.134739	0.135533	0.141426	0.123219	0.137748	0.137748
Mach # (Normal Shock)	**4.04**	**4.03**	**3.98**	**4.14**	**4.01**	**4.01**
Mach Number (eqn)	**4.035**	**4.028**	**3.977**	**4.141**	**4.009**	**4.009**

Table B.3.   Mach 4 Pitot Tube Survey.

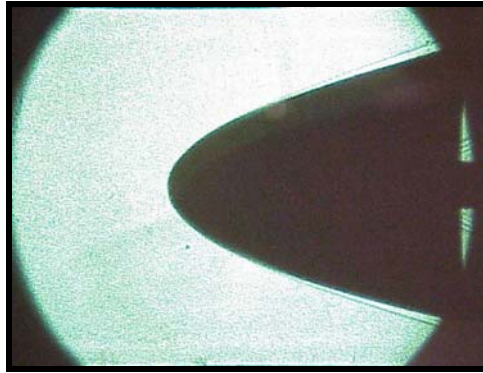# APPENDIX C.   DIRECT COMPARISON OF MACH 4 RESULTS

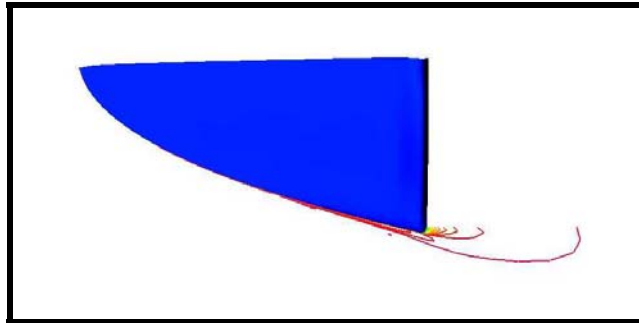**Figure C.1   Mach 4 shadowgraph image of 15°-wedge leading edge model planform at 2° AOA (Figure 3.11).**

Figure C.2   Mach 4 CFD viscous pressure and Mach contours planform (top) view generated from Ref. 17.
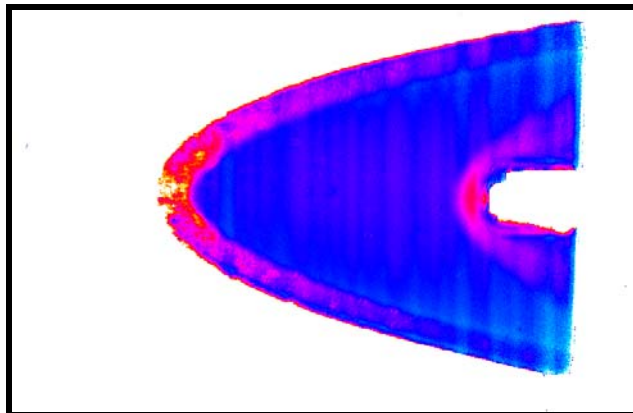

Figure C.3.   Mach 4 pressure sensitive paint image of the 15°-wedge leading edge model at 0° AOA (Figure 3.14).
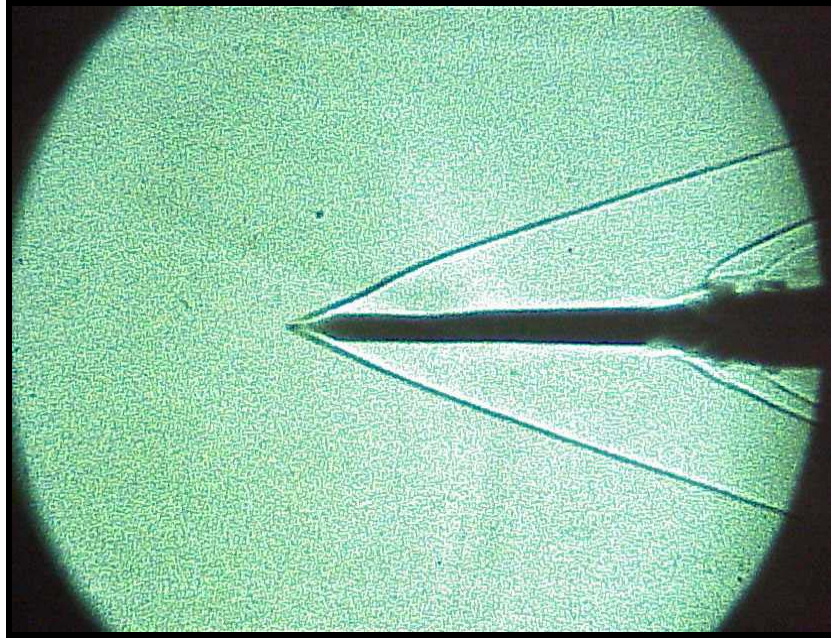
Figure C.4. **Mach 4 shadowgraph image of 15°-wedge leading edge planform model at 0° AOA (Figure 3.3).**
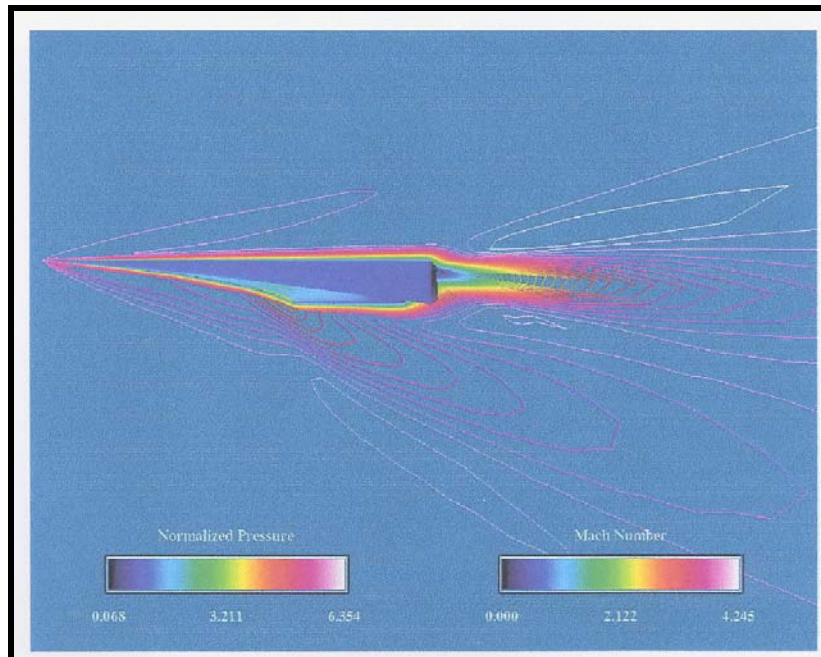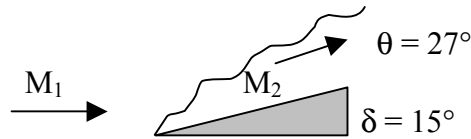

Figure C.5. **Mach 4 CFD viscous pressure and Mach contours horizontal (side) view (Figure 4.3) generated from Ref. 17.**

APPENDIX D.   CALCULATIONS.

Calculation of Mach Number and Pressure on Upper Surface of Waverider Planform

Test Section Flow Conditions

$M_1 = 4$
$p_1 = 180$ psf $= 1.25$ psi
$p_{t1} = 27,330.3$ psf
$T_1 = 123.1°$ R
$T_{t1} = 517°$ R
$a_1 = 543.66$ ft/s
$V_1 = 2,174.64$ ft/s

$\theta = 27°$

$\delta = 15°$

Geometric Equations	Isentropic Relations	Normal Shock Relations
$V_{1n} = V_1 \sin \theta$	$p_t = p\left[1 + \dfrac{\gamma-1}{2}M^2\right]^{\frac{\gamma}{\gamma-1}}$	$T_2 = \left(T_2/T_1\right)T_1$
$M_{1n} = M_1 \sin \theta$		
$V_t = V_1 \cos \theta$	$T_t = T\left[1 + \dfrac{\gamma-1}{2}M^2\right]$	$p_2 = \left(p_2/p_1\right)p_1$

$$p_{t_2} = \left(p_{t_2}/p_{t_1}\right)p_{t_1}$$

Results

$V_{1n} = 987.27$ ft/s
$M_{1n} = 1.816$
$V_t = 1,937.62$ ft/s

Normal Shock Tables Results

$M_{2n} = 0.613$
$p_2/p_1 = 3.68086$
$T_2/T_1 = 1.543582$
$p_{t2}/p_{t1} = 0.801066$

Calculated Conditions After Oblique Shock

$T_2 = 190.015°$ R $p_2 = 662.555$ psf
$a_2 = 675.44$ ft/s $p_{t2} = 21,893.4$ psf
$V_{2n} = 414.05$ ft/s
$V_2 = 1,981.36$ ft/s $M_2 = 2.933$

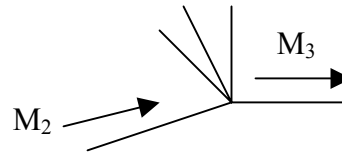**Isentropic Relations-Prandtl-Meyer Expansion**

$M_2 = 2.933$
$\nu_2 = 48.448°$
$\Delta\nu = 15°$

$p_{t2} = p_{t3}$; $T_{t2} = T_{t3}$
$\nu_3 = \nu_2 + \Delta\nu$

$\nu_3 = 63.448$
$M_3 = 3.83$
$P_3 = 181.33$ psf $= 1.259$ psi

INITIAL DISTRIBUTION LIST

1.   Defense Technical Information Center
        8725 John J. Kingman Road, Suite 0944

2.   Dudley Knox Library
        Naval Postgraduate School
        Monterey, CA 93943-5101

3.   Prof. Conrad F. Newberry, AA/Ne
        Department of Aeronautics and Astronautics
        Naval Postgraduate School

        _____

4.   Prof. Garth V. Hobson, AA/Hg
        Department of Aeronautics and Astronautics
        Naval Postgraduate School

        _____

5.   Prof. Max F. Platzer, AA/Pl
        Chairman, Department of Aeronautics and Astronautics
        Naval Postgraduate School

        _____

6.   Prof. Raymond P. Shreeve, AA/Sf
        Department of Aeronautics and Astronautics
        Naval Postgraduate School

        _____